Combined Measurements of Meteorological Variables, Atmospheric Electricity and Aerosol Particle Concentration using a Small Uncrewed Aircraft System

Dissertation
der Mathematisch-Naturwissenschaftlichen Fakultät
der Eberhard Karls Universität Tübingen
zur Erlangung des Grades eines
Doktors der Naturwissenschaften
(Dr. rer. nat.)

vorgelegt von
Martin Schön
aus München

Tübingen
2024

Gedruckt mit Genehmigung der Mathematisch-Naturwissenschaftlichen Fakultät der Eberhard Karls Universität Tübingen.

Tag der mündlichen Qualifikation: 14.10.2024
Dekan: Prof. Dr. Thilo Stehle
1. Berichterstatter/-in: Prof. Dr. Jens Bange
2. Berichterstatter/-in: Prof. Dr.-Ing. Hermann Knaus
3. Berichterstatter/-in: Prof. Dr. Burkhard Wrenger

ABSTRACT

The Uncrewed Aircraft System (UAS) Multipurpose Airborne Sensor Carrier, version 3 (MASC-3), which is capable of measuring the three-dimensional wind vector, air temperature, and humidity at high resolution, was used in this thesis as a starting point in the development of a system that can simultaneously measure meteorological variables, atmospheric electricity, and aerosol particle concentration and size distribution. The aim of this development was to be able to accurately record Saharan dust events and, in contrast to existing measurements, to make in-situ measurements of all of the above variables simultaneously. This is important because no such combined measurements exist to date, and in particular, the influence of atmospheric electricity on aerosol particle transport is still largely unexplored. This thesis consists of three publications, each dealing with one aspect of this combined measurement system. First, MASC-3 was used to measure the local wind field in an Arctic fjord at high resolution. It was shown that the wind field in Kongsfjorden, in the immediate vicinity of the Ny-Ålesund research station on Svalbard, is complex and strongly influenced by the local terrain. MASC-3 captured small-scale katabatic flows that affect aerosol particle transport in the immediate vicinity of the research station, which are not resolved in large-scale numerical models. Second, a sensor payload was developed for MASC-3 to measure the space charge in the atmospheric electric field. Validation measurements of this sensor system were performed by flying MASC-3 past a 100 m high metallic measurement mast. A simulation of the electric field around the mast was compared with the measurement data, and it was shown that MASC-3 was able to measure the changes in the electric field around the mast with low noise after the signal from the charge sensors was corrected to remove the influence of the aircraft motion. Finally, a low-cost Optical Particle Counter (OPC) was integrated into MASC-3 to measure aerosol particle concentration and size distribution. For this purpose, the OPC was equipped with a passive aspiration system and a diffusion dryer and integrated into an airfoil-shaped pod. The measurement system was validated both in ambient conditions against a reference instrument and in a wind tunnel. The three measurement methods were combined in the measurement of a Saharan dust event over Cyprus, where aerosol particle concentration, wind, temperature, humidity, and space charge were measured simultaneously. The resulting measurements can be used in the future to investigate fundamental relationships in aerosol particle transport.

ZUSAMMENFASSUNG

Das Uncrewed Aircraft System (UAS) Multiple-Purpose Airborne Sensor Carrier, Version 3 (MASC-3), das in der Lage ist, den dreidimensionalen Windvektor, die Lufttemperatur und die Luftfeuchtigkeit mit hoher Auflösung zu messen, wurde in dieser Arbeit als Ausgangspunkt für ein System verwendet, das gleichzeitig meteorologische Variablen, atmosphärische Elektrizität sowie die Konzentration und Größenverteilung von Aerosolpartikeln messen kann. Ziel dieser Entwicklung war es, Saharastaub-Ereignisse genau zu erfassen und im Gegensatz zu bestehenden Messungen alle oben genannten Variablen gleichzeitig in-situ zu messen. Dies ist wichtig, weil es bisher keine derartigen kombinierten Messungen gibt und insbesondere der Einfluss der atmosphärischen Elektrizität auf den Transport von Aerosolpartikeln noch weitgehend ungeklärt ist. Die Arbeit besteht aus drei Publikationen, die sich jeweils mit einem Aspekt dieses kombinierten Messsystems befassen. Zunächst wurde MASC-3 eingesetzt, um das lokale Windfeld in einem arktischen Fjord mit hoher Auflösung zu messen. Es zeigte sich, dass das Windfeld im Kongsfjorden, in unmittelbarer Nähe der Forschungsstation Ny-Ålesund auf Svalbard, sehr komplex ist und stark durch das lokale Gelände beeinflusst wird. MASC-3 wurde eingesetzt, um kleinräumige katabatische Strömungen zu messen, die den Aerosolpartikeltransport in der unmittelbaren Umgebung der Forschungsstation beeinflussen und die in großräumigen numerischen Simulationen nicht aufgelöst werden. In der zweiten Publikation wurde für MASC-3 eine Sensornutzlast zur Messung der Raumladung in der Atmosphäre entwickelt. Validierungsmessungen dieses Sensorsystems wurden durchgeführt, indem MASC-3 an einem 100 m hohen metallischen Messmast vorbeiflog. Eine Simulation des elektrischen Feldes um den Mast wurde mit den Messdaten verglichen und es zeigte sich, dass MASC-3 in der Lage war, die Änderungen des elektrischen Feldes um den Mast mit geringen Störungen zu messen, nachdem das Signal der Ladungssensoren korrigiert wurde, um den Einfluss der Flugzeugbewegung zu beseitigen. Im dritten Teil der Arbeit wurde ein preiswerter optischer Partikelzähler Alphasense OPC-3 in MASC-3 integriert, um die Konzentration und Größenverteilung von Aerosolpartikeln zu messen. Zu diesem Zweck wurde der OPC so umgebaut, dass er mit passivem Luftstrom betrieben werden kann, und er wurde mit einem Diffusionstrockner ausgestattet. Das Messsystem wurde gegen ein Referenzsystem als auch in einem Windkanal validiert. Schließlich wurden die drei Messmethoden bei der Messung eines Saharastaub-Ereignisses über Zypern kombiniert, bei dem Aerosolpartikelkonzentration, Wind, Temperatur, Feuchtigkeit und Raumladung gleichzeitig gemessen wurden. Solche Messungen können in Zukunft zur Untersuchung grundlegender Zusammenhänge im Aerosolpartikeltransport genutzt werden.

CONTENTS

A Peer-reviewed first-author publications

ACRONYMS

ABL Atmospheric Boundary Layer

ASL Above Sea Level

AOD Aerosol Optical Depth

APS Aerodynamic Particle Sizer

CALIPSO Cloud-Aerosol Light Detection and Ranging (LIDAR) and Infrared Pathfinder Satellite Observations

CAMS Copernicus Atmosphere Monitoring Service

CCN Cloud Condensation Nuclei

CPC Condensation Particle Counter

DWD German Meteorological Service

E-field Electric Field

ECMWF European Centre for Medium-Range Weather Forecasts

FHP Five-Hole Probe

GFS Global Forecast System

GPS Global Positioning System

HYSPLIT Hybrid Single-Particle Lagrangian Integrated Trajectory

IFS Integrated Forecast System

IMU Inertial Measurement Unit

INS Inertial Navigation System

LIDAR Light Detection and Ranging

MACC Monitoring Atmospheric Composition and Climate

MASC-3 Multipurpose Airborne Sensor Carrier, version 3

MDAP Multicopter Data Analysis Python Package

NOAA National Oceanic and Atmospheric Administration

NWP Numerical Weather Prediction

OPC Optical Particle Counter

PM Particulate Matter

PNC Particle Number Concentration

PG Potential Gradient

PSD Particle Size Distribution

TAS true airspeed

UAS Uncrewed Aircraft System

UCASS Universal Cloud and Aerosol Sounding System

WHO World Health Organisation

1 LIST OF PUBLICATIONS

This work is a cumulative dissertation consisting of three peer-reviewed publications. All publications listed here have already been published or have been accepted as manuscripts.

1.1 Peer-Reviewed Publications, First Author

- Schön, M., V. Savvakis, M. Ketsoudi, A. Platis, and J. Bange, 2024: OPC-Pod: A New Sensor Payload to Measure Aerosol Particles for Small Uncrewed Aircraft Systems. *J. Atmos. Oceanic Technol.*, **early online release**, doi: 10.1175/JTECH-D-23-0078.1

- Schön, M., K. A. Nicoll, Y. G. Büchau, S. Chindea, A. Platis, and J. Bange, 2022a: Fair Weather Atmospheric Charge Measurements with a Small UAS. *J. Atmos. Oceanic Technol.*, **39 (11)**, 1799–1813, doi: 10.1175/JTECH-D-22-0025.1

- Schön, M., I. Suomi, B. Altstädter, B. van Kesteren, K. zum Berge, A. Platis, B. Wehner, A. Lampert, and J. Bange, 2022c: Case studies of the wind field around Ny-Ålesund, Svalbard, using unmanned aircraft. *Polar Research*, **41**, doi: 10.33265/polar.v41.7884

- Related published dataset: Schön, M., K. zum Berge, A. Platis, and J. Bange, 2022b: UAS-based measurement of wind vector, temperature and humidity in Ny-Ålesund, Svalbard, during April and May 2018. PANGAEA, doi: 10.1594/PANGAEA.946961

1.2 Peer-Reviewed Publications, Co-Author

- Savvakis, V., M. Schön, K. A. Nicoll, C. L. Ryder, A. Papetta, M. Kezoudi, F. Marenco, J. Bange, and A. Platis, 2024c: In-situ observations of charged Saharan dust from an uncrewed aircraft system. *Aerosol Sci. Technol.*, **in review**

- Bramati, M., M. Schön, D. Schulz, V. Savvakis, Y. Wang, J. Bange, and A. Platis, 2024: A Versatile Calibration Method for Rotary-Wing UAS as Wind Measurement Systems. *J. Atmos. Oceanic Technol.*, **41 (1)**, 25–43, doi: 10.1175/JTECH-D-23-0010.1

- Savvakis, V., M. Schön, M. Bramati, J. Bange, and A. Platis, 2024a: Calculation of aerosol particle hygroscopic properties from OPC derived PM2.5 data. *Meteorol. Z.*, doi: 10.1127/metz/2024/1198

- Savvakis, V., M. Schön, M. Bramati, J. Bange, and A. Platis, 2024b: Small-Scale Diffusion Dryer on an Optical Particle Counter for High-Humidity Aerosol Measurements with an Uncrewed Aircraft System. *J. Atmos. Oceanic Technol.*, **41 (3)**, 205–219, doi: 10.1175/JTECH-D-23-0093.1

- Harm-Altstädter, B., K. Bärfuss, L. Bretschneider, M. Schön, J. Bange, R. Käthner, R. Krejci, M. Mazzola, K. Park, F. Pätzold, A. Peuker, R. Traversi, B. Wehner, and A. Lampert, 2023: Spatial distribution and variability of boundary layer aerosol particles observed in Ny-Ålesund during late spring in 2018. *Aerosol Research*, **1 (1)**, 39–64, doi: 10.5194/ar-1-39-2023

- zum Berge, K., M. Schön, M. Mauz, A. Platis, B. van Kesteren, D. Leukauf, A. E. Bahlouli, P. Letzgus, H. Knaus, and J. Bange, 2021: A Two-Day Case Study: Comparison of Turbulence Data from an Unmanned Aircraft System with a Model Chain for Complex Terrain. *Boundary-Layer Meteorology*, **180**, 53–78, doi: 10.1007/s10546-021-00608-2

- Mauz, M., B. van Kesteren, W. Junkermann, K. zum Berge, M. Schön, A. Platis, and J. Bange, 2020: Miniature high-frequency chilled-mirror hygrometer for atmospheric measurements aboard fixed wing UAS. *Meteor. Z.*, **29 (6)**, 439–449, doi: 10.1127/metz/2020/1026

- Petäjä, T., E.-M. Duplissy, K. Tabakova, J. Schmale, B. Altstädter, G. Ancellet, M. Arshinov, Y. Balin, U. Baltensperger, J. Bange, A. Beamish, B. Belan, A. Berchet, R. Bossi, W. R. L. Cairns, R. Ebinghaus, I. E. Haddad, B. Ferreira-Araujo, A. Franck, L. Huang, A. Hyvärinen, A. Humbert, A.-C. Kalogridis, P. Konstantinov, A. Lampert, M. MacLeod, O. Magand, A. Mahura, L. Marelle, V. Masloboev, D. Moisseev, V. Moschos, N. Neckel, T. Onishi, S. Osterwalder, A. Ovaska, P. Paasonen, M. Panchenko, F. Pankratov, J. B. Pernov, A. Platis, O. Popovicheva, J.-C. Raut, A. Riandet, T. Sachs, R. Salvatori, R. Salzano, L. Schröder, M. Schön, V. Shevchenko, H. Skov, J. E. Sonke, A. Spolaor, V. K. Stathopoulos, M. Strahlendorff, J. L. Thomas, V. Vitale, S. Vratolis, C. Barbante, S. Chabrillat, A. Dommergue, K. Eleftheriadis, J. Heilimo, K. S. Law, A. Massling, S. M. Noe, J.-D. Paris, A. S. H. Prévôt, I. Riipinen, B. Wehner, Z. Xie, and H. K. Lappalainen, 2020: Overview: Integrative and Comprehensive Understanding on Polar Environments (iCUPE) – concept and initial results. *Atmos. Chem. Phys.*, **20 (14)**, 8551–8592, doi: 10.5194/acp-20-8551-2020

- Leukauf, D., A. El-Bahlouli, K. zum Berge, M. Schön, H. Knaus, and J. Bange, 2019: The impact of a forest parametrization on coupled WRF-CFD simulations during the passage of a cold front over the WINSENT test-site. *Wind Energy Science*, **2019**, 1–24, doi: 10.5194/wes-2019-68

- Bahlouli, A. E., A. Rautenberg, M. Schön, K. zum Berge, J. Bange, and H. Knaus, 2019: Comparison of CFD Simulation to UAS Measurements for Wind Flows in Complex Terrain: Application to the WINSENT Test Site. *Energies*, **12**, 1992, doi: 10.3390/en12101992

- Rautenberg, A., M. Schön, K. zum Berge, M. Mauz, P. Manz, A. Platis, B. van Kesteren, I. Suomi, S. T. Kral, and J. Bange, 2019: The Multi-Purpose Airborne Sensor Carrier MASC-3 for Wind and Turbulence Measurements in the Atmospheric Boundary Layer. *Sensors*, **19 (10)**, 2292, doi: 10.3390/s19102292

1.3 Conference Contributions

- Schön, M., 2023: OPC-Pod: A sensor payload for the UAS MASC-3 to measure Saharan Dust. *8th ISARRA Conference, Bergen, Norway, 01-04 August 2023*, `https://sites.google.com/view/isarra2023/program`

- Schön, M., V. Savvakis, M. Bramati, A. Platis, J. Bange, 2023: Combined measurement of Saharan dust and atmospheric parameters with the uncrewed aircraft system MASC-3 over Cyprus. *EAC Conference 2023, Malaga, Spain, 02-08 September 2023*, `https://www.dfmf.uned.es/EAC2023/index.php?page=program`

- Schoen, M., B. Altstädter, A. Platis, K. zum Berge, P. Manz, A. Rautenberg, H. Mashni, M. Mauz, L. Bretschneider, K. Bärfuss, R. Käthner, A. Peuker, F. Pätzold, A. Lampert, B. Wehner, J. Bange, 2019: Linking boundary layer aerosol particles and dynamics between different measurement sites with unmanned aerial systems in Ny-Ålesund *EMS 2019, Copenhagen, Denmark, 09-13 September 2019*, `https://www.ems2019.eu/ems2019-programme-book.pdf`

- Schön, M., B. Altstädter, L. Bretschneider, K. Bärfuss, R. Käthner, A. Peuker, F. Pätzold, C. Crazzolara, A. Platis, J. Bange, A. Lampert, B. Wehner, 2019: Linking boundary layer aerosol particles and dynamics between different measurement sites with unmanned aerial systems in Ny-Ålesund. *EAC 2019, Gothenburg, Sweden, 25-30 August 2019*, `https://web.archive.org/web/20231107065857/http://media.eac2019.se/2019/08/1-EAC_Overview-1.pdf`

- Schön, M., B. Altstädter, L. Bretschneider, K. Bärfuss, R. Käthner, A. Platis, C. Crazzolara, A. Peuker, F. Pätzold, A. Lampert, B. Wehner, J. Bange, 2019: Analysing the wind field near Ny-Ålesund, Spitsbergen using UAS measurements. *ISARRA 2019, Lugo, 16-19 July 2019*, `https://www.isarra.org/?page_id=625`

- Schön, M., B. Altstädter, L. Bretschneider, K. Bärfuss, R. Käthner, J. Bange, A. Platis, C. Crazzolara, A. Peuker, F. Pätzold, A. Lampert, B. Wehner, 2019: In-situ Aerosol- und Windmessungen in der arktischen atmosphärischen Grenzschicht mit unbemannten Flugzeugen. *DACH 2019, Garmisch-Partenkirchen, Germany, 18-22 March 2019*, `https://www.dach2019.de/DACH2019-abstracts.pdf`

- Schön, M., H. Knaus, K. zum Berge, A. Rautenberg, M. Mauz, J. Bange, 2018: In-situ airborne wind measurements in complex terrain for comparison with wind simulations. *EMS 2018, Budapest, Hungary, 05 September 2018*, `https://meetingorganizer.copernicus.org/EMS2018/EMS2018-588.pdf`

- Schön, M., A. Rautenberg, J. Bange, 2017: In-situ measurement of the airflow over an escarpment with a UAV. *EMS 2017, Dublin, Ireland, 06 September 2017*, `https://meetingorganizer.copernicus.org/EMS2017/EMS2017-603.pdf`
- Schön, M. 2017: Improving the performance of the Multi-Purpose Airborne Sensor Carrier using a Pixhawk flight controller. *ISARRA 2017, Oban, Scotland, 22 May 2017*, `https://www.isarra.org/?page_id=490`

2 INTRODUCTION

Our knowledge of atmospheric processes is steadily growing, but so is the need to understand them: Human activities are increasingly dependent on accurate predictions of atmospheric processes, and the need to understand their interdependencies is becoming more urgent. Among these processes, atmospheric aerosols are of particular relevance, and their study is a rapidly growing field of science.

Aerosol particles, whether from anthropogenic or natural sources, are solid or liquid substances present in the Earth's atmosphere that, together with the air in which they are suspended, form an aerosol.

The effects of atmospheric aerosols on human activities have been recorded throughout history, even when the cause was uncertain. For example, the Roman politician Flavius Cassiodorus described how the sun darkened in 536, unaware that the cause was volcanic ash in the atmosphere, which continued to cause serious climatic changes for decades to come. The scientific exploration of aerosol particles' meteorological implications emerged relatively recently. The first links between aerosol particles and atmospheric processes, such as cloud formation and radiation absorption, were discovered in the late 19th century (Husar et al., 2000).

At the beginning of the twentieth century, aerosol science was primarily concerned with fundamental research, and aerosols played an important role in physics experiments. For example, when developing his cloud chamber, C.T.R Wilson initially wanted to investigate the condensation of water droplets and the behavior of aerosols, and it was only as a result of this that he noticed the relevance of his experimental setup for particle physics (as in: the study of fundamental particles, not aerosol research) (Gupta and Ghosh, 1946). During the 20th century, research focused on the effects of aerosol particles on human health and on the application and generation of aerosols for technical processes (Hinds and Zhu, 2022), and the World Health Organization (WHO) published the first guidelines on harmful exposure to aerosol particles in the 1980s (Pai et al., 2022).

Towards the end of the 20th century, our understanding of the role of aerosol particles evolved significantly, and their influence on various atmospheric processes and climate change was recognized (Preining, 1991).

Aerosol particles affect weather systems and climate by absorbing or reflecting solar radiation and shaping cloud formation when serving as condensation nuclei for moisture (Lohmann and Feichter, 2005; Chung, 2012; Papadimas et al., 2012; Wang, 2013). The net impact of aerosol particles on the Earth's climate is not easy to determine, and secondary effects of aerosol particles may have diverse, sometimes counteracting and non-intuitive consequences (Heintzenberg, 2012). The effect of aerosol particles on climate is also not properly reflected in current numerical models (Li et al., 2022).

Even after leaving the atmosphere, aerosol particles play a role, for example, when reducing the albedo of glaciers, which can lead to increased melting (Gabbi et al., 2015). The effect aerosol particles have on the atmosphere is, among other factors, dependent on particle concentration and size distribution (Leinonen et al., 2022), the vertical distribution of the aerosol in the atmosphere (Watson-Parris et al., 2019; Marinescu et al., 2017), and meteorological conditions such as the structure of the Atmospheric Boundary Layer (ABL) (Miao et al., 2020).

Advances in aerosol research also have an impact on policy and legislation. For example, many European cities have introduced zones that regulate the emission of aerosol particles and other pollutants by restricting vehicle access (Malina and Scheffler, 2015). These regulations, in turn, contribute to the need for better and more reliable measurements of aerosol particles in the atmosphere. Increased awareness of the impact of atmospheric aerosols on human health has also had direct economic consequences, such as strict limits on particulate emissions from vehicles or industrial plants.

Other findings show the influence of aerosol particles on human activities in a more indirect way but are still highly relevant to the Earth's environment. For example, research on the transport of Saharan dust has led to insights into its influence on ecosystems in the Atlantic and Central and South America (Yu et al., 2015), as well as on meteorological processes in Europe (Levin et al., 2005).

This work is part of an area of research that addresses the physical, chemical, and optical properties of aerosol particles and their interaction with meteorological processes. By developing and validating new high-resolution measurement methods on board UAS, the research contributes to answering questions about the transport of aerosol particles and the physical processes governing their interactions with the atmosphere.

Research on aerosol particles in the atmosphere continues to advance. Several research sub-disciplines have emerged, sometimes using fundamentally different methodologies. These different disciplines also often use their own conventions and specific technical terms for displaying data. In order to try to make the work accessible to readers who are not familiar with the peculiarities of aerosol particle research, the following sections briefly summarize the most important concepts regarding measurements with sensors on UAS as far as they are relevant to this work.

3 MEASURING METEOROLOGICAL PARAMETERS, AEROSOLS AND CHARGE WITH UAS

3.1 Using UAS for In-Situ Atmospheric Measurements

For the purpose of combined in-situ measurements of atmospheric parameters, aircraft are a useful platform, as they provide the capability to carry multiple instruments simultaneously while covering a large area, both laterally and vertically. Crewed aircraft are particularly useful for large-scale in-situ measurements, complementing remote sensing approaches such as satellite measurements or LIDAR approaches.

However, small UAS have emerged to fill the niche between in-situ measurements on the ground and remote sensing methods or measurements from crewed aircraft to achieve high-resolution measurements in the troposphere. UAS have been used for meteorological measurements with a wide variety of sensors and, if balloons are included in this category, since the beginnings of modern meteorology. Compared to crewed aircraft, employing UAS results in lower logistical overhead and requires less training for the crew and the pilot. Meanwhile, operating a crewed aircraft is significantly more costly, and attaching meteorological sensors to a certified aircraft also involves a great deal of administrative effort. Compared to a measurement tower, UAS provide coverage over an area and rise above the ABL. Compared to remote sensing applications, an in-situ measurement aboard a UAS can provide higher resolution data (spatially as well as temporally).

In a narrower (and legal) sense, UAS is a term applied to uncrewed rotary or fixed-wing aircraft capable of automatic flight. A UAS is typically controlled by a ground station that issues commands to the UAS. The autopilot on board the UAS then interprets and executes these commands while taking care of the actual flying: It regulates throttle, keeps the aircraft stable, performs maneuvers, and may even launch and land the UAS.

3.2 The UAS MASC-3 for Simultaneous Measurement of Multiple Atmospheric Parameters

UAS have been used extensively for measurements in the atmospheric boundary layer, measuring wind and turbulence (Rautenberg et al., 2019; Reuder et al., 2012), temperature (Wildmann et al., 2013), humidity, aerosol particles (Bates et al., 2013; Altstädter et al., 2015; Renard et al., 2018; Smith et al., 2019) and atmospheric electricity (Harrison et al., 2021). As stated in Sec. 3.6, the aim of this work is to improve the existing methods and to combine several measurements, namely wind, temperature, humidity, aerosol particle concentration, and atmospheric electricity on a UAS platform.

The system serving as the base for the developments in this work is the MASC-3 fixed-wing UAS, operated by the Environmental Physics group of Tübingen University (Fig. 1). However, the resulting sensor package can easily be attached to any fixed-wing UAS, provided it has enough payload capacity (2 kg total) and space.

Based on MASC-3, which already carries a meteorological payload to measure the 3D turbulent wind vector, humidity, and temperature (Rautenberg et al., 2019), we are developing additional sensor systems to extend MASC-3's capability to measure:

- Aerosol particle concentration and size distribution
- Atmospheric electricity

The existing capabilities of MASC-3 to measure meteorological variables are particularly useful when simultaneously measuring aerosol particles.

As previously highlighted, aerosol research is inherently multidisciplinary. However, the complexity of this field extends further with the inclusion of the development, validation, and integration of sensor payloads on UAS.

Without the respective developments and advances in sensor miniaturization and the development of relatively low-cost small UAS, the results presented here would not be possible. Therefore, much of this work is devoted to the methodology itself.

Figure 1. The UAS MASC-3 for atmospheric research operating at a wind energy test site in Baden-Württemberg, Germany, in Spring 2022

3.3 Studying the Local Wind Field in an Arctic Fjord

3.3.1 Limitations of Numerical Models for Investigating Aerosol Transport

Numerical models are often used to study the transport of aerosol particles and to trace the source and composition of aerosols in the atmosphere. At large scales, a common tool for determining the source of aerosol particles are trajectory models such as the Hybrid Single-Particle Lagrangian Integrated Trajectory (HYSPLIT) model provided by the National Oceanic and Atmospheric Administration (NOAA), which calculates the back trajectories of air parcels and is used to trace the origin of aerosol particles in the atmosphere (Stein et al., 2015). HYSPLIT can be run using data from any compatible meteorological model. For applications outside of North America, the NOAA provides the Global Forecast System (GFS). Similar models are the Monitoring Atmospheric Composition and Climate (MACC) model and its successor, the Copernicus Atmosphere Monitoring Service (CAMS) model, both provided by the European Centre for Medium-Range Weather Forecasts (ECMWF), which are based on its Integrated Forecast System (IFS).

The accuracy of the resulting trajectories depends on accurate meteorological parameters and the simulation of particle transport, dispersion, and deposition. The main drivers of particle transport in the atmosphere are advection by wind and turbulence (Lagzi et al., 2013). Particles observed in the atmosphere often do not originate from local sources but are transported by advection, and their distribution depends on the stratification of the atmosphere. For example, Saharan dust can be transported over thousands of kilometers up to the Arctic (Varga et al., 2021). Since the simulation of particle transport is ultimately based on the simulation of advection processes, the model is highly dependent on the underlying simulation of wind and turbulence. This is especially important in complex terrain, where wind conditions are influenced by topography on such a small scale that synoptic weather models can no longer represent the situation, and high-resolution meteorological data is needed for modeling aerosol particle transport (Kurppa et al., 2020), or when considering small-scale elements in the ABL, such as low-level jets (Fiedler et al., 2013).

3.3.2 Wind Measurement Around Ny-Ålesund

In this work, we study the wind field in an Arctic fjord on Svalbard in the immediate vicinity of the internationally relevant research station Ny-Ålesund, where atmospheric gases and aerosols are measured. Aerosol particles are particularly relevant in the Arctic because they remain in the atmosphere for a very long time during the spring and summer months and create the so-called Arctic Haze, which mostly consists of anthropogenic particles transported to the Arctic from lower latitudes. Sources of this aerosol include forest fires in Siberia, industrial emissions in Asia, and shipping (Quinn et al., 2007; Law and Stohl, 2007). Aerosol particles in the Arctic atmosphere affect the radiation budget of the Arctic, cloud formation, and surface albedo (Quinn et al., 2007).

Ny-Ålesund, situated in the Kongsfjorden (King's fjord) on the west coast of Svalbard, is the northernmost continuously inhabited settlement and one of the few research stations in the Arctic that continuously collects data on aerosol particles and atmospheric gases. The wind conditions in the Kongsfjorden differ greatly from synoptic conditions due to the complex terrain (Svendsen et al., 2002). The station is located on the shore of the fjord and is surrounded by several glaciers and high mountains. Numerical Weather Prediction (NWP) models perform poorly in such conditions, especially in the Arctic (Henkies et al., 2023), which in turn makes the tracking of aerosol particles with these models prone to error. Therefore, a good understanding of the local wind conditions and the influence of the complex topography on these wind conditions is very important for the vicinity of Ny-Ålesund.

A two-month measurement campaign was carried out in spring 2018 with the UAS MASC-3 in order to contribute to the research of this wind field and to better understand the wind conditions around Ny-Ålesund (Fig. 6). UAS measurements are particularly well suited for this application. Compared to stationary measurements on the ground, a UAS can cover a large horizontal and vertical area and thus map the wind field in several dimensions. Compared to remote sensing applications such as LIDAR, in-situ measurements with the MASC-3 UAS have the advantage of being able to detect small structures in the wind field with high resolution (Rautenberg et al., 2019) and also work at very low aerosol particle concentrations, which is a difficulty for wind measurements with LIDAR. Compared to crewed flight measurements, a small UAS can also operate close to the ground and in narrow valleys.

3.4 Atmospheric Electricity

3.4.1 The Atmospheric Electric Field

When comparing the transport of Saharan dust in transport models such as the European CAMS with measurements, it is striking that the model underestimates the transport range of larger particles (O'Sullivan et al., 2020; Heintzenberg, 2009). This discrepancy between observations and theory suggests that not all factors influencing particle transport are fully reflected in the models. As our understanding of atmospheric processes grows, and especially as our ability to simulate them improves, more and more factors that influence these transport processes can be included in our models.

One variable that was measured very early on in atmospheric science, but which receives relatively little attention today (outside of thunderstorms), is atmospheric electricity. The influence of atmospheric electricity on atmospheric processes other than thunderstorms and cloud formation was already hypothesized in the early 19th century (Howard, 1865), and various methods for measuring atmospheric electricity were part of many early meteorological measurement campaigns (Harrison and Bennett, 2021). More recent research has highlighted the relationship between the charging of dust particles and the atmospheric electric field (Zheng, 2013; Nicoll et al., 2022; Esposito et al., 2016). There is a strong relationship between the introduction of Saharan dust into the atmosphere and the electric field, as particles are carried by the wind and exchange electric charge (Gringel and Muhleisen, 1978; Esposito et al., 2016), and the charge of desert dust has been measured with ground-based (Silva et al., 2016; Yair et al., 2016) and balloon-borne methods (Nicoll and Harrison, 2009). In addition, Toth et al. (2020) showed the significant influence of electrostatic forces on particle transport, especially on the transport of large particles > 100 µm. It is hypothesized that electrical charge keeping particles aloft contributes to the unexpected long-range transport of large dust particles (van der Does et al., 2018). Another effect influencing aerosol particle dynamics is the "Venetian Blinds" effect, where charged, non-spherical aerosol particles in the atmosphere align themselves along the electric field and thus change the expected absorption or reflection of solar radiation because the effective area of the aerosol particles oriented towards the sun increases or decreases (Ulanowski et al., 2007). The fair weather atmospheric electric field can be simplified as a giant spherical capacitor, with the two conductors being the ionosphere and the solid Earth, and the dielectric being the atmosphere in between (Hill, 1971). The ionosphere has an average potential of around 250 kV relative to the surface. The atmosphere is not a perfect insulator, so a current flows between these two conductors, with a global total of about 1 kA (Rycroft et al., 2008). However, this is a simplification. The ionosphere does not have the same conductivity everywhere, the charge transport influencing the

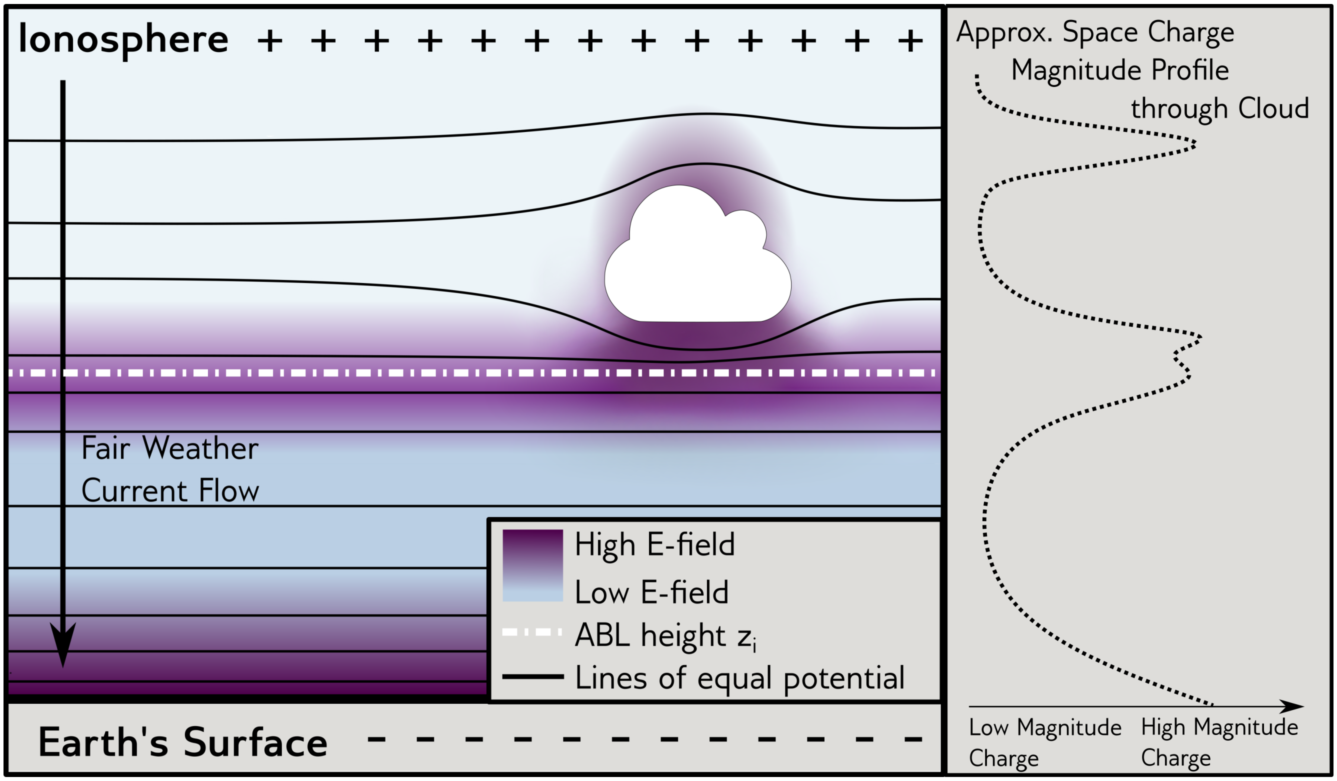

Figure 2. Sketch of the E-field in the earth's atmosphere. The color shading indicates E-field intensity. The Potential Gradient (PG) increases in regions with higher resistance, such as the capping inversion of the ABL or in clouds. On the right side, an approximated profile of the magnitude of space charge ρ is displayed, as it would be captured by the sensors aboard MASC-3. Modified after Schön et al. (2022a)

potential of the ionosphere depends on many factors (galactic cosmic rays, thunderstorms, radioactive decay), which can vary greatly in space and time, and the conductivity of the atmosphere is influenced by stratification, clouds, and aerosol particle concentration (Rycroft et al., 2008). The interplay of these effects creates a complex system.

3.4.2 Measuring the Electric Field

When measuring the fair weather electric field, the vertical component of the Electric Field (E-field), i.e., the Potential Gradient (PG), is the most commonly measured parameter (Harrison and Bennett, 2021). The PG is expressed in voltage per meter height, and typical values are around 100 V/m in the Atmospheric Boundary Layer (ABL) (Harrison and Bennett, 2021). Vertical changes in the conductivity of the atmosphere cause the PG to change locally (see Figure 2). Typically, the PG decreases exponentially with increasing altitude (Gish, 1944).

3.4.3 Compensating for Aircraft Motion

Conductivity is strongly influenced by water droplets and aerosol particles (Rycroft et al., 2008), so changes in PG are common in clouds, dust clouds, and inversions (see Fig. 2). In the UAS measurements presented here, PG is not measured directly, but instead, the space charge ρ is measured using highly sensitive miniaturized space charge sensors, which are well-suited for use on UAS due to their small size and low weight. The space charge is equivalent to the first spatial derivative of the E-field, according to Gauss' law (Eq. 1)

$$\nabla \cdot \mathbf{E} = \frac{\rho}{\varepsilon_0} \quad (1)$$

with ε_0 being the permittivity of free space, and E being the E-field consisting of the three vector components E_x, E_y, and E_z.

For both space charge and PG measurements, the movement of the aircraft through space has a large influence (especially in the vertical plane, as this is by far the largest gradient). This means that movements of the aircraft around its own axes, i.e., roll, pitch, or yaw, also have an influence on the measurements. In addition, the aircraft itself may distort the E-field, which further affects the measurement. There are published methods for correcting the distortion of the ambient E-field by an aircraft and for correcting the motion of the aircraft (Winn, 1993; Koshak et al., 1994; Mach and Koshak, 2007). These methods are applicable when measuring with multiple E-field sensors (i.e., sensors capable of measuring the potential gradient directly) mounted on an aircraft; the most recent approach is described by Mach (2015).

This work describes the implementation and validation of charge sensors on a MASC-3 and an approach to compensate for the influence of aircraft motion on the measurement. Since the E-field itself is not measured as a vector quantity but as ρ, the approach to correct the measurement is also simpler.

The approach presented here first investigated to what extent the movement of the UAS affects the measurement of the charge sensors. Since the meteorological sensor payload installed on MASC-3 also records the position and speed of movement of the aircraft along the roll, pitch, and yaw axis (Fig. 3 b) at a frequency of 100 Hz, it was possible to correlate the signal from the charge sensors with the movement data of the aircraft. The results of this correlation and the correction procedure are described in Section 44.2.

Independent validation with another instrument is difficult for a measurement system that measures the atmospheric charge in-situ on board an aircraft. For example, an instrument that measures the PG on the ground (such as an electric field mill) would not be directly comparable with the MASC-3 measurements, since those show the spatial variations of the E-field (space charge ρ) and not the absolute gradient.

Therefore, in this work, an experimental setup was chosen in which MASC-3 flies through an E-field with a relatively simple geometry, which can then be simulated. This validation experiment was performed at the Falkenberg Meteorological Observatory (operated by the German Weather Service). MASC-3 was flown at different distances and altitudes next to a 100 m high meteorological tower. This setup with a metal, conductive tower in flat terrain is easy to model. A simulation of the tower's E-field was created in the COMSOL physics simulation program.

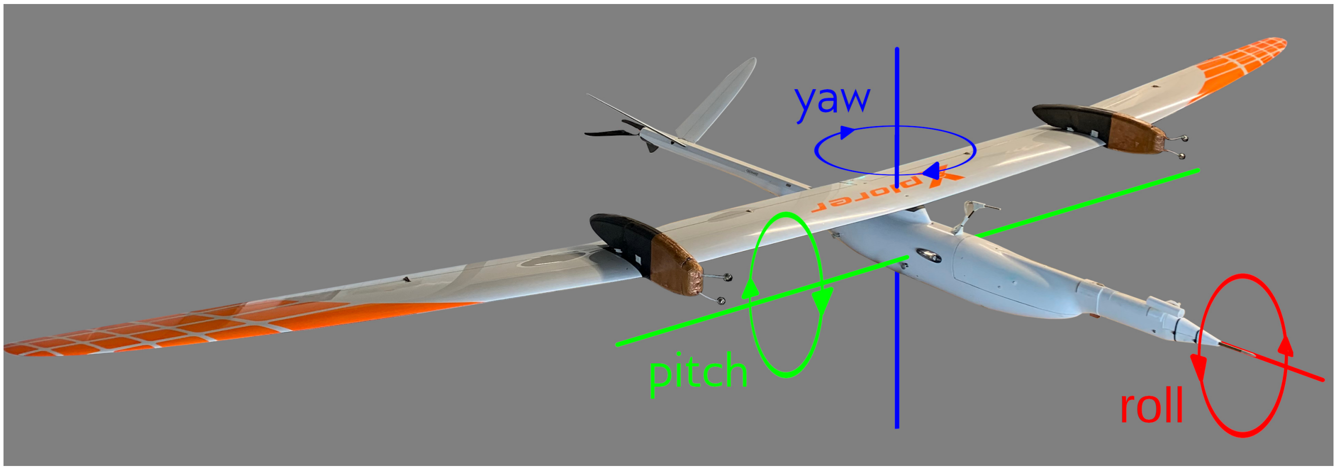

Figure 3. The MASC-3 UAS with charge sensors attached. While motion along every axis theoretically influences the charge measurement, experiments showed that motion along the roll axis (red) is relevant. Modified after (Schön et al., 2022a)

3.5 Aerosol Particle Measurement: Basics and Limitations

3.5.1 Aerosol Particle Size Classification

While there are anthropogenic aerosols that are monodisperse (meaning they consist of only one specific particle size), aerosol particles found in the atmosphere are polydisperse, with a sample of atmospheric air typically containing a range of particle sizes from a few molecules up to particles larger than 100 µm, which are typically found in dust storms (Ryder et al., 2018). The size distribution of aerosol particles is one of the most important factors determining their influence on atmospheric processes (Dusek et al., 2006). Aerosol particles from different sources have typical size distributions, and the size distribution can also provide information about the transport history and age of the observed particles (Jaenicke, 1980). Understanding the impact of physical properties (size distribution, hygroscopicity, light refraction, etc.) on transport processes, weather, and climate is an ongoing area of research (Formenti et al., 2011; Heintzenberg, 2012).

Whitby (1978) described the typical size distribution of urban atmospheric aerosol particles. Looking at the size distribution by particle volume, it typically has three distinct peaks, and Whitby identified these three modes: nucleation (at about 0.01 µm), accumulation (at about 0.1 µm), and coarse (at about 1 µm) (Fig. 4). This evolved into the four modes commonly used today: nucleation, Aitken, accumulation, and coarse (Table 1). The exact boundaries of these modes vary from publication to publication, but the basic division into these size modes is assumed to be general knowledge in this field. This classification is useful due to the fact that different physical and chemical processes are particularly relevant in each of these size modes.

Nucleation and Aitken mode (also classified as ultrafine particles) have a particularly negative impact on human health and are a risk factor for various diseases because their small size gives them a particularly large surface area

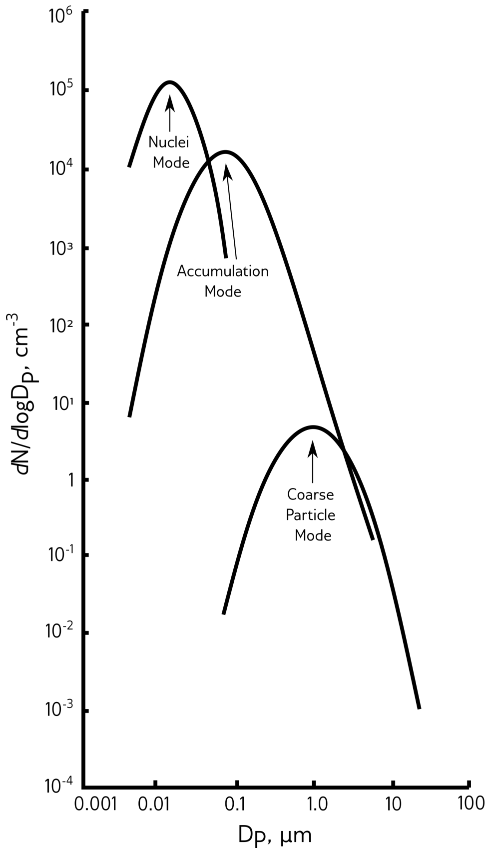

Figure 4. Typical size distribution of ambient aerosol particles in an urban environment, with three size modes: nucleation, accumulation, and coarse. Modified after Whitby (1978)

and they can easily penetrate the organism through the lungs (Kwon et al., 2020; Schraufnagel, 2020), while larger particles are more relevant as Cloud Condensation Nuclei (CCN), indirectly influencing weather and climate (Dusek et al., 2006).

3.5.2 Aerosol Particle Measurement Methods

Methods for measuring aerosol particles can be divided into remote sensing and in situ measurements. Remote sensing methods work at a distance so that aerosol particles can be detected by a station on the ground, remotely by an aircraft, or measured by satellites orbiting the Earth. Since this work focuses on in-situ measurements, only a brief overview of the most common remote sensing methods is given here.

One very common method is LIDAR (Light Detection and Ranging). The basic principle of LIDAR measurements is to direct a laser beam into the aerosol and use the backscatter of the laser beam to obtain information about the concentration of the aerosol particles. Using the depolarization ratio, LIDAR can provide information on particle shape (or the ratio of spherical to irregularly shaped particles). Multi-wavelength LIDAR can provide more information on particle type by analyzing the backscatter at multiple wavelengths. A recent example of an

Size Range	Mode	Size Classification	Instrument
<20 nm	Nucleation	Ultrafine	Electrometer, MPSS, CPC, Cascade Impactor
20 - 100 nm	Aitken		Electrometer, MPSS, CPC, Cascade Impactor
100 - 1000 nm	Accumulation	Fine	Electrometer, MPSS, CPC, OPC, APS, Cascade Impactor
1000 - 2500 nm	Coarse		
>2500 nm		Coarse	Electrometer, OPC, APS, Cascade Impactor

Table 1. Size Modes for Aerosol Particles and typical instruments for in-situ measurement for these size classes, from (Held and Mangold, 2022), based on Whitby (1978). Size Classifications (ultrafine, fine, coarse) based on (Kwon et al., 2020).

instrument that uses the above techniques to measure aerosol vertical distribution and can classify aerosol particles using LIDAR is the Cloud-Aerosol LIDAR and Infrared Pathfinder Satellite Observations (CALIPSO) mounted on the CloudSat satellite (Kim et al., 2018).

Apart from the more advanced instruments such as CALIPSO, remote sensing solutions primarily provide Aerosol Optical Depth (AOD) measurements. In the simplest case, using a passive sun photometer on the ground, AOD is calculated as the ratio of the solar irradiance at a given wavelength reaching the Earth's surface to the irradiance at that wavelength at the top of the atmosphere. In the simplest case of a ground-based radiometer, remote sensing can only provide a single value representing the radiative loss through the entire atmosphere. Although there have been major advances in remote sensing methods in recent years, high-resolution in-situ measurements can still provide more detailed information on aerosol particle concentrations.

When more precise information about local aerosol particle concentrations is needed, or when the exact size distribution and physical properties of aerosol particles are to be studied, in-situ measurements are preferred. For in-situ measurements, there are several approaches for measuring aerosol particles: The oldest is the gravimetric approach, where particles are collected and weighed. Using Cascade impactors or an Aerodynamic Particle Sizer (APS), particles can be sorted by aerodynamic diameter before collection. This approach is typically used as a reference for other types of aerosol particle measurements and is used in legislation (2008/50/EC, Official Journal of the European Union).

Aerosol particles can also be measured by exploiting the electrical capacity of the aerosol particles. Early, simple variants of these instruments had a conductive electrode as an impactor that was struck by aerosol particles. If the aerosol particles were charged, they transferred that charge to the plate, and the current flowing from the electrode was measured with an electrometer (Dhaniyala et al., 2011). Modern instruments do not just rely on the natural charge of particles but actively charge particles to enable measurements. Several types of instruments use electrical charge to measure aerosol particles, providing the ability to capture size distributions for nucleation mode particles up to coarse particles (Table 1).

In this work, we measure with an OPC, which uses the scattering of a laser beam on the aerosol particles.

Because an OPC is based on the scattering of visible light, this method is limited to the detection of particles larger than 100 nm (i.e., the lower limit of Rayleigh scattering) (Held and Mangold, 2022). In practice, most of these instruments are capable of measuring particles from 0.2–0.3 µm in size (Ensor and Dixon, 2011). To measure smaller sizes, the apparent size of the particles can be increased by condensing a liquid on the surface of the particle (thereby increasing its apparent size) before it enters the OPC. An instrument that uses this method is called a Condensation Particle Counter (CPC).

This condensation of liquid on particles, which in turn increases the diameter of the particles, can also occur in nature and is called hygroscopic growth. When measuring with optical methods, it is important to be aware of this hygroscopic growth or to dry the particles before they enter the measurement volume. If this is not done, hygroscopic growth can lead to significant bias in the measurement result (Zhao et al., 2022). It should also be mentioned that the hygroscopic properties of aerosol particles depend on the composition of the particles. By analyzing the hygroscopic behavior of the particles, conclusions can therefore be drawn about the origin of the aerosol particles (Savvakis et al., 2024a).

3.5.3 Estimating Particle Mass from Optical Measurements

As mentioned above, particle mass is the primary parameter used to determine particle load in legislation, but also for research purposes. For aerosol particle concentration, this is the mass of particles per volume of air, called Particulate Matter (PM). It is usually expressed in $\mu g\,m^{-3}$ and is often divided into three categories: PM1, PM2.5, and PM10, sometimes also PM4.

Although most introductory literature defines PM1 as the mass of all particles smaller than 1 µm, PM2.5 as the mass of all particles smaller than 2.5 µm, and so on, which is based on the U.S. Environmental Protection Agency (EPA) National Air Quality Standard for Particulate Matter, the practicalities of particle measurement make this definition more complex.

The original definition of PM and the convention to use particle mass comes from the gravimetric method, in which the particles are separated from the gas, sorted by size, and collected on filters. The filters are then weighed, and the particle mass is determined. This method makes it difficult to accurately measure a specific particle size range because no instruments have an exact cut-off at a specific size limit (Quincey and Butterfield, 2009). In addition, the simple definition of PM only describes the upper, not the lower, size limit for measurement, and this lower limit may vary depending on the measurement method. Another source of uncertainty is volatile components of the aerosol that may evaporate during the filtering process (Quincey and Butterfield, 2009).

To circumvent these problems, the European Union EN12341 definition is therefore based on the description of a standardized gravimetric measurement method.

Clarifying this definition is important because it means that the measurement of PM values with optical methods requires several assumptions to provide a result comparable with PM measurements according to EN 12341.

As used in this work, an optical particle counter (OPC) initially only measures the light scattering of particles in an aerosol that flows through a laser in a measuring chamber. The path from this initial measurement to PM involves several significant uncertainties and assumptions (Held and Mangold, 2022):

- Depending on the device, there is a coincidence probability, i.e., a probability that several particles pass through the laser beam and are evaluated as a single larger particle.
- The particle diameter is calculated by capturing the scattered light hitting the particle using an assumed refractive index and an assumed particle shape (usually spherical). For the refractive properties, polystyrene latex spheres are often used as a reference (Ensor and Dixon, 2011).
- The relationship between light scattering intensity and particle diameter depends on the material of the particle. The relationship is also non-linear and is not necessarily monotonic for the wavelength range where Mie scattering is relevant. This introduces large uncertainties in size classification when the refractive index or particle shape is not known.
- For OPCs, particles are registered in discrete size classes, with high-quality particle counters typically resolving these size classes in fine increments, and low-cost instruments sometimes only measuring a single-digit number of size classes. These size classes are referred to as size bins or bins in the following.
- With the determined particle diameter, the mass of the particle is then calculated using an assumed particle density.

In summary, the output of PM values from OPCs is based on several assumptions, which unfortunately can vary between device manufacturers and are sometimes not disclosed. In order to keep different instruments as comparable as possible, we therefore use the number concentration for displaying aerosol concentration, i.e., the number of particles of a certain size class per volume of sampled aerosol.

The Particle Number Concentration (PNC) is calculated from the number of counts for a given size range divided by the volume of sampled aerosol. The sampled aerosol volume is derived from the sampled air flow (provided the volume flow is measured correctly, taking into account air density). Aerosol particle size distribution often follows a lognormal distribution (i.e., the particle distribution describes a bell curve when the particle concentration is plotted against particle diameter with a logarithmic axis for the diameter). This is an empirical observation, but most size distributions of atmospheric aerosol particles follow this rule (John, 2011).

Following this, size distributions are typically plotted on logarithmic axes, with the particle concentration on the ordinate axis. To compare measurements from different instruments, which may have different numbers of size bins and different ranges of those size bins, the particle concentration is normalized to the size range of the bins.

Dividing by the range of the size bin is done to normalize the PNC and display the size distribution independent of the number and width of the size bins. This allows for size distribution plots to be generated that are comparable, even when made with different instruments measuring over different size ranges (Eq. 2, Held and Mangold, 2022; Seinfeld and Pandis, 2006; TSI Incorporated, 2021).

$$\frac{dN}{d\log(D_p)} = \frac{dN}{\log(D_{p,u}) - \log(D_{p,l})} \tag{2}$$

So for the normalized particle concentration for a given size bin, dN is the particle concentration, in this work specifically the particle number concentration in particles per cm^3. $d\log(D_p) = \log(D_{p,u}) - \log(D_{p,l})$ is the bin width, so the difference between the upper bin boundary and the lower bin boundary.

3.5.4 Sampler Design

Even with a well-functioning OPC and processing that takes into account the OPC's limitations, a meaningful measurement of ambient aerosol particle concentration and size distribution is not guaranteed. An important step in setting up a particle measurement system is the aspiration of the measurement system. Ideally, the OPC would sample an aerosol that is representative of the ambient aerosol. In practice, however, particle loss from the inlet to the sampling volume and sampling bias at the inlet are common, and a representative measurement is difficult to achieve (Brockmann, 2011).

To reduce measurement error, the first step is to provide an adequate flow rate to the sensor, usually through an actively controlled electric pump (or, for smaller instruments, a fan). A high flow rate helps to sample enough particles for meaningful statistics at low particle concentrations. Conversely, a low flow rate ensures that at high particle concentrations, an excessive number of particles do not enter the sample volume and cause measurement errors (Held and Mangold, 2022). Related to this is the flow velocity, which must be low enough to keep the particles in the sample volume long enough to be detected by the OPC. The ratio of particles that have passed through the inlet to those that actually enter the sample volume after being transported through the instrument is called transport efficiency (Brockmann, 2011). To optimize transport efficiency, the flow from the inlet to the sample chamber (the sample line) should be as straight as possible. Bends and constrictions in the line will cause larger, heavier particles with high inertia to bounce into the walls of the pipe and not reach the measurement volume, while smaller particles generally follow the streamlines more easily, resulting in a measurement result biased towards smaller particles (Held and Mangold, 2022).

Accordingly, isoaxial sampling is preferable, i.e., a setup where the ambient airflow has the same direction as the sample airflow. Isoaxial sampling ensures that the aerosol particles do not have to follow a bend in the streamlines when entering the inlet.

Finally, a very significant bias in the measurement can occur at the inlet of the system, depending on the ratio of the ambient air velocity to the inlet velocity. The following applies to thin-walled nozzles, which is the simplest inlet design in terms of aerodynamics. A nozzle with an outer-to-inner diameter ratio of less than 1.1 is defined as thin-walled (Brockmann, 2011; Belyaev and Levin, 1972). In this work, a thin-walled nozzle is used for the measurement system.

The standard convention defines three different regimes for sampling:

- **Super-isokinetic:** Ambient flow is slower than the sample flow.
- **Isokinetic:** Ambient flow speed is equal to sample flow speed.
- **Sub-isokinetic:** Ambient flow is faster than sample airflow.

For minimal particle loss, the system should sample isokinetically (Brockmann, 2011). In the case of the particle measurement system presented here, which is mounted on board an uncrewed fixed-wing aircraft, the sampling is subisokinetic. This means that the flow velocity around the system is faster than the sample airflow. As a result, small particles with low inertia tend to follow the streamlines around the instrument, while heavier particles have enough inertia to maintain their trajectory and are transported into the inlet (Fig. 5) (Brockmann, 2011). As a result, heavier (i.e., typically larger) particles will be overrepresented in the particle size distribution of a subisokinetic sampling instrument.

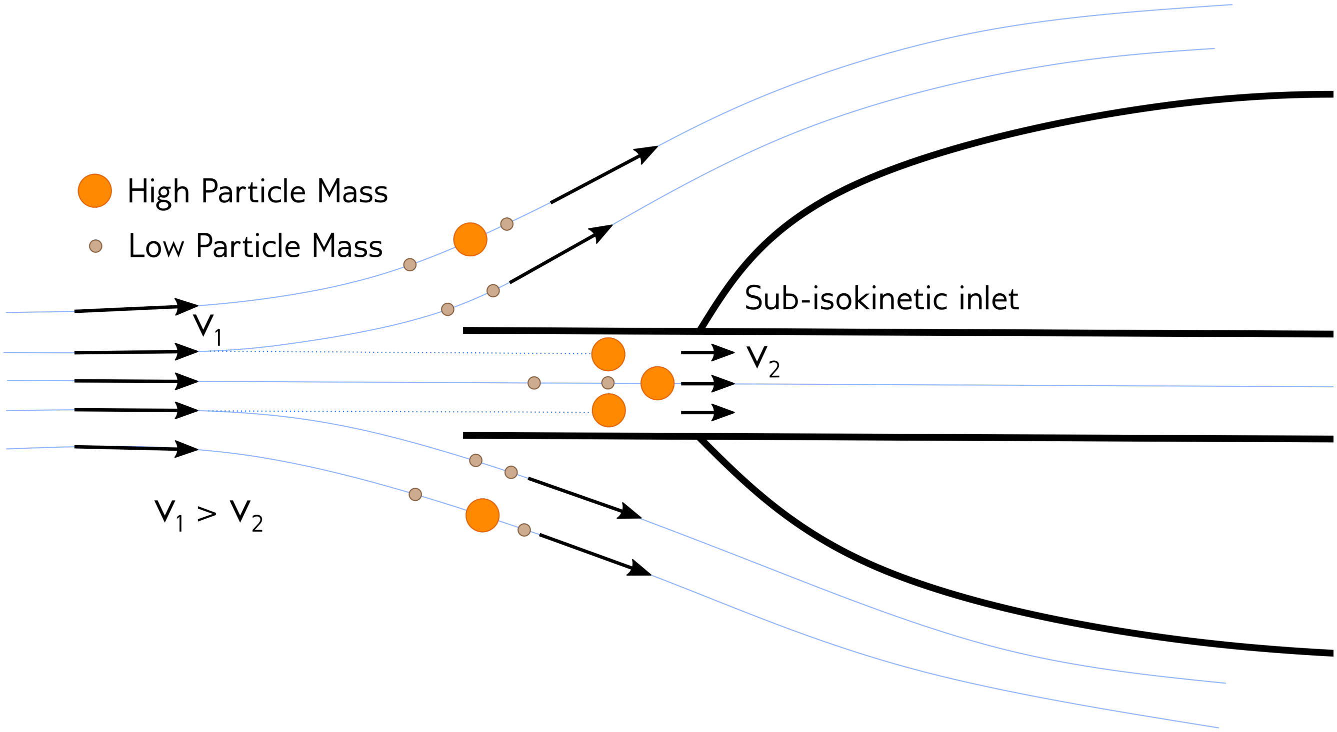

Figure 5. Sketch depicting sub-isokinetic sampling, so the airflow in the inlet (v_2) is slower than the ambient flow (v_1). Small particles (brown) follow the streamlines and avoid the inlet, while larger particles (orange) with sufficient inertia follow a straight line into the inlet and get sampled at a higher rate. Modified after (Wilcox, 1956)

3.6 Main Research Questions

In summary, a sensor package that provides comprehensive information on aerosol particle transport requires measurements of the following variables:

- High-resolution measurements of the meteorological conditions that influence particle transport, i.e., wind, temperature, and humidity. From this, turbulent variables and the structure of the atmosphere can be derived.
- Atmospheric electricity affecting particle deposition and interaction
- Aerosol particle concentration and size distribution. Particle size significantly influences particle transport and is one of the main parameters driving numerical models.

This work aims to develop and validate a measurement platform that can ultimately measure all important parameters simultaneously, in situ, and with high resolution to understand how these factors determine the aerosol particle process. Depending on the measured variable and sensor, case studies of field measurements, laboratory measurements, or a combination of both are used.

This work does not address the chemical composition of aerosol particles or the processes that lead to the formation or modification of aerosol particles in the atmosphere, because the focus is on physical processes influencing transport processes.

4 RESULTS

4.1 Case Studies of the Wind Field around Ny-Ålesund, Using UAS

As described in Section 3.3.2, understanding the local wind field (and thus the movement of air parcels carrying aerosol particles), the structure of the ABL and the troposphere above it (and thus vertical mixing processes affecting particle distribution), and the moisture distribution in the atmosphere is critical to interpreting aerosol particle measurements. In this work, we focused on the case of an Arctic fjord on the island of Svalbard in the Spitsbergen archipelago. Kongsfjorden is located in the northwest of Svalbard (Fig. 6) and is the site of the Ny-Ålesund International Research Station. At this research station and at the nearby Zeppelin Observatory, which is in close proximity to Ny-Ålesund, several facilities measure gases, meteorological parameters, and aerosol particles. It is, therefore, particularly important to understand the microclimate of the fjord and the factors influencing the local wind field, as this directly affects the interpretation of the data from the various measurement stations.

During a measurement campaign between 24 April and 25 May 2018, the UAS MASC-3 performed 18 measurement flights in the immediate vicinity of Ny-Ålesund, covering the Broggerdalen valley and the Ny-Ålesund airfield, 1 km northwest of the town itself. During these flights, MASC-3 collected data on the 3D wind vector, temperature, and humidity between the surface and 500 m above the ground. The results of these flights show a continuous flow from southeast to northwest along Kongsfjorden towards the sea, as already observed in previous surveys. This flow strongly influences the wind conditions in Ny-Ålesund itself and is the dominant wind direction in the village.

In addition to this, in Broggerdalen, MASC-3 recorded a south-south-westerly katabatic flow near the ground, which in some measurements is stronger than the dominant main flow along the fjord (Fig. 7).

This is an important finding for the stations around Ny-Ålesund, as measurements at the Gruvebadet station in Broggerdalen and at the airfield at the mouth of Broggerdalen may be within this katabatic flow, while simultaneously at Ny-Ålesund, the wind comes from a completely different direction. The wind measurement in Ny-Ålesund itself also seems to be influenced by smaller katabatic flows on the slope of Zeppelin Mountain, as there is a secondary south-southwest wind direction in the long-term ground measurements in Ny-Ålesund itself, presumably caused by a similar mechanism as the katabatic wind measured in Broggerdalen.

Using the MASC-3 measurements and the long-term measurements at Ny-Ålesund, we have created a map that shows the structure of the wind field around Ny-Ålesund (Fig. 8) and contains the most important characteristics of the wind field.

a) Overview Map of MASC Measurements

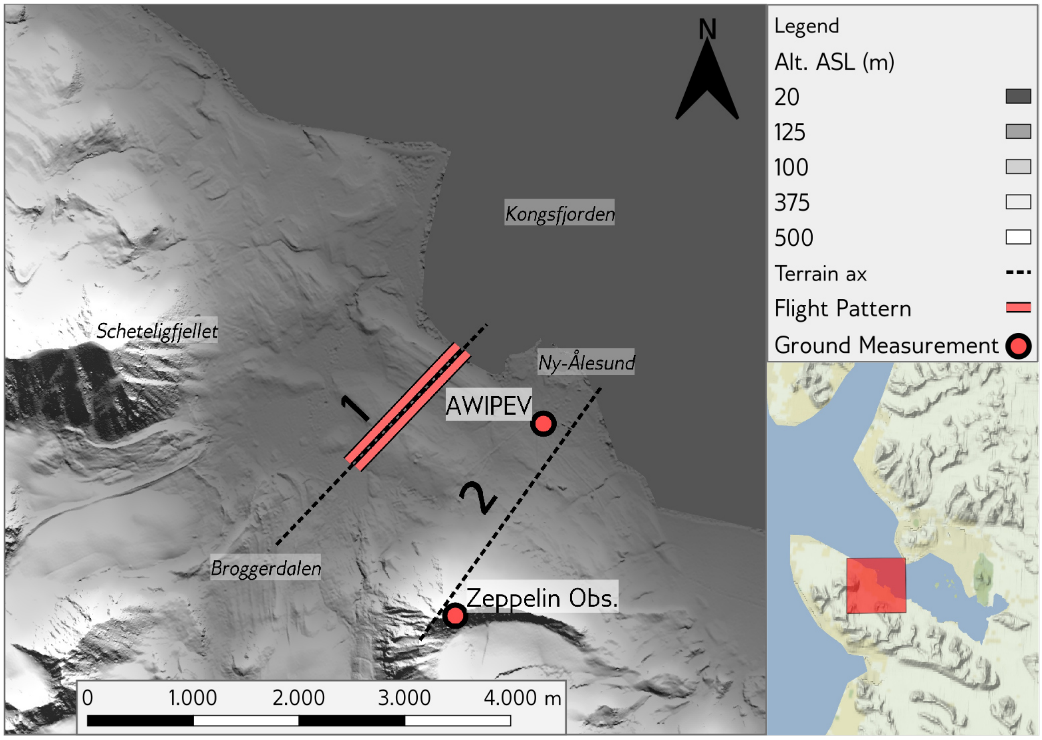

b) Overview Cross-Section of MASC Measurements

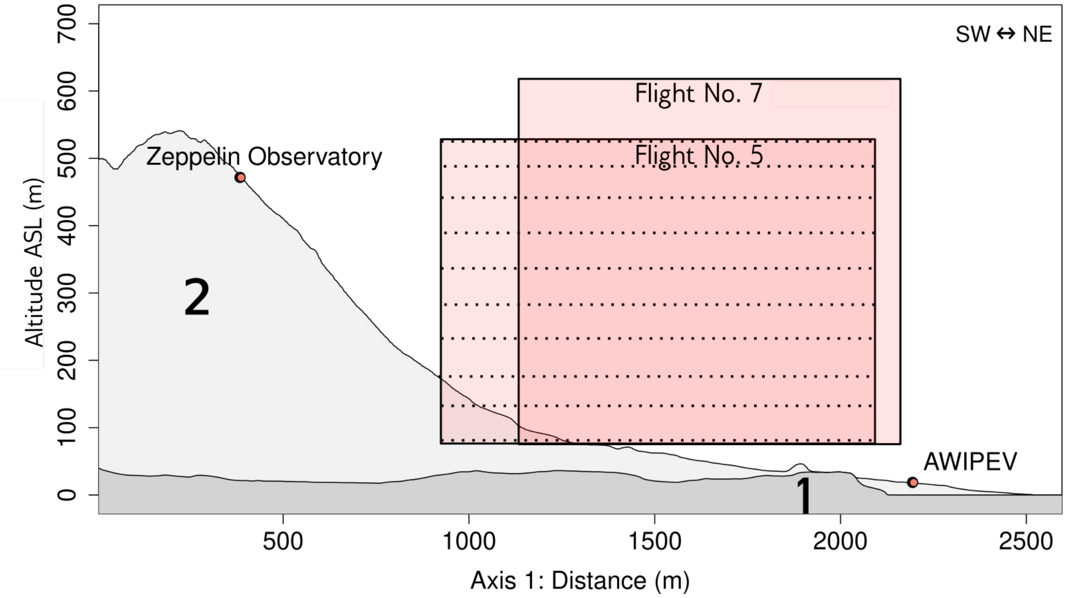

Figure 6. Location of the measurement flights performed near Ny-Ålesund in spring 2018. a) The two case studies presented in this work were flown along axis (1). b) Cross-section of the extent of the measurement flights, with the terrain along axes (1) and (2) displayed in the profile. Modified after Schön et al. (2022c)

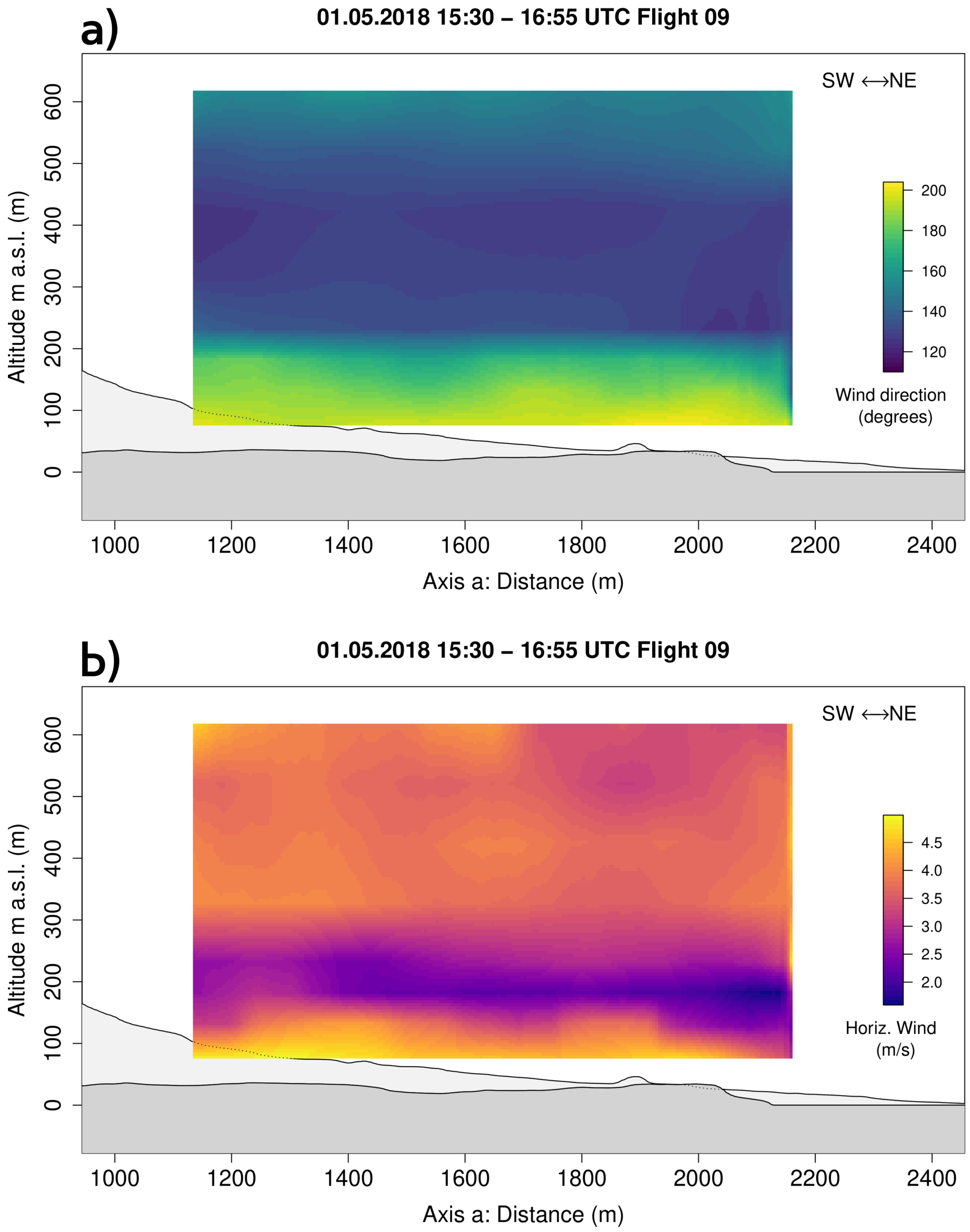

Figure 7. Case study measurement from 01 May 2018, showing wind direction and horizontal wind speed as measured by MASC-3 along Broggerdalen, with the fjord to the NE and the glacier to the SW. The referenced axis a is displayed on the map in Fig. 6. The measurement shows a katabatic flow at the lowest measured heights, with increased wind speed and a rotation of the wind direction. A decrease in wind speed to about 2 $\mathrm{m\,s^{-1}}$ at 110 - 250 m Above Sea Level (ASL) is observed at the interface between the katabatic flow below and the air above. On the vertical axis, data between the horizontal flight legs displayed in Fig. 6 is linearly interpolated.

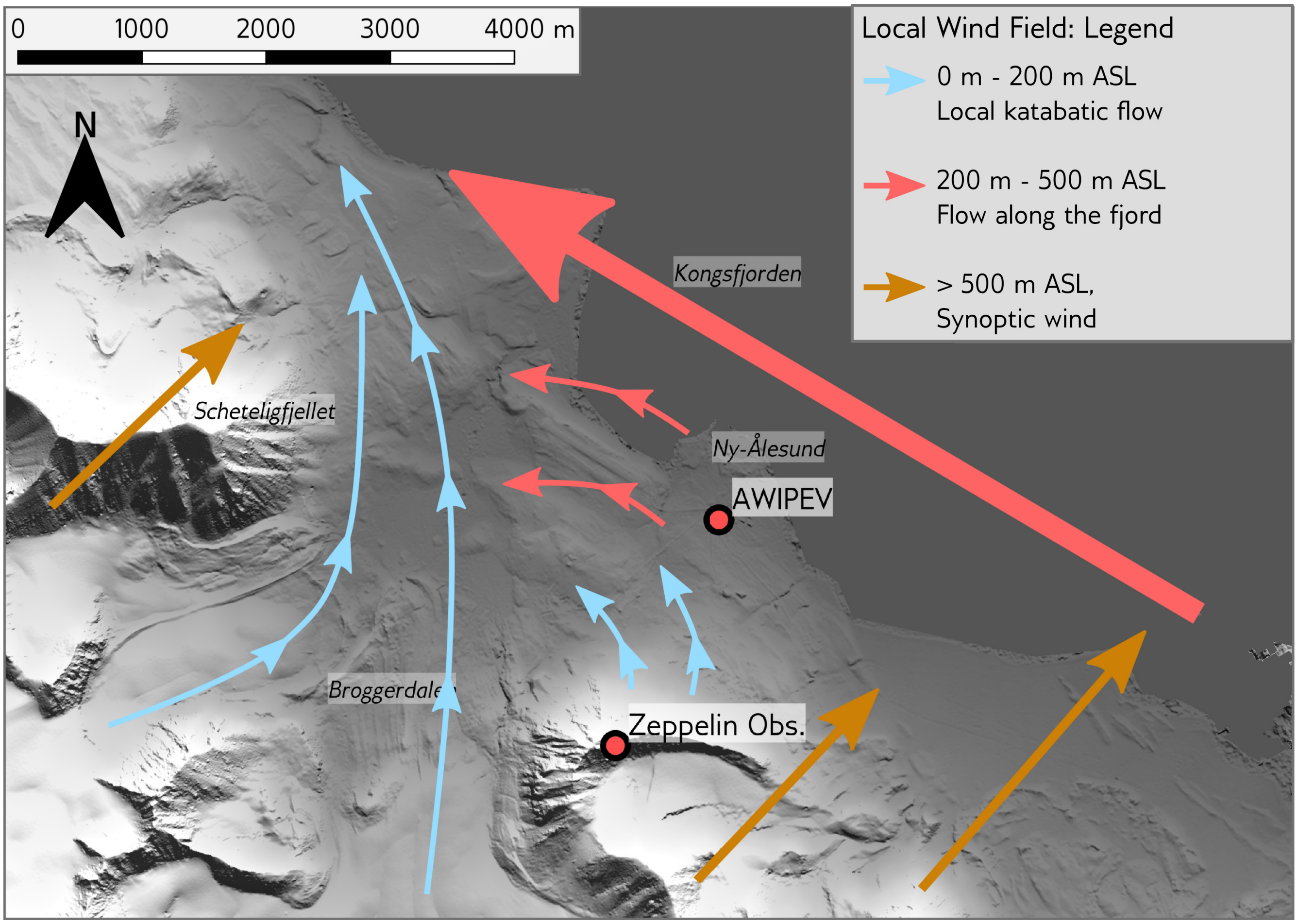

Figure 8. Interpretation of the wind field around Ny-Ålesund for spring and early summer, incorporating MASC-3 measurements and long-term measurements at Ny-Ålesund and Zeppelin observatory. The dominant feature in the wind field is the flow along the fjord (red), with deviations in wind direction caused by katabatic flows (blue) near the surface. Generally, the wind field in the fjord is decoupled from the synoptic wind (brown). Figure from Schön et al. (2022c)

4.2 Fair-Weather Atmospheric Charge Measurements with a Small UAS

As described in Section 3.4, atmospheric electricity is an important quantity that has been neglected in current modeling approaches. Measuring a vertical profile of the E-field or derived quantities requires in-situ measurements on aircraft. In order to combine the measurement of atmospheric charge with the measurement of other meteorological parameters, we developed add-on sensor pods for MASC-3, which contain sensors for atmospheric charge (originally described in Nicoll and Harrison, 2009; Nicoll, 2013) as well as an integrated logging system (Fig. 3). Several test flights were conducted to validate these sensors.

A strong correlation was found between the output of the charge sensors and the aircraft's roll rate (Fig. 9 a). Since the charge sensors are mounted on the wings, 1 m away from the center aircraft, a rolling motion causes a particularly large movement of the charge pods, which amplifies the influence on the charge measurement. To compensate for this influence, we demonstrate a method that generates a correction function from the roll rate recorded by the onboard Inertial Navigation System (INS) using a kernel generated from analyzing the correlation of charge sensor output and roll rate during a calibration flight.

The correction function can then be subtracted from the raw charge sensor data to minimize the influence of aircraft motion (Fig. 9 b). When applied to flight measurement in the ABL, the correlation coefficient between the raw charge sensor data and the roll rate is 0.5 - 0.6. After processing with the correction function, the correlation coefficient drops to 0.4.

To validate the charge sensor measurements, the E-field around a 100 m metal tower in flat terrain was modeled in the COMSOL physics simulation. This model was then compared to the measurement data collected while flying past the tower. The flyby of the tower produces a distinct signal in the charge sensors (Fig. 10), which decreases in amplitude as the distance to the tower increases.

The function of the distance to the tower versus the maximum amplitude in the charge sensor response waveform was then compared to the simulated divergence of the E-field with respect to the distance to the tower. A comparison of the two curves shows good agreement (Fig. 11). This shows that the charge sensors on MASC-3 are detecting the distortion the metal tower is causing in the ambient E-field. It should be noted that this experiment confirms that MASC-3 is able to detect the structure of the E-field around the tower, but not discrete values of the PG, since MASC-3 only measures space charge.

Finally, vertical profiles were flown under good weather conditions to capture the structure of the ABL. The structure of the ABL, especially the inversion at the upper boundary of the ABL, is reflected in the vertical profile of the space charge, as expected. This shows that MASC-3 can measure the ambient space charge with sufficient resolution even at the relatively low charge values in the fair weather atmosphere.

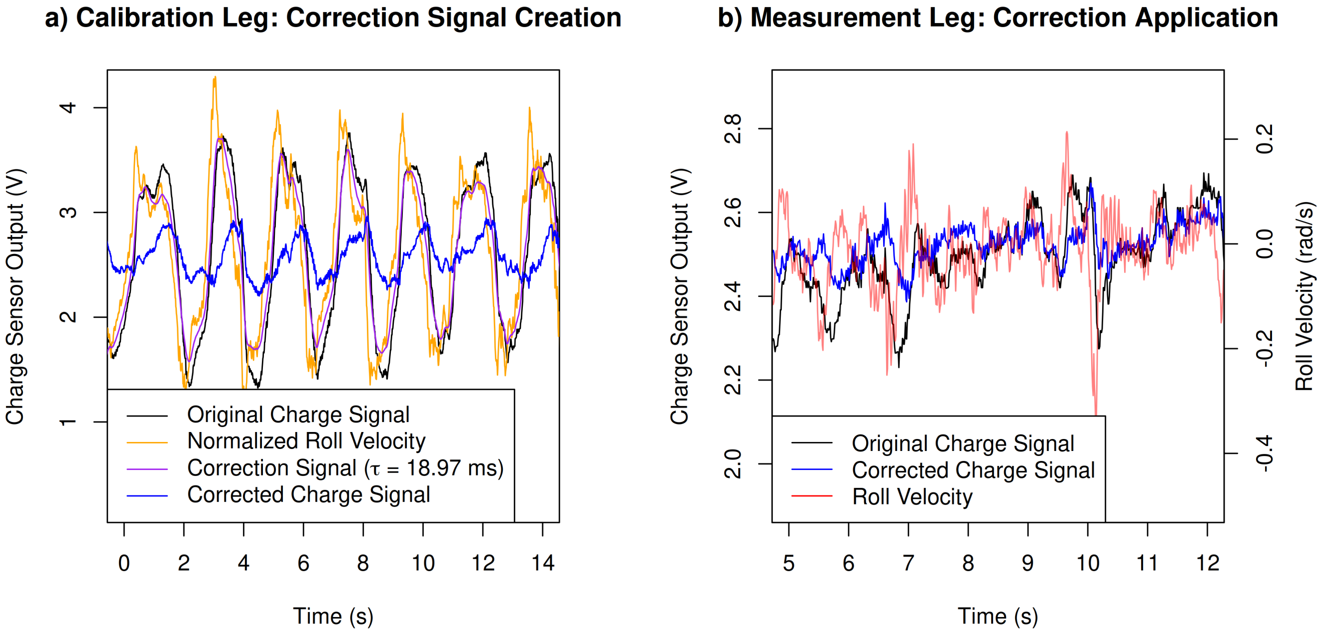

Figure 9. (a) Correlation between the charge sensor signal (black) and the roll rate (yellow) during a calibration flight with a pilot-induced rolling motion. From this correlation, a correction signal is generated (purple) and subtracted from the original charge sensor signal to create a corrected charge sensor signal (blue). (b) Application of the roll rate correction on measurement data captured in the ABL. Figure from Schön et al. (2022a)

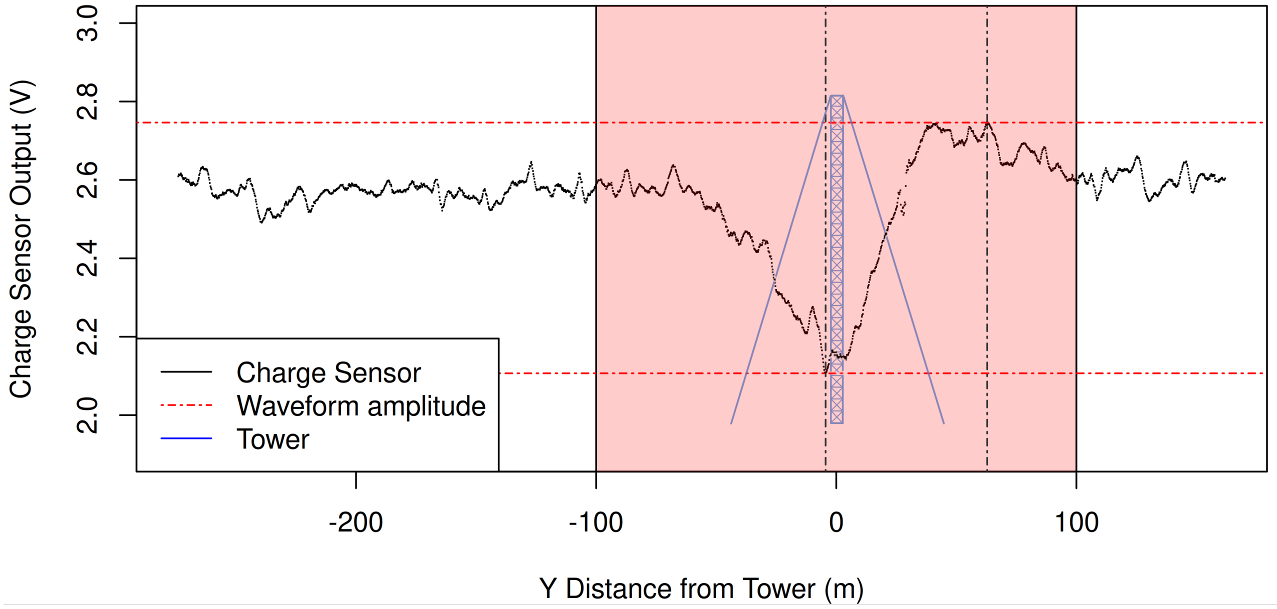

Figure 10. Charge Sensor signal while flying past a 100 m metal tower. The amplitude of the observed waveform (red dashed lines) is dependent on the distance of the aircraft to the tower. Figure from Schön et al. (2022a)

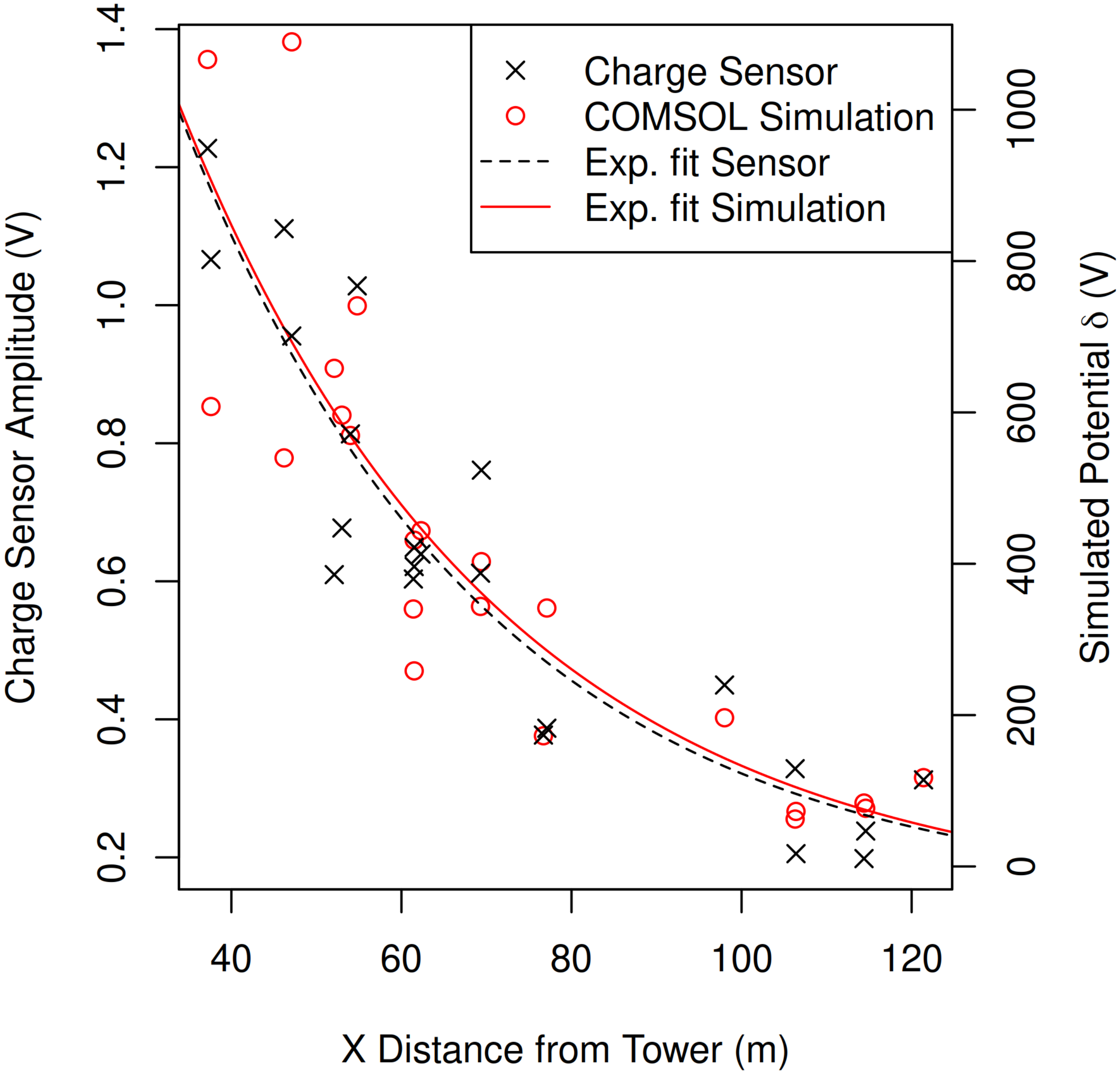

Figure 11. Function of the charge sensor waveform amplitude response to the tower (see. Fig. 10) versus the distance to the tower, compared to the simulated potential gradient from the COMSOL simulation. Figure from Schön et al. (2022a)

4.3 OPC-Pod: A Sensor System for Measuring Saharan Dust Using Small UAS

The OPC-Pod presented here was developed to enable the measurement of aerosol particle concentration on the small fixed-wing UAS MASC-3 in addition to the existing sensor payload measuring wind, temperature, humidity, and atmospheric electricity. It is an airfoil-shaped pod containing an OPC with a dryer, a flow sensor, and a logging system. The system is based on a low-cost, lightweight Alphasense OPC-N3 (Alphasense, 2019) that has been slightly modified by removing the built-in fan and replacing it with a passive aspiration system.

The passive aspiration system, described in detail in Mashni et al. (2023), consists of an air inlet at the front of the pod and an exhaust at the top of the pod. Because the pod is shaped like an airfoil, the pressure gradient between the inlet and the exhaust ensures a steady flow through the system. The airflow is measured with the Sensirion SMF3300 flow sensor mounted downstream of the OPC-N3. Because the MASC-3 autopilot maintains a constant indicated airspeed (and therefore a constant dynamic pressure on the OPC-Pod) during flight, the airflow through the system remains constant even if the air density changes during a measurement flight (Fig. 12).

Between the inlet and the OPC-N3, a self-built diffusion dryer is mounted. This dryer is been described in Savvakis et al. (2024b). The dryer can reduce the effect of hygroscopic growth described in Sec. 3.5. The ability to measure dry particle concentration is a major advantage over remote sensing methods or other small particle measurement devices mounted on UAS or balloons. This work focuses on the development and validation of the OPC-Pod. Three separate validation experiments were performed:

First, the OPC-Pod was tested in ambient conditions on the ground against a reference device and an unmodified OPC-N3. This experiment was designed to ensure that the modifications made to the OPC-N3 do not affect the sensor's functionality. The performance of the OPC-Pod compared to a reference device was determined, as was the performance of the drying channel on the OPC-Pod compared to an unmodified OPC-N3 without a dryer. The experiment occurred at an environmental monitoring station north of Mannheim (Germany). The OPC-Pod (aspirated with a pump) and an unmodified OPC-N3 were placed next to the inlet of the Palas Fidas 200 aerosol particle measurement system of the environmental monitoring station (Fig. 13).

The measurement was done twice, once on 14 February 2023, at low temperatures and very high humidity (up to 98%) and once on 10 October 2023 in clear, sunny weather and lower humidity (50% - 60%). The results of this measurement, presented as a particle size distribution (Fig. 14), show that the performance of the OPC-Pod in both experiments is close to that of the reference instrument. In general, there is a slight underestimation of the particle number of the OPC-Pod compared to the Palas Fidas 200 for particles above 3.0 µm. In contrast to the OPC-Pod, the unmodified OPC-N3 shows a large variation between the two measurements. In dry conditions (Fig. 14 b), the performance of the unmodified OPC-N3 is similar to that of the OPC-Pod. In humid conditions, however, the unmodified OPC-N3 shows an extreme overestimation of the particle concentration, up to 1000% higher particle

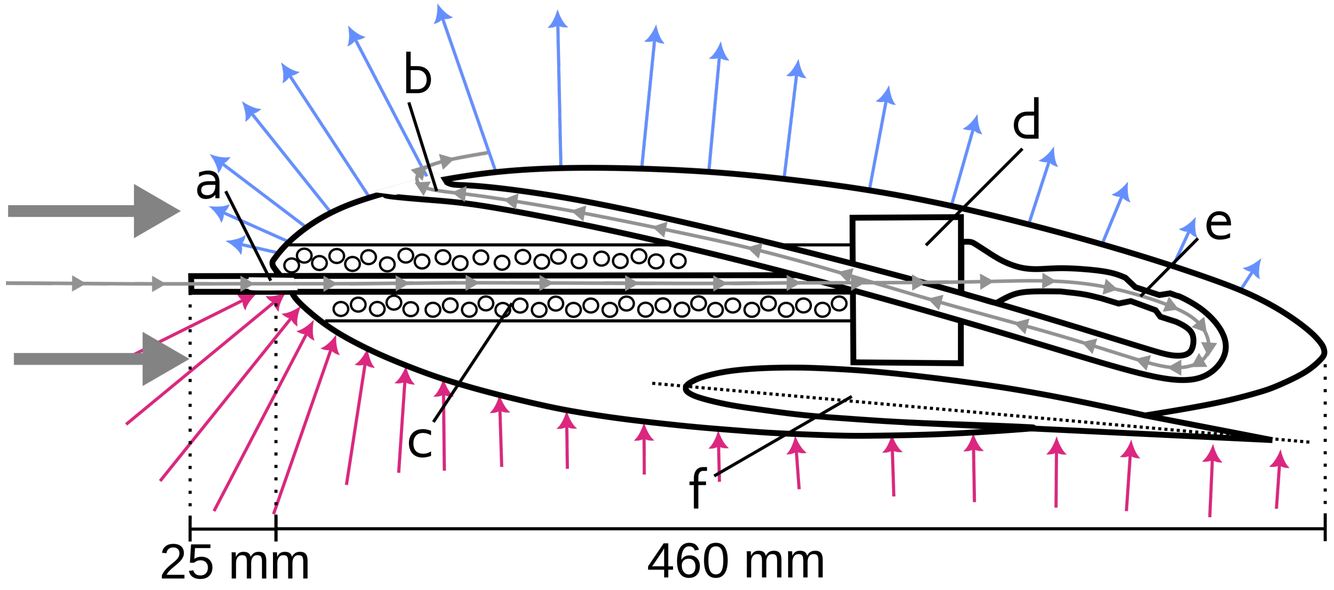

Figure 12. Cross-section of the OPC-Pod. The flow around the airfoil-shaped pod creates a pressure gradient (blue and red arrows), leading to a constrained airflow from the inlet (a), through the diffusion dryer (c), the OPC-N3 (d), the mass flow sensor (e) and finally out of the exhaust (b) (grey arrows). The OPC-Pod is mounted on the wing of MASC-3 (f). Figure from Schön et al. (2024)

concentrations than the OPC-Pod and the Palas Fidas 200 (Fig. 14 a). This overestimation results from hygroscopic growth, as the unmodified OPC-N3 does not have a dryer.

A second validation experiment was conducted in a wind tunnel. The objective of this experiment was to quantify the extent to which subisokinetic sampling (see Sec. 3.5) and other aerodynamic effects affect the particle size distribution recorded with the OPC-Pod compared to an unmodified OPC-N3. For this purpose, the OPC-Pod was mounted in a wind tunnel and an unmodified OPC-N3 was mounted out of the direct airflow at the inlet of the wind tunnel. In addition, a Palas Fidas Frog (Palas GmbH, 2023) was run alongside the unmodified OPC-N3 to provide a total number concentration for comparison with both instruments.

The wind tunnel was then set to a velocity of 18.5 m s^{-1}, which corresponds to the airspeed of the MASC-3. Polydisperse dolomite particles with a size distribution between 0 and 20 µm were then dispersed into the wind tunnel. As the air circulates in the wind tunnel, homogeneous particle distribution is established after a short time. This gradually decreases over the course of approximately 2 hours due to deposition until finally, the ambient particle concentration before the dolomite dust injection is reached again. The polydisperse dolomite particles were chosen because they are a good surrogate for mineral dust and are less harmful than quartz dust.

The experiment was repeated six times, and the recorded number concentration of the OPC-Pod and the unmodified OPC-N3 was compared. The results are consistent with the expectations of sub-isokinetic sampling. Compared to the unmodified OPC-N3, the OPC-Pod shows a higher concentration for the larger particles above

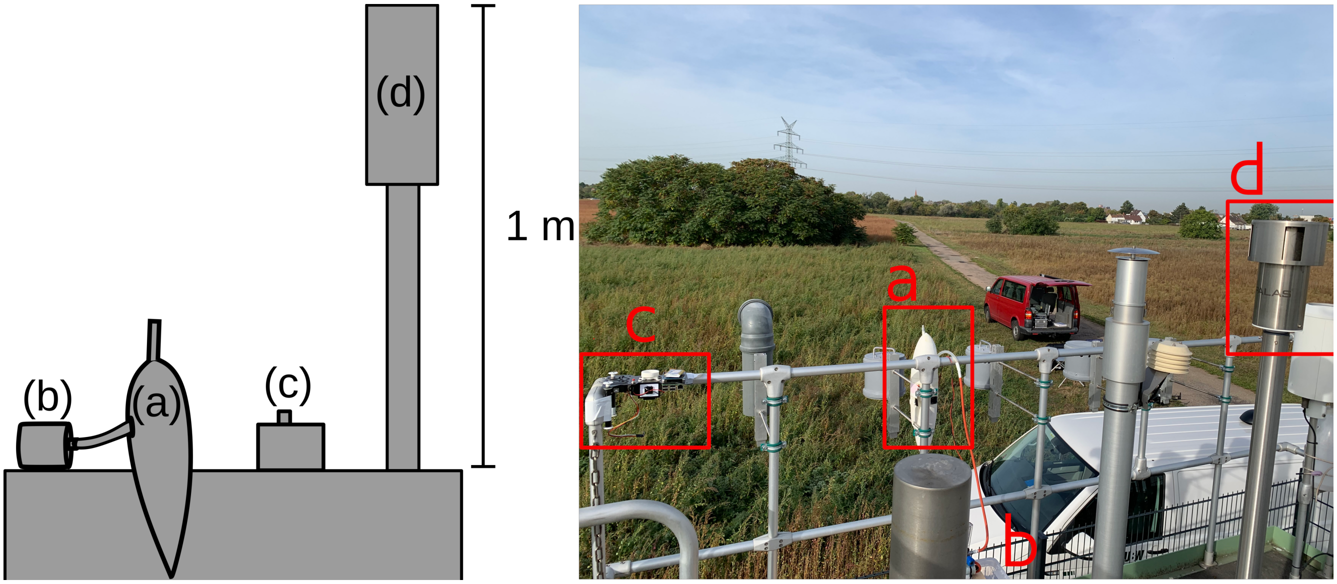

Figure 13. Validation setup at the Environmental Monitoring station in Mannheim, Germany. The OPC-Pod (a) and the unmodified Alphasense OPC-N3 (c) are mounted next to the Palas Fidas 200 inlet (d). The OPC-Pod is aspirated by a pump (b) during the experiment. Figure from Schön et al. (2024)

2.3 µm diameter and a lower concentration for particles below 2.3 µm (Fig. 15).

Finally, a measurement campaign was conducted with the OPC-Pod to evaluate the performance of the system under flight conditions on MASC-3. For this purpose, flights were performed in Cyprus, at the Orounda Airfield of the Cyprus Institute during a Saharan dust event (Fig. 16) in the spring of 2022 during a Saharan dust event. Immediately following the MASC-3 flight presented here, a Cyprus Institute UAS equipped with a Universal Cloud and Aerosol Sounding System (UCASS) OPC ascended (Smith et al., 2019). Both MASC-3 and UCASS produced a vertical profile of the particle concentration of the entire dust layer over Cyprus, rising above 3000 m ASL.

The UCASS and OPC-Pod vertical profiles agree well for the 0.66-37 µm size range and clearly show a dust layer between 1500 and 2800 m ASL. In the dust layer, there are two maxima in particle concentration, the OPC-Pod shows 25 cm^{-3} at 2000 m ASL and 29 cm^{-3} at 2300 m ASL, UCASS measures 22 cm^{-3} at 1740 m and 35 cm^{-3} at 2400 m ASL. Interestingly, most patterns in the vertical profile of UCASS are shifted downward compared to those captured by MASC-3. The dust layer captured during the descent of MASC-3 is also shifted downward compared to the measurement during the ascent. This is likely due to the dust layer changing and moving in its vertical extent during the measurement period.

The MASC-3 and UCASS size distributions are shown for two sections (Fig. 17), one for the measurement in the dust layer and one for the measurement from the ground to below the dust layer. Comparing these two layers, there is an increased concentration of coarse particles larger than 5 µm in the dust layer.

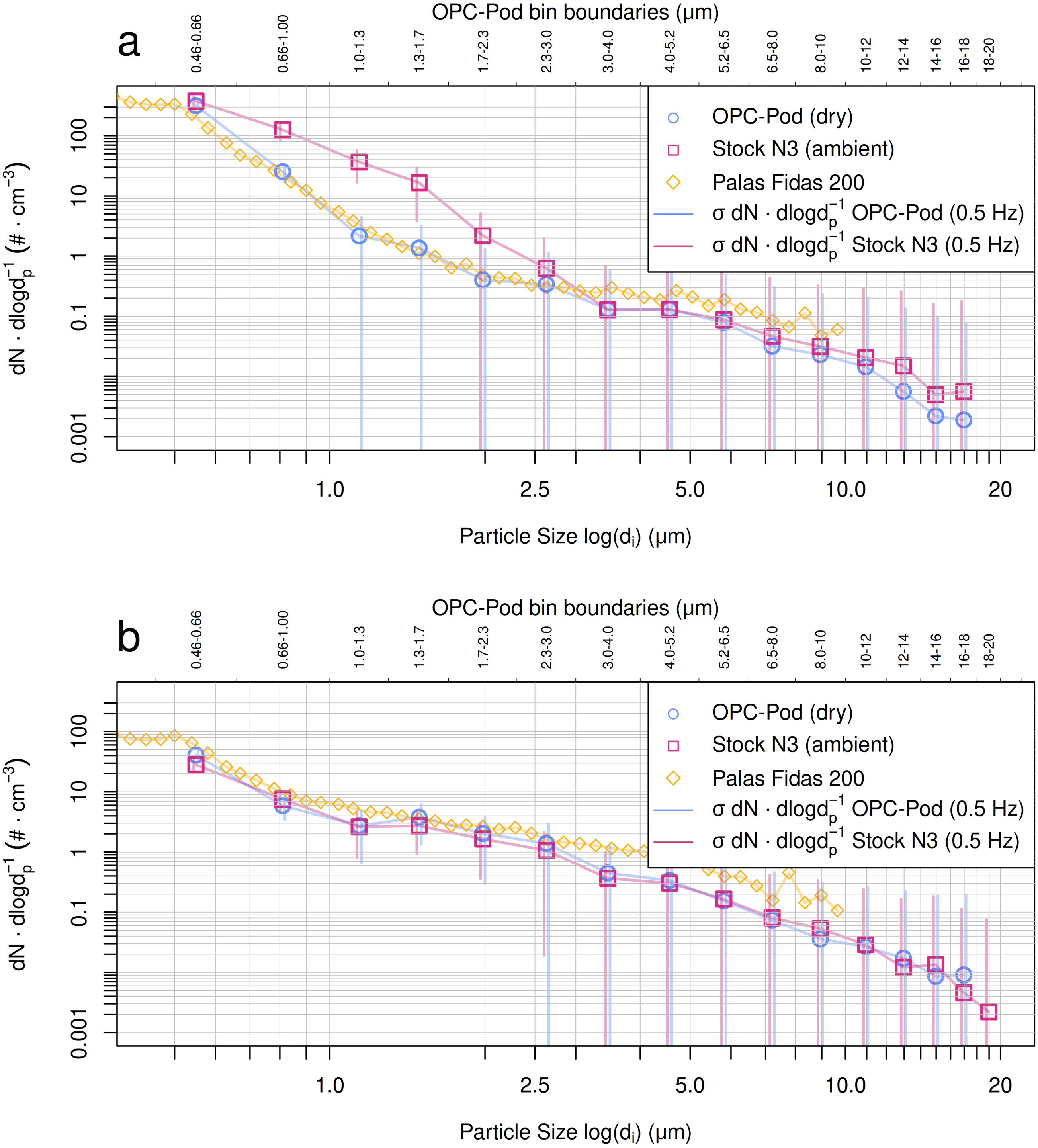

Figure 14. Particle size distribution from the Mannheim validation experiment, for the OPC-Pod with attached dryer (blue), the unmodified Alphasense OPC-N3 (red), and the reference Palas Fidas 200 with drying system (yellow). The first test run (a) took place during humid conditions, and consequently, the system without a dryer shows significant overestimation in the lower size bins; the second test run (b) shows good agreement between the OPC-Pod and the unmodified Alphasense OPC-N3, with both instruments showing a slight underestimation compared to the Palas Fidas 200. Figure from Schön et al. (2024)

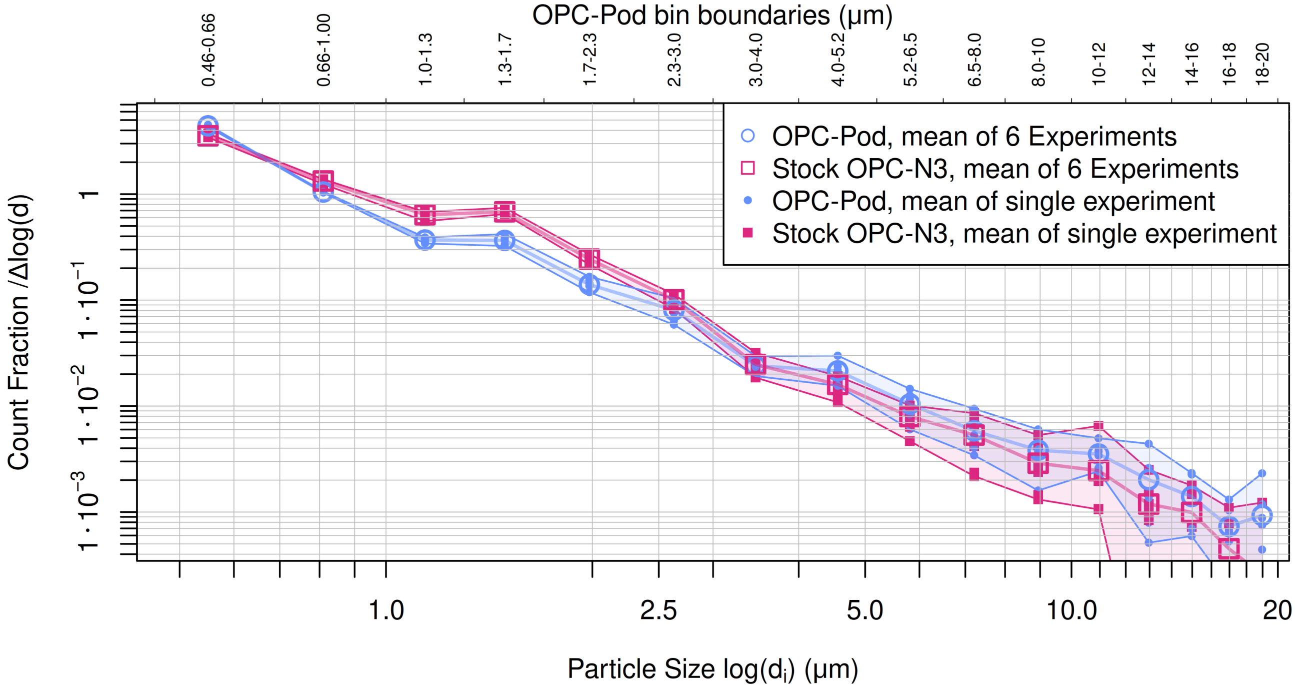

Figure 15. Normalized count fraction for the windtunnel experiment, showing count fraction for the OPC-Pod (blue circles) and the unmodified Alphasense OPC-N3 (red squares). Solid symbols show the mean count fraction for each of the 6 experiments and outlined symbols show the mean of all 6 experiments. Figure from Schön et al. (2024)

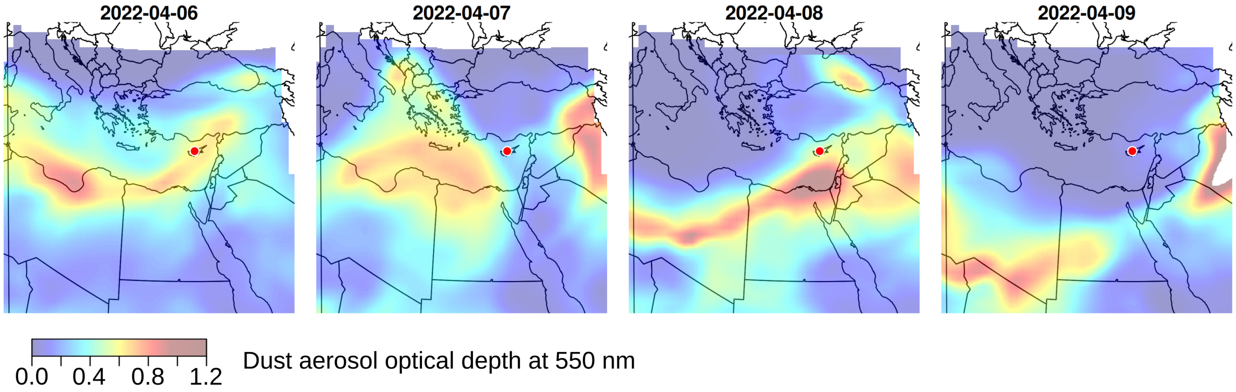

Figure 16. Dust AOD at 550 nm from the CAMS global reanalysis model (Generated using Copernicus Atmosphere Monitoring Service Information 2023), 6 April 2022 - 9 April 2022 (0000 UTC) over the eastern Mediterranean. Cyprus (and the Orounda airfield) are marked with a red dot. The flights presented in this work took place on 6 April 2022. The maximum AOD was reached on 6 April, and during the following week, the dust event subsided.

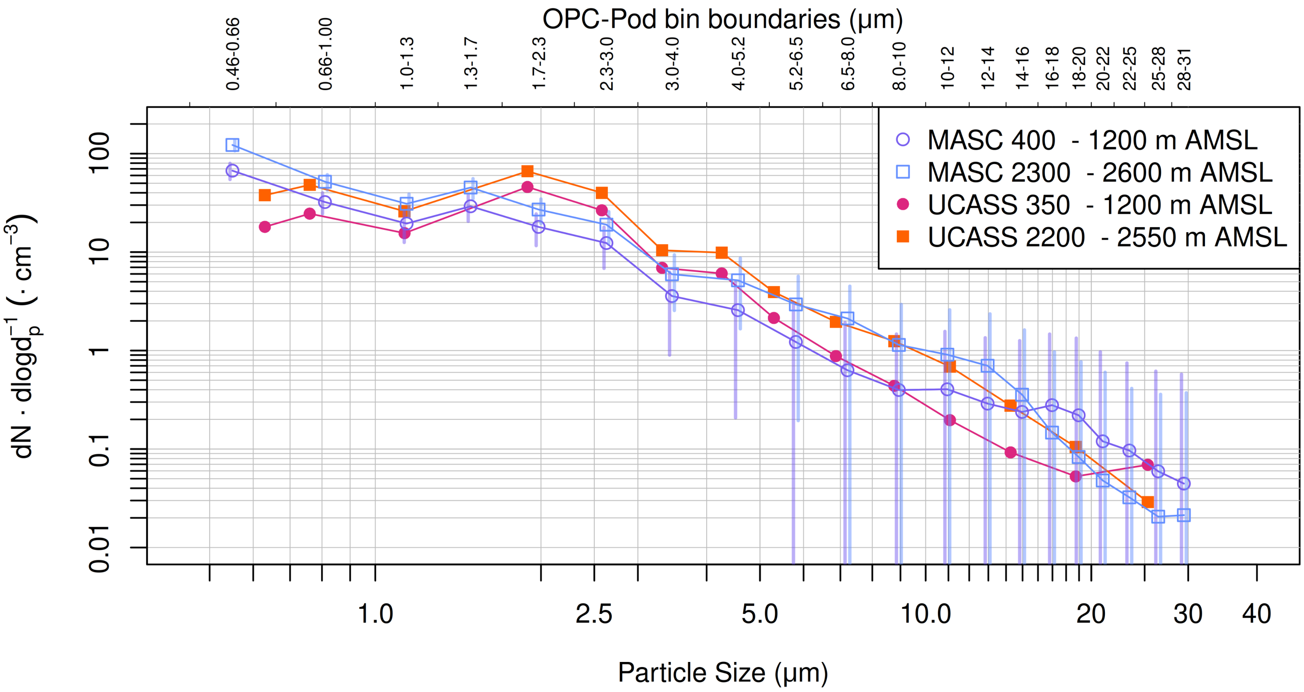

Figure 17. Number concentration size distribution captured by MASC-3 and UCASS over Orounda, Cyprus on 6 April 2022. Size distributions for two altitude ranges are shown, one altitude range covering the area close to the ground (purple for MASC, red for UCASS), and one altitude range covering the dust layer (blue for MASC, orange for UCASS). Error bars show the standard deviation per altitude range and size bin. Figure from Schön et al. (2024)

5 DISCUSSION

The results presented here show how a small, relatively inexpensive UAS and an appropriate sensor package can be used to make high-resolution in-situ measurements of wind, temperature, humidity, aerosol particle concentration, and atmospheric electrical charge. The simultaneous measurements of the aerosol PNC and the atmospheric electricity during a Saharan dust event are unique data that have never been measured in this way before and may help to solve the question in which way the particle charge contributes to particle transport. The development of such relatively complex and versatile measurement systems on UAS has only recently become technically feasible, as the continuous development of smaller, better, and cheaper sensors, autopilot systems, and onboard computers has made it possible to build such a system. However, the construction and operation of such a system and the analysis of such complex measurement data is still challenging and requires a multidisciplinary approach as well as well-trained personnel. Due to increasingly restrictive regulations for the operation of UAS, the organizational effort is also increasing, at least in Europe.

5.1 High-resolution Wind Field Measurements

We have successfully used the high-resolution wind, temperature, and humidity measurement system on MASC-3 to record small-scale structures in the wind field of an Arctic fjord. The measurements in Kongsfjorden show that in the immediate vicinity of Ny-Ålesund, small-scale katabatic flows create significantly different wind conditions than a coarse-resolution weather model would suggest.

The two case studies from 01 May 2018 confirm the persistent flow along the fjord axis described in the existing literature (Svendsen et al., 2002). This is the main influence on the wind conditions in Ny-Ålesund, leading to the most common wind direction being ESE to SE. As of writing this thesis summary, this flow aligned with the fjord axis has been described for additional fjords on Svalbard and has been described as “Arctic Fjord Breeze” (Henkies et al., 2023).

In the valley west of Ny-Ålesund, the Broggerdalen, MASC-3 captured a katabatic flow close to the ground, transporting cold air from the glaciers in the south and southwest to the fjord (Fig. 8). A 2D slice of the flight measurement of wind speed and wind direction clearly shows how the cold air mass from Broggerdalen moves near the ground towards the fjord (Fig. 7).

However, the measurements presented here are only case studies. This is a limitation of UAS measurements in general, at least at the current time: Most research UAS in use today require a team on the ground during the flight, or at minimum a safety pilot. There are also restrictions on the operation of UAS in many places, for example at night. This makes it challenging to use UAS to collect continuous statistics, in this case, on the wind field in Kongsfjorden. In addition, the MASC-3 presented here (and UAS in general) have limitations with respect to weather conditions. In the case of MASC-3, it cannot fly in precipitation, heavy fog, or wind speeds above 15 m s^{-1}. These limitations must be taken into account when attempting to capture statistically relevant data with UAS.

5.2 Atmospheric Charge Measurement

One of the novel aspects of this research was the measurement of atmospheric charge using UAS. This work demonstrates that it is possible to measure atmospheric charge with high accuracy and low noise using MASC-3. This was demonstrated by measuring the space charge during a flyby of a 100 m metal tower.

During the validation of the charge sensors on MASC-3, it was shown the movement of MASC-3 around its axes has a significant effect on the measurement with the charge sensors. A rolling motion of the aircraft generates a signal in the charge sensors mounted on the wing. The faster the roll, the greater the amplitude of this signal. By using a filter function that takes the roll rate measured by the on-board INS as input, it was possible to eliminate the influence of this roll motion from the charge sensor readings. Charge sensors were also used to measure PNC during a Saharan dust event in Cyprus. The interpretation of the results of these measurements concerning the relationship between PNC and atmospheric charge is still in preparation at the time of writing (Savvakis et al., 2024c), but a preliminary analysis of the measurement data shows a clear relationship between aerosol particle concentration and charge sensor output (Fig. 18). This result may be due to the dust particles being charged or the charging of the aircraft fuselage itself. Since the test flights covered in this work presented here took place in good weather and clean air, there was no significant source of fuselage charging. However, it has been described in the literature that an aircraft can become charged when there are high concentrations of aerosol particles, such as in dust clouds.

Such a linear relationship between charge sensor output and aerosol particle concentration is unexpected since, when flying through a dust cloud, one would expect a signal in the charge sensors primarily when entering and leaving the dust cloud (i.e., where the E-field changes most rapidly, see also Fig. 2). This initial analysis, therefore, suggests that static charging of the fuselage itself occurs when flying through the dust cloud, similar to that described in (Lekas, 2019). These data will be further analyzed in an upcoming publication by Savvakis et al.

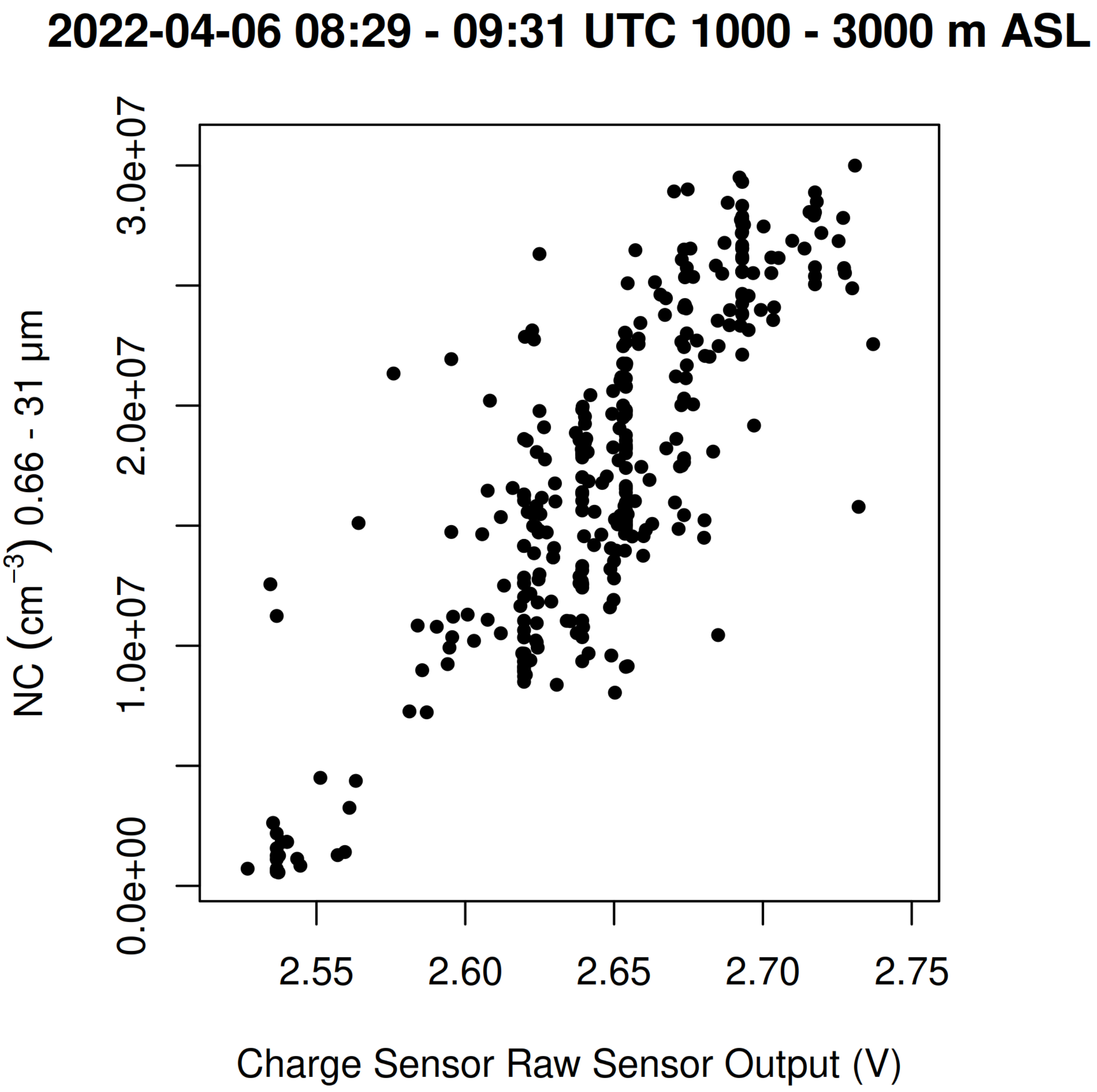

Figure 18. Particle number concentration and magnitude of the raw charge sensor signal recorded by MASC-3 during a measurement flight on 6 April 2022 over Orounda, Cyprus, during a Saharan dust event. Data corresponds to an ascent to 3000 m ASL and the subsequent descent. Data is averaged for every 10 m of altitude.

5.3 Aerosol Particle Measurement with the OPC-Pod

The development and validation of the OPC-Pod is one of several independently developed particle measurement systems for use on small UAS in recent years (e.g. Smith et al., 2019; Renard et al., 2018; Altstädter et al., 2015; Bates et al., 2013). The OPC-Pod differs from these systems by combining four key features:

- Low weight
- Low cost, based on a commercially available sensor (Alphasense OPC-N3)
- Detection of particle size distribution over a wide size range (24 bins from 0.46 - 25 µm)
- Integrated drying channel to compensate for hygroscopic growth

The comparative experiments with the environmental monitoring station in Mannheim (Fig. 14) demonstrated the critical role of particle drying, highlighting hygroscopic growth as a critical factor in aerosol measurement.

The lightweight and compact design of the OPC-Pod is aided by the passive aspiration system, which ensures that a constant volume flow at a constant dynamic pressure passes through the particle sensor via the ”wing profile” of the OPC-Pod. Since the dynamic pressure is directly dependent on the indicated airspeed and is kept constant during flight by the MASC-3 autopilot, there is no need for complicated (and heavy) control of the sample airflow by a pump.

This compact and lightweight design allows it to be mounted alongside other meteorological sensors on a UAS and opens up new possibilities for comprehensive, multi-parameter atmospheric studies.

However, the limitations of this sensor system must also be mentioned. Although the low-cost OPC-N3 shows very good performance compared to the reference device in Mannheim, there is a strong overestimation of PNC in the smallest bin size compared to the reference device and also to another OPC-N3. This indicates that the performance varies between individual instances of the OPC-N3. This would have to be investigated in more detail in follow-up studies or taken into account if the OPC-N3 is to be used operationally.

The OPC-Pod also differs in the measured size distribution from the UCASS and an unmodified OPC-N3 operated in the wind tunnel. With the OPC-Pod, the size distribution is shifted toward larger particles, which was expected because the OPC-Pod samples sub-isokinetically, meaning that larger particles are preferentially detected due to their higher inertia (Fig. 5).

Finally, a disadvantage of the OPC-Pod’s diffusion dryer is that the desiccant (silica gel) has to be replaced periodically. This is not a problem when using the OPC-Pod in scientific measurement campaigns, as the desiccant can simply be replaced after each flight. However, if this type of diffusion dryer is to be used over an extended period of time in a fixed location or without human intervention, this limitation must be taken into account.

6 CONCLUSION

In an increasingly interconnected world, where the need to predict, understand, and mitigate weather events is growing, so is the need for more detailed measurements. Ultimately, in-situ measurements are just one link in the chain that leads to a better understanding of the atmosphere and, ultimately, to high-resolution, accurate numerical models that directly impact human actions. Nevertheless, they are crucial because they give us direct information about the atmosphere and provide the closest possible view of the processes that take place in it.

MASC-3 as a small UAS, with its extensive sensor payload and considerable flight performance compared to its size and the required logistical effort, shows how useful airborne measurements are in this context. Small UAS, in contrast to manned aircraft, are particularly good at resolving the ABL close to the ground, where, ultimately, the processes most relevant to humans take place.

The measurements of the space charge on board a UAS presented in this paper are unique and demonstrate new possibilities to reliably measure this relatively neglected parameter at high resolution and, above all, to put it into context by simultaneously measuring other parameters. The simultaneous in-situ measurement of wind, temperature, humidity, particle size distribution, and atmospheric charge from a small UAS represents a significant methodological advance. The dataset acquired during the Saharan dust event in Cyprus is unique in that it combines the measurement of PNC and atmospheric charge, which may help to solve questions regarding the involvement of electrical charge in the long-range transport of large dust particles.

High-resolution measurements of wind, temperature, and humidity are very valuable for the study of aerosol particle transport because they allow better differentiation between different air masses. In addition, the influence of turbulent processes on particle transport and new particle formation can be studied. The availability of meteorological parameters and aerosol particle concentration also helps in follow-up studies, as the data can be used to initialize numerical models.

7 OUTLOOK

While MASC-3 demonstrates the great potential of on-board measurements from small UAS, there are still a number of issues that can be addressed in future work. Some of these are more methodological issues and some are still open questions about the atmospheric processes described here.

7.1 Methodic Improvements

From a methodological point of view, some improvements to the OPC-Pod are conceivable that would further improve the measurement results.

- The refractive index of the measured particles should be included in the post-processing. This could improve the precision of the particle size distribution, especially when measuring a relatively homogeneous aerosol with a known particle type.

- The OPC-Pod would benefit from an isokinetic inlet to reduce the observed bias from sub-isokinetic sampling.
- In the present measurements, both the OPC-Pod and the UCASS system measured mainly smaller particles below 20 µm in diameter. The Alphasense OPC-N3 sensor installed in the OPC-Pod is particularly interesting for measuring dust events because, unlike other low-cost OPCs, it can measure large particles up to 40 µm in diameter. However, the measurement of such large particles was not validated in the present work and would need to be investigated in future experiments.

When measuring space charge, the aforementioned influence of the static charge of the aircraft itself is an important point, which will be investigated in an upcoming publication by Savvakis et al. The charge measurements at Falkenberg Observatory presented here are not affected by this, but the strong relationship between PNC and space charge measurements during the Sahara Dust event indicate that this might be an issue during Saharan dust measurements. With respect to UAS measurements in general, some steps still need to be taken to make the systems capable of continuous measurements in all weather conditions (precipitation, high winds). The need for a ground crew within sight of the aircraft also limits the ability to make statistically relevant continuous measurements. For example, during the measurements at Ny-Ålesund, it was often not possible to perform measurements because the ground crew for MASC-3 could only perform flight operations during the daytime while the research station was occupied. Further, flight measurements had to be interrupted for crewed air traffic for safety reasons. A fully autonomous UAS capable of continuous operations would be useful here.

7.2 Further research

The Saharan dust event recorded by MASC-3 in Cyprus provides a unique data set that needs to be further investigated. The data set is particularly interesting in terms of the interplay between atmospheric charge and particle concentration. The data set could also be used for comparison with reanalysis models and remote sensing data. It would also be interesting to find out why the fraction of large particles larger than 20 µm is relatively small in this dust event and to what extent the near-ground aerosol particles also belong to the dust event or are locally generated particles.

For future campaigns, it would be interesting to equip MASC-3 with several OPC pods, one with a particle dryer and another one measuring the ambient (non-dried) particles. This would make it possible to quantify the contribution of hygroscopic growth to the aerosol particle measurement, and even more information about the nature of the aerosol particles measured could be obtained by comparing the two instruments.

The immediate next step is to study the electrical charge of the dust particles from the Cyprus dataset and acquire more data on Saharan dust events. We hope to answer questions about the amount of charge carried by the transported dust particles, to better understand the processes leading to particle charging, and to get information about the influence of charge on the deposition of the dust particles.

REFERENCES

Alphasense, 2019: User Manual: OPC-N3 Optical Particle Counter. Accessed 19 May 2022, https://www.alphasense.com/wp-content/uploads/2019/03/OPC-N3.pdf.

Altstädter, B., A. Platis, B. Wehner, A. Scholtz, N. Wildmann, M. Hermann, R. Käthner, H. Baars, J. Bange, and A. Lampert, 2015: ALADINA–an unmanned research aircraft for observing vertical and horizontal distributions of ultrafine particles within the atmospheric boundary layer. *Atmos. Meas. Tech.*, **8 (4)**, 1627–1639, doi: 10.5194/amt-8-1627-2015.

Bahlouli, A. E., A. Rautenberg, M. Schön, K. zum Berge, J. Bange, and H. Knaus, 2019: Comparison of CFD Simulation to UAS Measurements for Wind Flows in Complex Terrain: Application to the WINSENT Test Site. *Energies*, **12**, 1992, doi: 10.3390/en12101992.

Bates, T., P. Quinn, J. Johnson, A. C. F.J., B. S.E., Stalin, C. Meinig, and J. F. Burkhart, 2013: Measurements of atmospheric aerosol vertical distributions above Svalbard, Norway, using unmanned aerial systems (UAS). *Atmos. Meas. Tech.*, **6 (8)**, 2115–2120, doi: 10.5194/amt-6-2115-2013.

Belyaev, S. P., and L. M. Levin, 1972: Investigation of aerosol aspiration by photographing particle tracks under flash illumination. *J. Aerosol Sci.*, **3 (2)**, 127–140, doi: 10.1016/0021-8502(72)90149-8.

Bramati, M., M. Schön, D. Schulz, V. Savvakis, Y. Wang, J. Bange, and A. Platis, 2024: A Versatile Calibration Method for Rotary-Wing UAS as Wind Measurement Systems. *J. Atmos. Oceanic Technol.*, **41 (1)**, 25–43, doi: 10.1175/JTECH-D-23-0010.1.

Brockmann, J. E., 2011: Aerosol Transport in Sampling Lines and Inlets. *Aerosol Measurement: Principles, Techniques, and Applications*, P. Kulkarni, P. A. Baron, and K. Willeke, Eds., Wiley-Blackwell, 68–105, doi: 10.1002/9781118001684.ch6.

Chung, C. E., 2012: Aerosol direct radiative forcing: a review. *Atmospheric Aerosols: Regional Characteristics - Chemistry and Physics*, H. Abdul-Razzak, Ed., IntechOpen, 379–394, doi: 10.5772/2695.

Dhaniyala, S., M. Fierz, J. Keskinen, and M. Marjamäki, 2011: Instruments Based on Electrical Detection of Aerosols. *Aerosol Measurement: Principles, Techniques, and Applications*, P. Kulkarni, P. A. Baron, and K. Willeke, Eds., Wiley-Blackwell, 393–416, doi: 10.1002/9781118001684.ch18.

Dusek, U., G. P. Frank, L. Hildebrandt, J. Curtius, J. Schneider, S. Walter, D. Chand, F. Drewnick, S. Hings, D. Jung, S. Borrmann, and M. O. Andreae, 2006: Size Matters More Than Chemistry for Cloud-Nucleating Ability of Aerosol Particles. *Science*, **312 (5778)**, 1375–1378, doi: 10.1126/science.1125261.

Ensor, D. S., and A. M. Dixon, 2011: Aerosol Measurements in Cleanrooms. *Aerosol Measurement: Principles, Techniques, and Applications*, P. Kulkarni, P. A. Baron, and K. Willeke, Eds., Wiley-Blackwell, 771–784, doi: 10.1002/9781118001684.ch36.

Esposito, F., R. Molinaro, C. I. Popa, C. Molfese, F. Cozzolino, L. Marty, K. Taj-Eddine, G. D. Achille, G. Franzese, S. Silvestro, and G. G. Ori, 2016: The role of the atmospheric electric field in the dust-lifting process. *Geophys. Res. Lett.*, **43 (10)**, 5501–5508, doi: 10.1002/2016GL068463.

Fiedler, S., K. Schepanski, B. Heinold, P. Knippertz, and I. Tegen, 2013: Climatology of nocturnal low-level jets over North Africa and implications for modeling mineral dust emission. *J. Geophys. Res. Atmos.*, **118**, 6100–6121, doi: 10.1002/jgrd.50394.

Formenti, P., L. Schütz, Y. Balkanski, K. Desboeufs, M. Ebert, K. Kandler, A. Petzold, D. Scheuvens, S. Weinbruch, and D. Zhang, 2011: Recent progress in understanding physical and chemical properties of African and Asian mineral dust. *Atmos. Chem. Phys.*, **11 (16)**, 8231–8256, doi: 10.5194/acp-11-8231-2011.

Gabbi, J., M. Huss, A. Bauder, F. Cao, and M. Schwikowski, 2015: The Impact of Saharan Dust and Black Carbon on Albedo and Long-term Mass Balance of an Alpine Glacier. *The Cryosphere*, **9 (4)**, 1385–1400, doi: 10.5194/tc-9-1385-2015.

Gish, O. H., 1944: Evaluation and interpretation of the columnar resistance of the atmosphere. *Terr. Magn. Atmos. Electr.*, **49 (3)**, 159–168, doi: https://doi.org/10.1029/TE049i003p00159.

Gringel, W., and R. Muhleisen, 1978: Sahara Dust Concentration in the Troposphere over the North Atlantic Derived from Measurements of Air Conductivity. *Beiträge zur Physik der Atmosphäre*, **51 (121)**.

Gupta, N. N. D., and S. K. Ghosh, 1946: A Report on the Wilson Cloud Chamber and Its Applications in Physics. *Reviews of Modern Physics*, **18**, 225–290, doi: 10.1103/RevModPhys.18.225.

Harm-Altstädter, B., K. Bärfuss, L. Bretschneider, M. Schön, J. Bange, R. Käthner, R. Krejci, M. Mazzola, K. Park, F. Pätzold, A. Peuker, R. Traversi, B. Wehner, and A. Lampert, 2023: Spatial distribution and variability of boundary layer aerosol particles observed in Ny-Ålesund during late spring in 2018. *Aerosol Research*, **1 (1)**, 39–64, doi: 10.5194/ar-1-39-2023.

Harrison, G., and A. Bennett, 2021: Electricity Measurements. *Springer Handbook of Atmospheric Measurements*, T. Foken, Ed., Springer Publishing, 431–456, doi: 10.1007/978-3-030-52171-4_14.

Harrison, R. G., K. A. Nicoll, D. J. Tilley, G. J. Marlton, S. Chindea, G. P. Dingley, P. Iravani, D. J. Cleaver, J. L. du Bois, and D. Brus, 2021: Demonstration of a Remotely Piloted Atmospheric Measurement and Charge Release Platform for Geoengineering. *J. Atmos. Oceanic Technol.*, **38 (1)**, 63–75, doi: 10.1175/JTECH-D-20-0092.1.

Heintzenberg, J., 2009: The SAMUM-1 experiment over Southern Morocco: overview and introduction. *Tellus B*, **61 (1)**, 2–11, doi: 10.1111/j.1600-0889.2008.00403.x.

Heintzenberg, J., 2012: The Aerosol-Cloud-Climate Conundrum. *International Journal of Global Warming*, **4**, 219–241, doi: 10.1504/IJGW.2012.049438.

Held, A., and A. Mangold, 2022: Measurement of Fundamental Aerosol Physical Properties. *Springer Handbook of Atmospheric Measurements*, T. Foken, Ed., Springer Publishing, Cham, 533–559, doi: 10.1007/

978-3-030-52171-4_18.

Henkies, M., K. V. Høyland, and A. Shestov, 2023: The Arctic Fjord Breeze: Characteristics of a Combined Sea Breeze and Valley Wind in a Svalbard Fjord Valley. *Boundary-Layer Meteorol*, **189**, 281–304, doi: 10.1007/s10546-023-00840-y.

Hill, R. D., 1971: Spherical Capacitor Hypothesis of the Earth's Electric Field. *Pure Appl. Geophys.*, **84**, 67–74, doi: 10.1007/BF00875454.

Hinds, W. C., and Y. Zhu, 2022: Introduction. *Aerosol Technology: Properties, Behavior, and Measurement of Airborne Particles*, Wiley-Blackwell, 1–14.

Howard, L., 1865: Essay on the Modifications of Clouds. *Essay on the Modifications of Clouds*, Cambridge University Press, 1–37, doi: 10.1017/CBO9781139096966.

Husar, R. B., J. D. Husar, and L. Martin, 2000: Distribution of Continental Surface Aerosol Extinction Based on Visual Range Data. *Atmos. Environ.*, **34**, 5067–5078, doi: 10.1016/S1352-2310(00)00324-1.

Jaenicke, R., 1980: Natural aerosols. *Annals of the New York Academy of Sciences*, **338 (1)**, 317–329, doi: https://doi.org/10.1111/j.1749-6632.1980.tb17129.x.

John, W., 2011: Size Distribution Characteristics of Aerosols. *Aerosol Measurement: Principles, Techniques, and Applications*, P. Kulkami, P. A. Baron, and K. Willeke, Eds., Wiley-Blackwell, 41–54, doi: 10.1002/9781118001684.ch4.

Kim, M.-H., A. H. Omar, J. L. Tackett, M. A. Vaughan, D. M. Winker, C. R. Trepte, Y. Hu, Z. Liu, L. R. Poole, M. C. Pitts, J. Kar, and B. E. Magill, 2018: The CALIPSO version 4 automated aerosol classification and lidar ratio selection algorithm. *Atmos. Meas. Tech.*, **11**, 6107–6135, doi: 10.5194/amt-11-6107-2018.

Koshak, W. J., J. Bailey, H. J. Christian, and D. M. Mach, 1994: Aircraft electric field measurements: Calibration and ambient field retrieval. *J. Geophys. Res.: Atmos.*, **99 (D11)**, 22 781–22 792, doi: https://doi.org/10.1029/94jd01682.

Kurppa, M., P. Roldin, J. Strömberg, A. Balling, S. Karttunen, H. Kuuluvainen, J. V. Niemi, L. Pirjola, T. Rönkkö, H. Timonen, A. Hellsten, and L. Järvi, 2020: Sensitivity of spatial aerosol particle distributions to the boundary conditions in the PALM model system 6.0. *Geosci. Model Dev.*, **13 (11)**, 5663–5685, doi: 10.5194/gmd-13-5663-2020.

Kwon, H.-S., M. H. Ryu, and C. Carlsten, 2020: Ultrafine particles: unique physicochemical properties relevant to health and disease. *Exp. Mol. Med.*, **52**, 318–328, doi: 10.1038/s12276-020-0405-1.

Lagzi, I. L., R. Mészáros, G. Gelybó, and Á. Leelőssy, 2013: Dispersion of Air Pollutants. *Atmospheric Chemistry*, I. L. Lagzi, R. Mészáros, G. Gelybó, and Á. Leelőssy, Eds., Eötvös Loránd University, 102–126.

Law, K. S., and A. Stohl, 2007: Arctic Air Pollution: Origins and Impacts. *Science*, **315 (5818)**, 1537–1540, doi: 10.1126/science.1137695.

Leinonen, V., H. Kokkola, T. Yli-Juuti, T. Mielonen, T. Kühn, T. Nieminen, S. Heikkinen, T. Miinalainen, T. Bergman, K. Carslaw, S. Decesari, M. Fiebig, T. Hussein, N. Kivekäs, R. Krejci, M. Kulmala, A. Leskinen, A. Massling,

N. Mihalopoulos, J. P. Mulcahy, S. M. Noe, T. van Noije, F. M. O'Connor, C. O'Dowd, D. Olivie, J. B. Pernov, T. Petäjä, Ø. Seland, M. Schulz, C. E. Scott, H. Skov, E. Swietlicki, T. Tuch, A. Wiedensohler, A. Virtanen, and S. Mikkonen, 2022: Comparison of Particle Number Size Distribution Trends in Ground Measurements and Climate Models. *Atmos. Chem. Phys.*, **22** **(19)**, 12 873–12 905, doi: 10.5194/acp-22-12873-2022.

Lekas, T. I., 2019: Electrostatic charging of an aircraft due to airborne dust particles impacts. *CEAS Aeronaut. J.*, **10**, 903–908, doi: 10.1007/s13272-018-00355-0.

Leukauf, D., A. El-Bahlouli, K. zum Berge, M. Schön, H. Knaus, and J. Bange, 2019: The impact of a forest parametrization on coupled WRF-CFD simulations during the passage of a cold front over the WINSENT test-site. *Wind Energy Science*, **2019**, 1–24, doi: 10.5194/wes-2019-68.

Levin, Z., A. Teller, E. Ganor, and Y. Yin, 2005: On the interactions of mineral dust, sea-salt particles, and clouds: A measurement and modeling study from the mediterranean israeli dust experiment campaign. *J. Geophys. Res.: Atmos.*, **110** **(D20)**, doi: 10.1029/2005JD005810.

Li, J., B. E. Carlson, Y. L. Yung, D. Lv, J. Hansen, J. E. Penner, H. Liao, V. Ramaswamy, R. A. Kahn, P. Zhang, O. Dubovik, A. Ding, A. A. Lacis, L. Zhang, and Y. Dong, 2022: Scattering and Absorbing Aerosols in the Climate System. *Nat. Rev. Earth Environ.*, **3** **(6)**, 363–379, doi: 10.1038/s43017-022-00296-7.

Lohmann, U., and J. Feichter, 2005: Global Indirect Aerosol Effects: A Review. *Atmos. Chem. Phys.*, **5** **(3)**, 715–737, doi: 10.5194/acp-5-715-2005.

Mach, D. M., 2015: Technique for reducing the effects of nonlinear terms on electric field measurements of electric field sensor arrays on aircraft platforms. *J. Atmos. Oceanic Technol.*, **32** **(5)**, 993–1003, doi: https://doi.org/10.1175/jtech-d-14-00029.1.

Mach, D. M., and W. J. Koshak, 2007: General matrix inversion technique for the calibration of electric field sensor arrays on aircraft platforms. *J. Atmos. Oceanic Technol.*, **24** **(9)**, 1576–1587, doi: https://doi.org/10.1175/jtech2080.1.

Malina, C., and F. Scheffler, 2015: The impact of Low Emission Zones on particulate matter concentration and public health. *Transportation Research Part A: Policy and Practice*, **77**, 372–385, doi: 10.1016/j.tra.2015.04.029.

Marinescu, P. J., S. C. van den Heever, S. M. Saleeby, S. M. Kreidenweis, and P. J. DeMott, 2017: The Microphysical Roles of Lower-Tropospheric versus Midtropospheric Aerosol Particles in Mature-Stage MCS Precipitation. *J. Atmos. Sci.*, **74** **(11)**, 3657–3678, doi: 10.1175/JAS-D-16-0361.1.

Mashni, H., H. Knaus, A. Platis, and J. Bange, 2023: Development of an airfoil-based passive volumetric air sampling and flow control system for fixed-wing UAS. *Bull. Atmos. Sci. Technol.*, **4**, 6, doi: 10.1007/s42865-023-00057-4.

Mauz, M., B. van Kesteren, W. Junkermann, K. zum Berge, M. Schön, A. Platis, and J. Bange, 2020: Miniature high-frequency chilled-mirror hygrometer for atmospheric measurements aboard fixed wing UAS. *Meteor. Z.*, **29** **(6)**, 439–449, doi: 10.1127/metz/2020/1026.

Miao, Y., H. Che, X. Zhang, and S. Liu, 2020: Integrated impacts of synoptic forcing and aerosol radiative effect on boundary layer and pollution in the Beijing–Tianjin–Hebei region, China. *Atmos. Chem. Phys.*, **20 (10)**, 5899–5909, doi: 10.5194/acp-20-5899-2020.

Nicoll, K. A., 2013: A self-calibrating electrometer for atmospheric charge measurements from a balloon platform. *Rev. Sci. Instrum*, **84 (9)**, 096 107, doi: https://doi.org/10.1063/1.4821500.

Nicoll, K. A., and R. G. Harrison, 2009: A lightweight balloon-carried cloud charge sensor. *Rev. Sci. Instrum.*, **80 (1)**, 014 501, doi: https://doi.org/10.1063/1.3065090.

Nicoll, K. A., A. Readle, A. A. Kamali, and R. G. Harrison, 2022: Surface atmospheric electric field variability at a desert site. *Journal of Atmospheric and Solar-Terrestrial Physics*, **241**, 105 977, doi: 10.1016/j.jastp.2022.105977.

O'Sullivan, D., F. Marenco, C. L. Ryder, Y. Pradhan, Z. Kipling, B. Johnson, A. Benedetti, M. Brooks, M. McGill, J. Yorks, and P. Selmer, 2020: Models transport Saharan dust too low in the atmosphere: a comparison of the MetUM and CAMS forecasts with observations. *Atmos. Chem. Phys.*, **20 (21)**, 12 955–12 982, doi: 10.5194/acp-20-12955-2020.

Pai, S. J., T. S. Carter, C. L. Heald, and J. H. Kroll, 2022: Updated World Health Organization Air Quality Guidelines Highlight the Importance of Non-anthropogenic PM2.5. *Environ. Sci. Technol. Lett.*, **9**, 501–506, doi: 10.1021/acs.estlett.2c00203.

Palas GmbH, 2023: Palas Fidas Frog Technical Features. Accessed 15 November 2023, https://www.palas.de/product/fidasfrog.

Papadimas, C. D., N. Hatzianastassiou, C. Matsoukas, M. Kanakidou, N. Mihalopoulos, and I. Vardavas, 2012: The Direct Effect of Aerosols on Solar Radiation Over the Broader Mediterranean Basin. *Atmos. Chem. Phys.*, **12 (15)**, 7165–7185, doi: 10.5194/acp-12-7165-2012.

Petäjä, T., E.-M. Duplissy, K. Tabakova, J. Schmale, B. Altstädter, G. Ancellet, M. Arshinov, Y. Balin, U. Baltensperger, J. Bange, A. Beamish, B. Belan, A. Berchet, R. Bossi, W. R. L. Cairns, R. Ebinghaus, I. E. Haddad, B. Ferreira-Araujo, A. Franck, L. Huang, A. Hyvärinen, A. Humbert, A.-C. Kalogridis, P. Konstantinov, A. Lampert, M. MacLeod, O. Magand, A. Mahura, L. Marelle, V. Masloboev, D. Moisseev, V. Moschos, N. Neckel, T. Onishi, S. Osterwalder, A. Ovaska, P. Paasonen, M. Panchenko, F. Pankratov, J. B. Pernov, A. Platis, O. Popovicheva, J.-C. Raut, A. Riandet, T. Sachs, R. Salvatori, R. Salzano, L. Schröder, M. Schön, V. Shevchenko, H. Skov, J. E. Sonke, A. Spolaor, V. K. Stathopoulos, M. Strahlendorff, J. L. Thomas, V. Vitale, S. Vratolis, C. Barbante, S. Chabrillat, A. Dommergue, K. Eleftheriadis, J. Heilimo, K. S. Law, A. Massling, S. M. Noe, J.-D. Paris, A. S. H. Prévôt, I. Riipinen, B. Wehner, Z. Xie, and H. K. Lappalainen, 2020: Overview: Integrative and Comprehensive Understanding on Polar Environments (iCUPE) – concept and initial results. *Atmos. Chem. Phys.*, **20 (14)**, 8551–8592, doi: 10.5194/acp-20-8551-2020.

Preining, O., 1991: Aerosol and Climate: An Overview. *Atmospheric Environment. Part A, General Topics*, **25 (11)**, 2443–2444, doi: 10.1016/0960-1686(91)90160-9.

Quincey, P., and D. Butterfield, 2009: Ambient air particulate matter PM10 and PM2.5: developments in european measurement methods and legislation. *Biomarkers*, **14 (sup1)**, 34–38, doi: 10.1080/13547500902965484.

Quinn, P. K., G. Shaw, E. Andrews, E. G. Dutton, T. Ruoho-Airola, and S. L. Gong, 2007: Arctic haze: current trends and knowledge gaps. *Tellus B*, **59 (1)**, 99–114, doi: 10.1111/j.1600-0889.2006.00238.x.

Rautenberg, A., M. Schön, K. zum Berge, M. Mauz, P. Manz, A. Platis, B. van Kesteren, I. Suomi, S. T. Kral, and J. Bange, 2019: The Multi-Purpose Airborne Sensor Carrier MASC-3 for Wind and Turbulence Measurements in the Atmospheric Boundary Layer. *Sensors*, **19 (10)**, 2292, doi: 10.3390/s19102292.

Renard, J. B., F. Dulac, P. Durand, Q. Bourgeois, C. Denjean, D. Vignelles, B. Couté, M. Jeannot, N. Verdier, and M. Mallet, 2018: In situ measurements of desert dust particles above the western Mediterranean Sea with the balloon-borne Light Optical Aerosol Counter/sizer (LOAC) during the ChArMEx campaign of summer 2013. *Atmos. Chem. and Physics*, **18 (5)**, 3677–3699, doi: 10.5194/acp-18-3677-2018.

Reuder, J., M. O. Jonassen, and H. Ólafsson, 2012: The Small Unmanned Meteorological Observer SUMO: Recent developments and applications of a micro-UAS for atmospheric boundary layer research. *Acta Geophysica*, **60**, 1454–1473, doi: 10.2478/s11600-012-0042-8.

Rycroft, M. J., R. G. Harrison, K. A. Nicoll, and E. A. Mareev, 2008: An Overview of Earth's Global Electric Circuit and Atmospheric Conductivity. *Space Sci. Rev.*, **137**, 83–105, doi: 10.1007/s11214-008-9368-6.

Ryder, C., F. Marenco, J. Brooke, V. Estelles, R. Cotton, P. Formenti, J. McQuaid, H. Price, D. Liu, P. Ausset, P. Rosenberg, J. Taylor, T. Choularton, K. Bower, H. Coe, M. Gallagher, J. Crosier, G. Lloyd, E. Highwood, and B. Murray, 2018: Coarse-mode mineral dust size distributions, composition and optical properties from AER-D aircraft measurements over the tropical eastern Atlantic. *Atmos. Chem. Phys.*, **18 (23)**, 17 225–17 257, doi: 10.5194/acp-18-17225-2018.

Savvakis, V., M. Schön, M. Bramati, J. Bange, and A. Platis, 2024a: Calculation of aerosol particle hygroscopic properties from OPC derived PM2.5 data. *Meteorol. Z.*, doi: 10.1127/metz/2024/1198.

Savvakis, V., M. Schön, M. Bramati, J. Bange, and A. Platis, 2024b: Small-Scale Diffusion Dryer on an Optical Particle Counter for High-Humidity Aerosol Measurements with an Uncrewed Aircraft System. *J. Atmos. Oceanic Technol.*, **41 (3)**, 205–219, doi: 10.1175/JTECH-D-23-0093.1.

Savvakis, V., M. Schön, K. A. Nicoll, C. L. Ryder, A. Papetta, M. Kezoudi, F. Marenco, J. Bange, and A. Platis, 2024c: In-situ observations of charged Saharan dust from an uncrewed aircraft system. *Aerosol Sci. Technol.*, **in review**.

Schön, M., K. A. Nicoll, Y. G. Büchau, S. Chindea, A. Platis, and J. Bange, 2022a: Fair Weather Atmospheric Charge Measurements with a Small UAS. *J. Atmos. Oceanic Technol.*, **39 (11)**, 1799–1813, doi: 10.1175/JTECH-D-22-0025.1.

Schön, M., V. Savvakis, M. Ketsoudi, A. Platis, and J. Bange, 2024: OPC-Pod: A New Sensor Payload to Measure Aerosol Particles for Small Uncrewed Aircraft Systems. *J. Atmos. Oceanic Technol.*, **early online release**, doi: 10.1175/JTECH-D-23-0078.1.

Schön, M., K. zum Berge, A. Platis, and J. Bange, 2022b: UAS-based measurement of wind vector, temperature and humidity in Ny-Ålesund, Svalbard, during April and May 2018. PANGAEA, doi: 10.1594/PANGAEA.946961.

Schön, M., I. Suomi, B. Altstädter, B. van Kesteren, K. zum Berge, A. Platis, B. Wehner, A. Lampert, and J. Bange, 2022c: Case studies of the wind field around Ny-Ålesund, Svalbard, using unmanned aircraft. *Polar Research*, **41**, doi: 10.33265/polar.v41.7884.

Schraufnagel, D. E., 2020: The health effects of ultrafine particles. *Exp. Mol. Med.*, **52 (3)**, 311–317, doi: 10.1038/s12276-020-0403-3.

Seinfeld, J. H., and S. N. Pandis, 2006: *Atmospheric Chemistry and Physics: From Air Pollution to Climate Change*. 2nd ed., Wiley-Blackwell, 1203 pp.

Silva, H. G., F. M. Lopes, S. Pereira, K. A. Nicoll, S. M. Barbosa, R. Conceição, S. Neves, R. G. Harrison, and M. C. Pereira, 2016: Saharan dust electrification perceived by a triangle of atmospheric electricity stations in Southern Portugal. *J. Electrostatics*, **84**, 106–120, doi: 10.1016/j.elstat.2016.10.002.

Smith, H. R., Z. Ulanowski, P. H. Kaye, E. Hirst, W. Stanley, R. Kaye, A. Wieser, C. Stopford, M. Kezoudi, J. Girdwood, R. Greenaway, and R. Mackenzie, 2019: The Universal Cloud and Aerosol Sounding System (UCASS): a low-cost miniature optical particle counter for use in dropsonde or balloon-borne sounding systems. *Atmos. Meas. Tech.*, **12 (12)**, 6579–6599, doi: 10.5194/amt-12-6579-2019.

Stein, A. F., R. R. Draxler, G. D. Rolph, B. J. B. Stunder, M. D. Cohen, and F. Ngan, 2015: NOAA's HYSPLIT Atmospheric Transport and Dispersion Modeling System. *Bull. Amer. Meteor. Soc.*, **96 (12)**, 2059–2077, doi: 10.1175/BAMS-D-14-00110.1.

Svendsen, H., A. Beszczynska-møller, J. O. Hagen, B. Lefauconnier, V. Tverberg, S. Gerland, J. B. Ørbæk, K. Bischof, C. Papucci, M. Zajaczkowski, R. Azzolini, O. Bruland, C. Wiencke, J.-G. Winther, and W. Dallmann, 2002: The physical environment of Kongsfjorden–Krossfjorden, an Arctic fjord system in Svalbard. *Polar Research*, **21 (1)**, 133–166, doi: 10.3402/polar.v21i1.6479.

Toth, J. R., S. Rajupet, H. Squire, B. Volbers, J. Zhou, L. Xie, R. M. Sankaran, and D. J. Lacks, 2020: Electrostatic forces alter particle size distributions in atmospheric dust. *Atmos. Chem. Phys.*, **20 (5)**, 3181–3190, doi: 10.5194/acp-20-3181-2020.

TSI Incorporated, 2021: Aerosol Statistics Application Note. Accessed 09 February 2024, https://tsi.com/getmedia/1621329b-f410-4dce-992b-e21e1584481a/PR-001-RevA_Aerosol-Statistics-AppNote.ext=.pdf, TSI Incorporated.

Ulanowski, Z., J. Bailey, P. W. Lucas, J. H. Hough, and E. Hirst, 2007: Alignment of atmospheric mineral dust due to electric field. *Atmos. Chem. Phys.*, **7 (24)**, 6161–6173, doi: 10.5194/acp-7-6161-2007.

van der Does, M., P. Knippertz, P. Zschenderlein, R. G. Harrison, and J.-B. W. Stuut, 2018: The mysterious long-range transport of giant mineral dust particles. *Sci. Adv.*, **4 (12)**, eaau2768, doi: 10.1126/sciadv.aau2768.

Varga, G., P. Dagsson-Waldhauserová, F. Gresina, and A. Helgadottir, 2021: Saharan dust and giant quartz particle transport towards Iceland. *Sci. Rep.*, **11 (1)**, 11 891, doi: 10.1038/s41598-021-91481-z.

Wang, C., 2013: Impact of Anthropogenic Absorbing Aerosols on Clouds and Precipitation: A Review of Recent Progresses. *Atmos. Res.*, **122**, 237–249, doi: 10.1016/j.atmosres.2012.11.005.

Watson-Parris, D., N. Schutgens, C. Reddington, K. J. Pringle, D. Liu, J. D. Allan, H. Coe, K. S. Carslaw, and P. Stier, 2019: In Situ Constraints on the Vertical Distribution of Global Aerosol. *Atmos. Chem. Phys.*, **19 (18)**, 11 765–11 790, doi: 10.5194/acp-19-11765-2019.

Whitby, K. T., 1978: The Physical Characteristics of Sulfur Aerosols. *Atmos. Environ.*, **12**, 135–159, doi: 10.1016/0004-6981(78)90196-8.

Wilcox, J. D., 1956: Isokinetic flow and sampling. *J. Air Pollut. Control Assoc.*, **5 (4)**, 226–245, doi: 10.1080/00966665.1956.10467715.

Wildmann, N., M. Mauz, and J. Bange, 2013: Two fast temperature sensors for probing of the Atmospheric Boundary Layer using small Remotely Piloted Aircraft (RPA). *Atmos. Meas. Tech.*, **6 (2)**, doi: 10.5194/amt-6-2101-2013.

Winn, W. P., 1993: Aircraft measurement of electric field: Self-calibration. *J. Geophys. Res.: Atmos.*, **98 (D4)**, 7351–7365, doi: https://doi.org/10.1029/93jd00165.

Yair, Y., S. Katz, R. Yaniv, B. Ziv, and C. Price, 2016: An electrified dust storm over the negev desert, israel. *Atmos. Res.*, **181**, 63–71, doi: 10.1016/j.atmosres.2016.06.011.

Yu, H., M. Chin, T. Yuan, H. Bian, L. A. Remer, J. M. Prospero, A. Omar, D. Winker, Y. Yang, Y. Zhang, Z. Zhang, and C. Zhao, 2015: The fertilizing role of African dust in the Amazon rainforest: A first multiyear assessment based on data from Cloud-Aerosol Lidar and Infrared Pathfinder Satellite Observations. *Geophys. Res. Lett.*, **42 (6)**, 1984–1991, doi: 10.1002/2015GL063040.

Zhao, P., S. Ge, J. Su, J. Ding, and Y. Kuang, 2022: Relative humidity dependence of hygroscopicity parameter of ambient aerosols. *J. Geophys. Res.: Atmos.*, **127 (8)**, e2021JD035 647, doi: 10.1029/2021JD035647.

Zheng, X.-J., 2013: Electrification of wind-blown sand: Recent advances and key issues. *The European Physical Journal E*, **36**, 138, doi: 10.1140/epje/i2013-13138-4.

zum Berge, K., M. Schön, M. Mauz, A. Platis, B. van Kesteren, D. Leukauf, A. E. Bahlouli, P. Letzgus, H. Knaus, and J. Bange, 2021: A Two-Day Case Study: Comparison of Turbulence Data from an Unmanned Aircraft System with a Model Chain for Complex Terrain. *Boundary-Layer Meteorology*, **180**, 53–78, doi: 10.1007/s10546-021-00608-2.

A PEER-REVIEWED FIRST-AUTHOR PUBLICATIONS

A.1 Case studies of the wind field around Ny-Ålesund, Svalbard, using unmanned aircraft

RESEARCH ARTICLE

Case studies of the wind field around Ny-Ålesund, Svalbard, using unmanned aircraft

Martin Schön,[1] Irene Suomi,[2] Barbara Altstädter,[3] Bram van Kesteren,[1] Kjell zum Berge,[1] Andreas Platis,[1] Birgit Wehner,[4] Astrid Lampert[3] & Jens Bange[1]

[1]Department of Geosciences, Tübingen University, Germany
[2]Finnish Meteorological Institute, Helsinki, Finland
[3]Technische Universität Braunschweig, Braunschweig, Germany
[4]Leibniz Institute for Tropospheric Research, Leipzig, Germany

Abstract

The wind field in Arctic fjords is strongly influenced by glaciers, local orography and the interaction between sea and land. Ny-Ålesund, an important location for atmospheric research in the Arctic, is located in Kongsfjorden, a fjord with a complex local wind field that influences measurements in Ny-Ålesund. Using wind measurements from UAS (unmanned aircraft systems), ground measurements, radiosonde and reanalysis data, characteristic processes that determine the wind field around Ny-Ålesund are identified and analysed. UAS measurements and ground measurements show, as did previous studies, a south-east flow along Kongsfjorden, dominating the wind conditions in Ny-Ålesund. The wind measured by the UAS in a valley 1 km west of Ny-Ålesund differs from the wind measured at the ground in Ny-Ålesund. In this valley, we identify a small-scale catabatic flow from the south to south-west as the cause for this difference. Case studies show a backing (counterclockwise rotation with increasing altitude) of the wind direction close to the ground. A katabatic flow is measured near the ground, with a horizontal wind speed up to 5 m s^{-1}. Both the larger-scale south-east flow along the fjord and the local katabatic flows lead to a highly variable wind field, so ground measurements and weather models alone give an incomplete picture. The comparison of UAS measurements, ground measurements and weather conditions analysis using a synoptic model is used to show that the effects measured in the case studies play a role in the Ny-Ålesund wind field in spring.

Keywords

Microscale meteorology; boundary layer; wind measurement; aircraft measurement; Kongsfjorden; Arctic fjord

Correspondence

Martin Schön, Department of Geosciences, Tübingen University, Schnarrenbergstraße 96, DE-72076 Tübingen, Germany.
Email: martin.schoen@uni-tuebingen.de

Abbreviations

ABL: atmospheric boundary layer
ALADINA: Application of Light-weight Aircraft for Detecting in situ Aerosols
AROME Arctic: Application of Research to Operations at Mesoscale (numerical weather prediction model, provided by the Norwegian Meteorological Institute)
ARTIST: Arctic Radiation and Turbulence Interaction Study (joint Finnish, German and Italian field measurement campaign with ground and airborne measurements, conducted in 1998 in Svalbard)
AWIPEV: Alfred Wegener Institute for Polar and Marine Research and Polar Institute Paul Emile Victor (joint German–French Arctic research station in Ny-Ålesund, Svalbard)
IMU: inertial measurement unit (GPS and movement sensors are combined to determine the position and movement vector of the vehicle carrying the IMU)
MASC: Multiple Purpose Airborne Sensor Carrier (electrically powered UAS with a wingspan of 4 m equipped with sensors to measure the wind vector, temperature and humidity in the ABL)
NILU: Norwegian Institute for Air Research
NWP: numerical weather prediction
SODAR: sonic detection and ranging (instrument for wind profiling)
UAS: unmanned aircraft system (includes aircraft capable of automatic flight, the controller on the ground and the sensor payload mounted on the aircraft)

Introduction

When researching the Arctic atmosphere to assess the impact of climate change, data from measurement stations play a significant role. For this reason, several internationally operated research stations in the Arctic provide long-term measurements. Located in Kongsfjorden, a fjord in north-west Spitsbergen, an island in the Svalbard archipelago (latitude: 78.923, longitude: 11.909; Figs. 1, 2), the village of Ny-Ålesund hosts 16 permanent stations from 10 different

Citation: *Polar Research* 2022, *41*, 7884, http://dx.doi.org/10.33265/polar.v41.7884

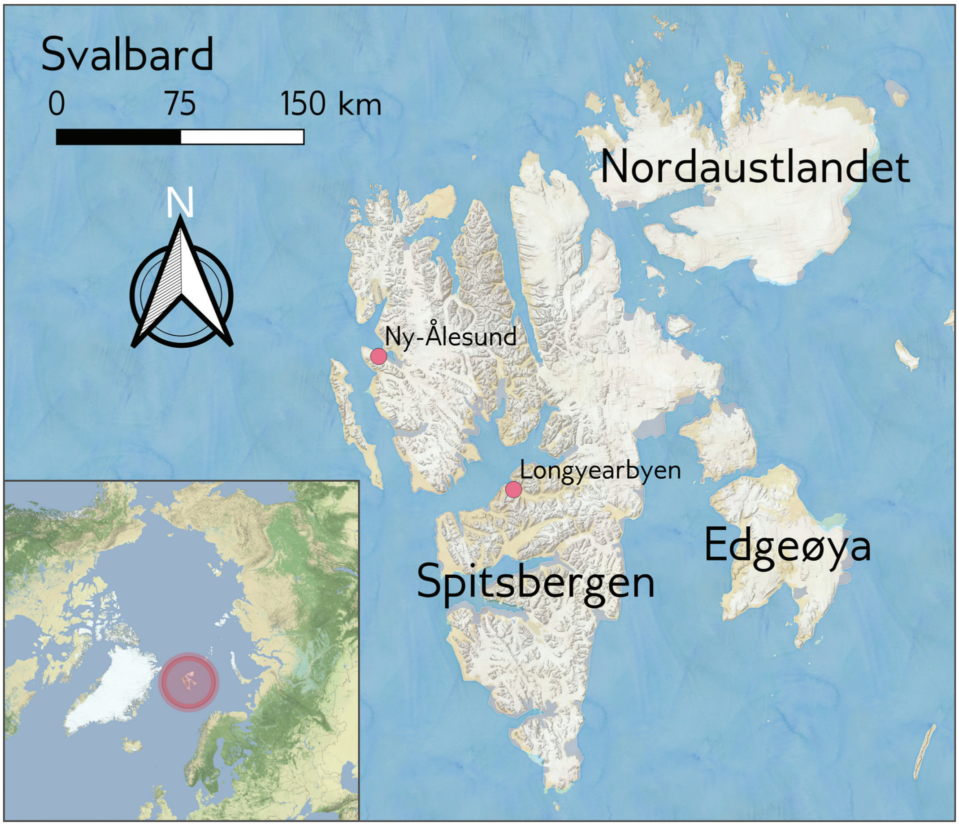

Fig. 1 Location of this survey, in Ny-Ålesund, on the island of Spitsbergen in the Svalbard archipelago. (Main map: Topo Svalbard, https://toposvalbard.npolar.no/, Norwegian Polar Institute. Inset map: Tiles by Stamen Design, under CC BY 3.0. Data by OpenStreetMap, under ODbL.)

countries. These research stations conduct meteorological, aerosol and trace gas measurements. Since local wind fields in Arctic fjords such as Kongsfjorden can deviate significantly from synoptic conditions (Svendsen et al. 2002), an understanding of this local wind field is crucial for the correct interpretation of the atmospheric measurements in Ny-Ålesund. For example, tethersonde measurements by Ferrero et al. (2016) show the importance of ABL properties like ground-based inversions and shear layers in the vertical wind profile for understanding the transport of aerosol particles. Aerosol particle measurements with the UAS ALADINA by the Technische Universität Braunschweig (Altstädter et al. 2015; Lampert et al. 2020; Petäjä et al. 2020) show the high vertical variability of aerosol concentration in the ABL and the need for understanding the local wind field influencing the transport processes.

The wind field in Arctic fjords such as Kongsfjorden is subjected to forcings by a highly variable terrain and significant thermal differences between open or frozen water and exposed soil or glacier ice. At larger scales, temperature differences between fjord water and open sea and synoptic processes play a role. Temperature and moisture inversions are common in the Arctic ABL (Egerer et al. 2021). Thermal differences between frozen and open water can lead to shallow convection and the development of internal boundary layers (Svendsen et al. 2002). Characteristic phenomena are low-level jets, which regularly occur because of katabatic flows (Vihma et al. 2011). Meltwater from the glaciers surrounding an Arctic fjord influences its water temperature. Cold, dense air flows from glaciers to the mouth of the fjord (Svendsen et al. 2002). In Kongsfjorden, these drainage flows often lead to higher wind speeds within the Arctic ABL, which typically has a depth of 250 m, and inverse wind directions compared to the synoptic conditions (Beine et al. 2001; Argentini et al. 2003).

For Arctic fjords, numerical models cannot reproduce these complex interactions reliably (Tjernström & Graversen 2009), while ground measurements and vertical profiles from radiosondes do not give enough information on the horizontal variability of the local wind field to determine its structure.

In 1998, the ARTIST project carried out a campaign to investigate SODAR profiles combined with the ground-based in situ measurements at Ny-Ålesund and the mountain Zeppelinfjellet (474 m a.s.l.,

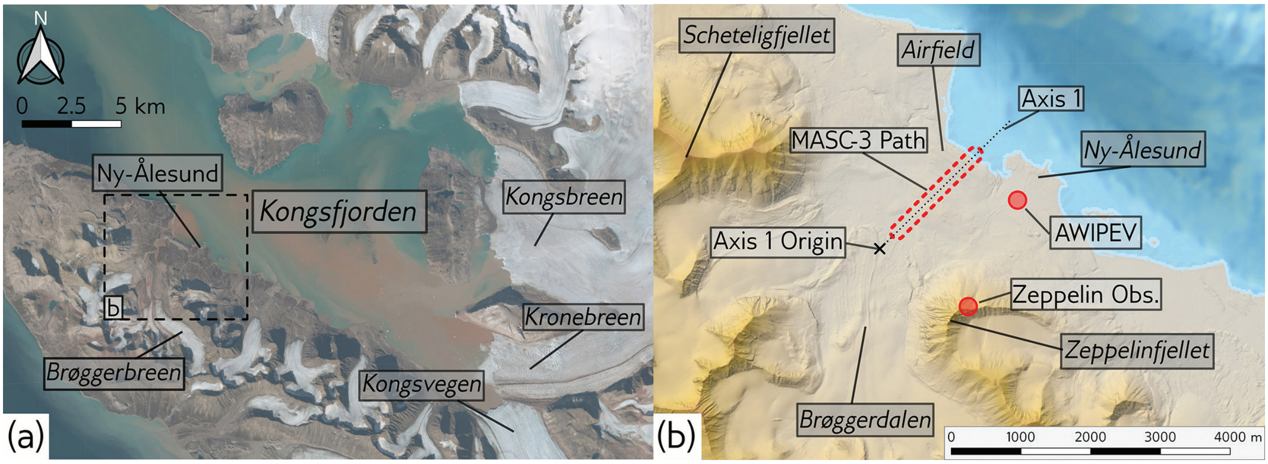

Fig. 2 (a) Overview map of the fjord Kongsfjorden. The glaciers Kongsbreen, Kronebreen and Kongsvegen are in the east and south-east. The sea is to the west. The smaller Brøggerbreen glacier originates south-west of Ny-Ålesund. The rectangle in (a) shows the extent of the zoomed-in map (b). (b) Detailed map of the area around Ny-Ålesund. West of Ny-Ålesund is the Brøggerdalen valley, with the Brøggerbreen glacier further up the valley, visible in (a). The highest mountains in the vicinity are Scheteligfjellet (719 m a.s.l.) and Zeppelinfjellet (556 m a.s.l.). The Zeppelin Observatory is located on Zeppelinfjellet, at 474 m a.s.l. Within the village of Ny-Ålesund is AWIPEV, which is the location of the continuous ground measurements and the radiosonde ascents presented in Fig. 4. The flight pattern of MASC-3 (red dashed line) followed along axis 1 (black dashed line), reaching into the Brøggerdalen in the south-west and passing over the Ny-Ålesund Airfield in the north-east. (Maps by Topo Svalbard, https://toposvalbard.npolar.no/, Norwegian Polar Institute/USGS Landsat.)

approximately 2 km south-west of Ny-Ålesund; Fig. 2). The results show that the two prevailing wind directions in the ABL are oriented along the fjord: In spring, the air flows from the Kongsbreen and Kongsvegen glaciers in the south-east to the mouth of the fjord in the north-west (Hartmann et al. 1999; Argentini et al. 2003). During summer, the primary wind direction reverses (Beine et al. 2001). This seasonal pattern of down-fjord flows in winter and up-fjord flows in summer is typical for large fjords (Svendsen et al. 2002). In Ny-Ålesund, this flow along the fjord with an east–south-east or south-east wind direction is dominant during spring. Local katabatic flows from the Zeppelinfjellet slope cause a secondary, less frequent, south–south-west to south-west wind direction and may also cause differences in wind direction between AWIPEV and Zeppelinfjellet (Beine et al. 2001).

To validate these findings and to investigate the horizontal variability of the wind field around Ny-Ålesund, the UAS MASC-3 is used in conjunction with ground-based measurements and radiosondes. During a measurement flight, MASC-3 can close the gap between separate ground measurement locations while also creating a vertical profile of the ABL, essentially creating a two-dimensional snapshot of the ABL conditions during a measurement flight. An in situ measurement system like MASC-3 can collect data even under conditions difficult for remote sensing systems (e.g., low aerosol concentrations).

During April and May 2018, the MASC-3 research UAS operated by the University of Tübingen performed in situ measurements west of Ny-Ålesund. The measurements took place along Brøggerdalen, a valley about 2 km wide, west of Ny-Ålesund. The glacier Brøggerbreen lies in the south-western part of the valley (Fig. 2). We compare 10 measurement flights presented here with simultaneous wind measurements on the ground. Two flights from 1 May 2018 are described as case studies, identifying a local, small-scale katabatic flow as an important factor in the local wind field. In the end, we present a high-resolution map of the local wind field around Ny-Ålesund.

Methods

Site description

The ground measurements of wind and temperature in this study come from two sources: the Norwegian observatory on the mountain Zeppelinfjellet, south-west of Ny-Ålesund, and, in Ny-Ålesund, the observatory of the French–German research base AWIPEV (Fig. 2). Ny-Ålesund is situated in Kongsfjorden, which is up to 11 km wide and 30 km long. The fjord opens up to the sea in the north-west. In the south-east, the glaciers Kongsbreen and Kongsvegen join the fjord. Steep mountains reaching up to 700 m in height surround the fjord. Ny-Ålesund itself is located on the south-west coast of the fjord. South of the village, Zeppelinfjellet rises to a height

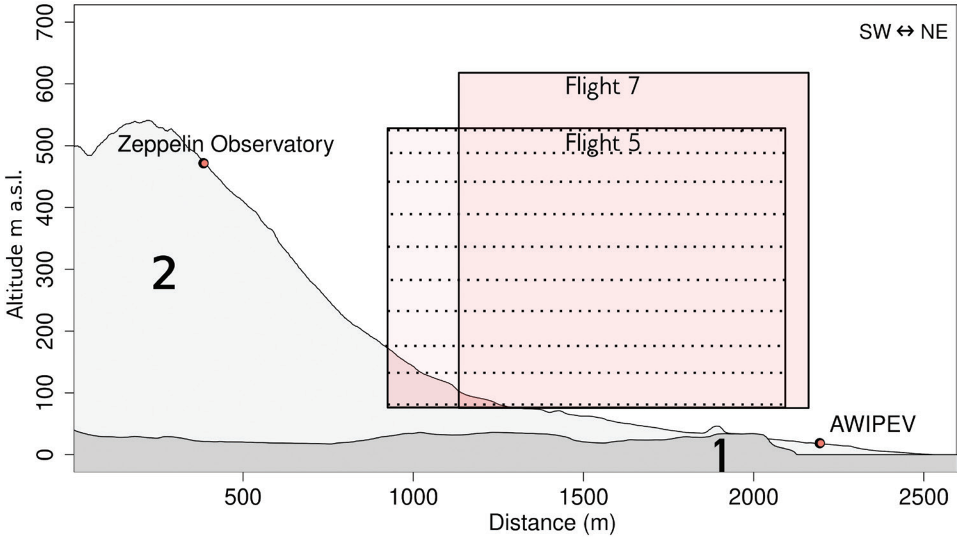

Fig. 3 Cross-section showing the terrain along the Brøggerdalen beneath the MASC-3 flight path (Fig. 2) and Zeppelinfjellet (light grey), the location of AWIPEV and Zeppelin Observatory and the vertical and horizontal extent of the two MASC-3 flights on 1 May 2018 (red squares). To illustrate the measurement pattern, the flight path of MASC-3 during flight 5 is included as a dashed line. The vertical axis shows the altitude in m a.s.l. The horizontal axis is the distance in m along the flight path originating at a reference point (marked in Fig. 2). Elevation data for cross-section from Arctic DEM (Porter 2018).

of 557 m a.s.l. The Zeppelin Observatory is situated below the summit, on the north-western edge of a ridge, at 474 m a.s.l. The airfield of Ny-Ålesund is north-west of the village, where Brøggerdalen opens up into the fjord. The cross-section in Fig. 3 shows the horizontal and vertical extent of the two case studies presented here. During the measurement period, the fjord was ice-free. The ground around Ny-Ålesund was completely covered with snow until mid-May.

MASC-3 sensor system

The UAS MASC-3 is an electrically powered aircraft with a wingspan of 4 m and a take-off weight between 5 and 8 kg, depending on battery weight. A Pixhawk 2.1 Cube Autopilot running the Arduplane firmware controls automatic flight and enables MASC-3 to follow a predefined set of waypoints during a measurement flight (Rautenberg et al. 2019). The measurement flights presented in this work lasted between 1 and 1.5 hours at a constant true airspeed of 18.5 m s^{-1}. All flights were conducted within the line of sight around the Ny-Ålesund airfield. MASC-3 carries a meteorological sensor package developed by the Environmental Physics Group of the University of Tübingen. The set-up is based on the Meteorological Mini-Aerial Vehicle 2 and MASC-2 aircraft (van den Kroonenberg et al. 2008; Wildmann, Hofsäß et al. 2014). For wind, temperature and position measurements, MASC-3 uses a five-hole probe, a fine wire platinum resistance thermometer (Wildmann et al. 2013) and an IMU with a GPS receiver. In order to measure the three-dimensional wind vector and air temperature with a resolution of up to 30 Hz, MASC-3 samples data with a frequency of 100 Hz (Wildmann, Ravi et al. 2014). Rautenberg et al. (2019) provide a detailed description of the complete MASC-3 set-up. MASC-3 can fly in wind speeds up to 15 m s^{-1}; to ensure safe take-off and landing the maximum surface wind speed should not exceed 10 m s^{-1}. In the configuration flown in Ny-Ålesund, MASC-3 can only be used in line of sight, excluding flying in fog or clouds. MASC-3 cannot be flown in heavy rain.

Measurement flights

A total of 18 measurement flights were performed between 24 April and 25 May 2018 (data set: Schön et al. 2022). The first 10 flights between 24 April and 12 May 2018, which are presented here, follow the flight pattern depicted in Figs. 2b and 3. The date, time frame, minimum measurement altitude (h_{min} [m a.s.l.]) and maximum measurement altitude (h_{max} [m a.s.l.]) of each flight are listed in Table 1. The flights are referred to hereafter by their flight number. The minimum and maximum flight altitudes for each flight vary with weather conditions, visibility and coordination with Air Traffic.

During a measurement flight, MASC-3 starts at the lowest measuring altitude, repeating each measurement altitude in the pattern shown in Fig. 3 two times, maintaining a straight and level flight path and a constant true

Table 1 Overview of the Multiple Purpose Airborne Sensor Carrier (MASC) measurement flights performed between 24 April and 12 May 2018. The two case studies on 1 May are highlighted in boldface.

Flight no.	Date	Time (UTC)[a]	h^{b}_{min} (m a.s.l)	h^{c}_{max} (m a.s.l)	Altitudes of the measurement legs (m a.s.l.)[d]
1	2018-04-24	19:59–20:54	77	327	80, 100, 130, 150, 180, 200, 230, 280, 320
2	2018-04-26	12:51–13:58	73	466	70, 90, 110, 130, 160, 180, 220, 270, 320, 370, 410, 460
3	2018-04-29	19:28–20:51	72	331	70, 90, 110, 140, 160, 180, 210, 230, 280, 330
4	2018-04-29	21:51–23:12	75	326	80, 90, 110, 140, 160, 180, 180, 210, 230, 280, 330
5	**2018-05-01**	**09:31–10:39**	**77**	**528**	**80, 90, 140, 190, 240, 280, 330, 380, 430, 480, 530**
6	2018-05-01	11:47–13:08	64	519	60, 80, 130, 180, 230, 270, 320, 370, 420, 470, 520
7	**2018-05-01**	**15:30–16:55**	**66**	**619**	**70, 80, 130, 180, 230, 330, 420, 520, 620**
8	2018-05-07	11:10–11:56	84	422	80, 110, 130, 160, 180, 230, 330, 420
9	2018-05-12	14:38–15:59	64	410	70, 130, 180, 220, 270, 320, 360, 410
10	2018-05-12	17:25–18:46	75	540	80, 90, 140, 240, 340, 440, 540, 640

[a]The timeframe of the measurement. [b]The lowest measurement altitude. [c]The maximum measurement altitude. [d]Rounded to the nearest 10 m.

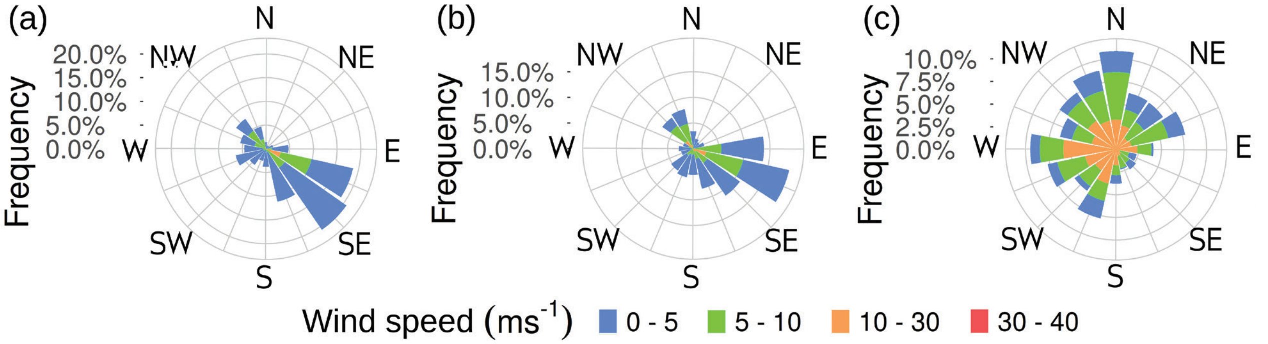

Fig. 4 Wind roses for April and May of 2017 to 2020: (a) ground data from the AWIPEV observatory (Maturilli 2020a, b); (b) radiosonde data (Maturilli 2020c) from 400 to 500 m a.s.l., corresponding to the altitudes around Zeppelin Observatory (450 m a.s.l.); and (c) 2000–2100 m a.s.l., above the highest terrain in Svalbard. Radiosonde data are from the daily launches at AWIPEV (11:00 UTC), at 1 Hz resolution. Ground station data are from a cup anemometer/wind vane combination at AWIPEV (10 m above ground, 21 m a.s.l.), provided as 1-min average. The dominant wind direction in the AWIPEV measurements at sea level is east–south-east to south-east, which corresponds to a flow along the fjord.

airspeed of 18.5 m s^{-1}. Accordingly, each of these repetitions consists of two straight and level sections, referred to as legs. The respective altitudes of the measurement legs for each flight are listed in Table 1. The vertical distance between measurement legs is typically 20–30 m below 200 m a.s.l. and 40–50 m above. This increases the vertical resolution close to the ground, where a high vertical variability in wind and temperature is expected.

After completing all repetitions at one altitude, MASC-3 proceeds to the next altitude. This is repeated up to the maximum measurement altitude. Whenever possible, the maximum altitude was higher than the Zeppelin Observatory (474 m a.s.l.) to fully cover the vertical variability of the wind field between the surface and the observatory.

In Fig. 2b, the flight pattern is shown as a dashed red line on a map of the area around Ny-Ålesund. Figure 3 shows the same flight pattern as a cross-section, exemplified for the extents of flights 5 and 7. In the cross-section of flight 5, dashed lines indicate the path of the measurement legs.

Ground-based, NWP and radiosonde data

Ground-based measurements, radiosonde data and NWP model data are compared with MASC-3 data. Observations are obtained from AWIPEV ground-based and radiosonde measurements for April and May from 2017 to 2020 (Maturilli 2020a, b, c). At the AWIPEV observatory, wind measurements are taken at 10 m above the surface level (22 m a.s.l.) using a cup anemometer and wind vane combination, provided as 1-min averages. The radiosonde data used in Fig. 4 are from the daily radiosonde launches (Vaisala RS41) in Ny-Ålesund. The radiosonde is launched every day at 11:00 UTC. The position of the radiosonde is determined by GPS data, which is used to calculate wind speed and wind direction.

Data from the Zeppelin Observatory are provided by NILU, measured at 474 m a.s.l. (Aas 2007a, b). At this observatory, a cup anemometer is used for wind speed, a wind vane for wind direction and a platinum resistance thermometer for temperature measurements, provided as 1-hour average. For the case studies, synoptic conditions during the flights in Table 1 were analysed based on operational AROME Arctic NWP model cycle, version 40h1.1, with output provided by the Norwegian Meteorological Institute (MET Norway 2021). The model system provides regional short-range forecasts for the European Arctic with 2.5 km horizontal resolution and 65 vertical levels (Müller et al. 2017; Køltzow et al. 2019). The results presented in this study are based on forecasts initiated at 00:00 UTC on each flight day.

Data processing

MASC-3 produces a high-resolution time series of the wind vector and temperature for each measurement leg. This results in multiple time series per measured altitude. The resolution of those measurements is sufficient to resolve smaller turbulent eddies even in the submetre range (Rautenberg et al. 2019). However, to determine the wind field, it is not individual eddies that have to be considered, but the average wind direction, wind speed and temperature. Therefore, a time average must be taken that is long enough to encompass the largest relevant eddies. To accomplish this, the averaging time must be larger than the integral time scale of each component of the three-dimensional wind vector (Garratt 1992). For the case studies presented here, the integral time scales of u, v and w were calculated for each leg and, in all cases, were found to be less than 9 s. A moving average of 9 s was, therefore, applied for the cross-section plots (Fig. 5). For the vertical profiles (Fig. 6), all measurement legs at each measurement altitude were averaged.

MASC-3 data for the case studies are visualized with two different methods. Two-dimensional cross-sections are used to visualize the vertical and horizontal variability of the wind field and temperature (Fig. 5). The position of the cross-section and the horizontal and vertical extent of the measurement flights are illustrated in Figs. 2b and 3. The second plotting method for the two case studies is vertical profiles (Fig. 6). They are used to compare MASC-3 data with the ground measurements at AWIPEV and the Zeppelin Observatory to investigate the relationship between the wind conditions at AWIPEV and the Observatory. Each point in the vertical profile represents the average of all measurement legs at the respective altitude. At the corresponding altitude, measurement data from AWIPEV and the Zeppelin Observatory for the measurement flight duration are included in the profiles. A MASC-3 temperature measurement from the ground is included to provide a complete vertical profile of temperature.

Results

Long-term observations of the wind field

The wind roses of the long-term wind conditions for April and May between 2017 and 2020 show that the dominant wind direction at ground level in Ny-Ålesund was east–south-east or south-east, i.e., along the shoreline of Kongsfjorden (Fig. 4a). This wind direction corresponds to the flow along the fjord described in literature (Beine et al. 2001; Svendsen et al. 2002; Argentini et al. 2003; Esau & Repina 2012). Two secondary wind directions are visible: west–north-west, corresponding to an up-fjord flow, which is more prevalent during summer (Svendsen et al. 2002), and a west–south-west to south-west wind direction. Between 400 and 500 m a.s.l. (corresponding to the altitude of the Zeppelin Observatory at 474 m a.s.l.), the radiosonde data show a dominant east–south-east to south-east wind direction (Fig. 4b), which corresponds to the ground measurement. The second most common wind directions were the north–north-west and north-west, with additional peaks in the wind rose at the south–south-west and south–south-east. At 2000–2100 m a.s.l., above the highest mountains of Svalbard (1713 m a.s.l.), the wind rose of the radiosonde measurements (Fig. 4a) shows a dominant north wind direction, together with a broader range of wind directions from the south–south-west to north–north-west.

MASC-3 measurement flights 24 April—12 May 2018

Ten measurement flights were performed between 24 April and 12 May 2018, using the flight pattern shown in Fig. 2b. To provide an overview of the measurement data, Table 2 shows the mean wind direction and horizontal wind speed during the measurement flights at AWIPEV and the Zeppelin Observatory. For MASC-3 flight data, this information is displayed for the lowest altitude $h_{\min}$ and highest altitude $h_{\max}$ (see Table 1 for the altitudes). The dominant south-east to east–south-east flow along the fjord seen in the wind roses (Fig. 4) was measured at AWIPEV during flights 3–8, when the prevailing wind direction at the Zeppelin Observatory was south. The

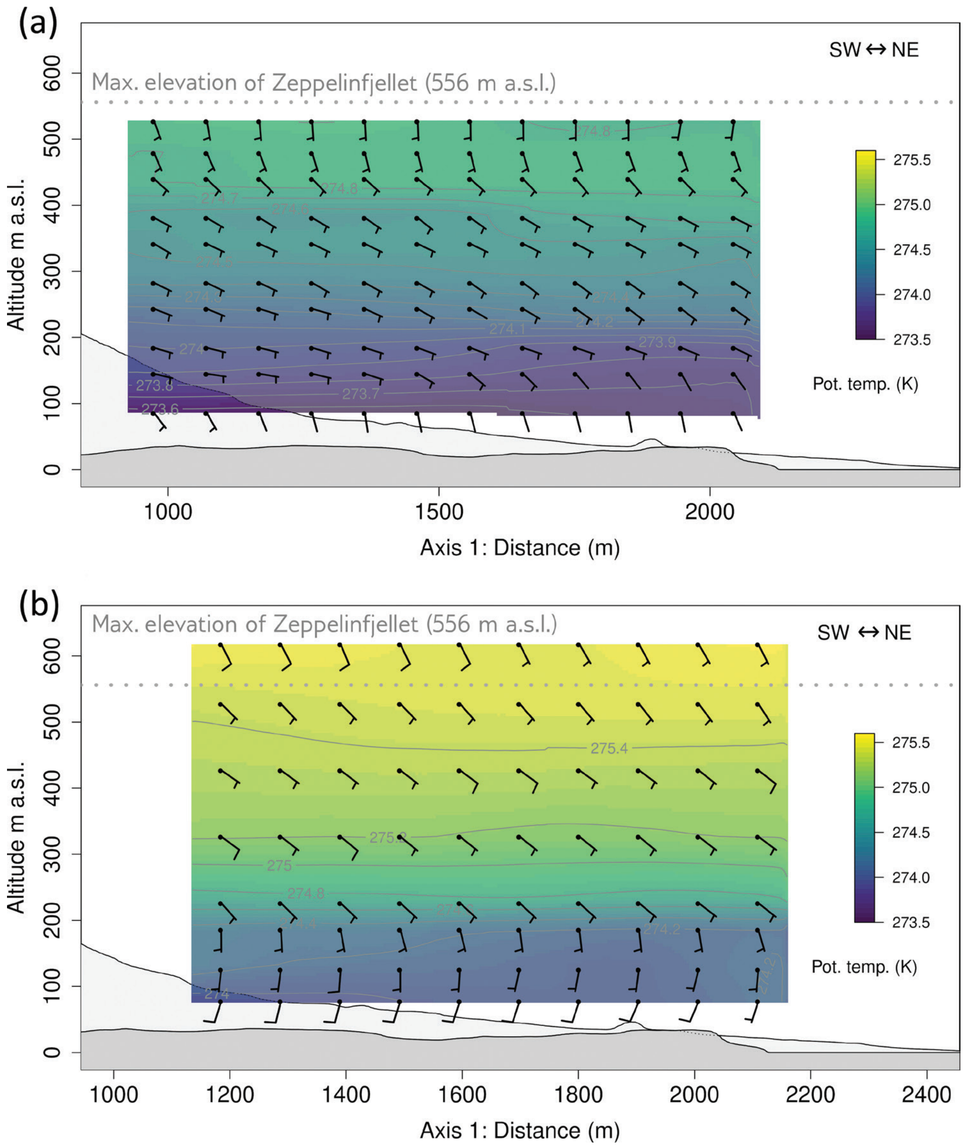

Fig. 5 Cross-sections of MASC-3 measurements: (a) flight 5 on 1 May 2018, 09:31–10:39 UTC and (b) flight 7 from 15:30 to 16:55 UTC. In the cross-sections, black wind barbs show the horizontal wind speed and wind direction measured by MASC-3 for every measurement altitude. Dashes at the end of the barb represent horizontal wind speed. Barbs without bars represent wind speed between 0 and 2 knots, a short bar 5 ± 2 knots and a long bar 10 ± 2 knots. Potential temperature is displayed along a colour ramp. The temperature values in the altitudes between measurements are linearly interpolated. The dark grey silhouette shows the terrain directly below the measurement (axis 1). The light grey silhouette shows the maximal terrain elevation in the vicinity of the measurement (axis 2). The vertical axis shows the altitude in m a.s.l. The horizontal axis is the distance in m along axis 1, originating at a reference point (marked in Fig. 2).

mean wind speed at AWIPEV ranges 0.7–2.9 m s^{-1}, while Zeppelin showed slightly higher wind speed, 1–3 m s^{-1}. Since this south-east to east–south-east wind direction was the main wind direction in the long-term observations at AWIPEV for April and May, the interpretation of the MASC-3 measurements will focus on flights 3–8.

Comparing the AWIPEV measurements with the MASC-3 measurements at the lowest measurement altitude shows that, in most cases, MASC-3 measured similar wind speeds as the AWIPEV observatory (in the range of ±1 m s^{-1}). For flights 7 and 10, MASC-3 measured a higher wind speed than at the AWIPEV. Generally, the wind speed during all 10 flights was low, between 0.5 and 4.5 m s^{-1}.

The dominant wind direction at AWIPEV was south to east–south-east (flights 1–7). The corresponding wind

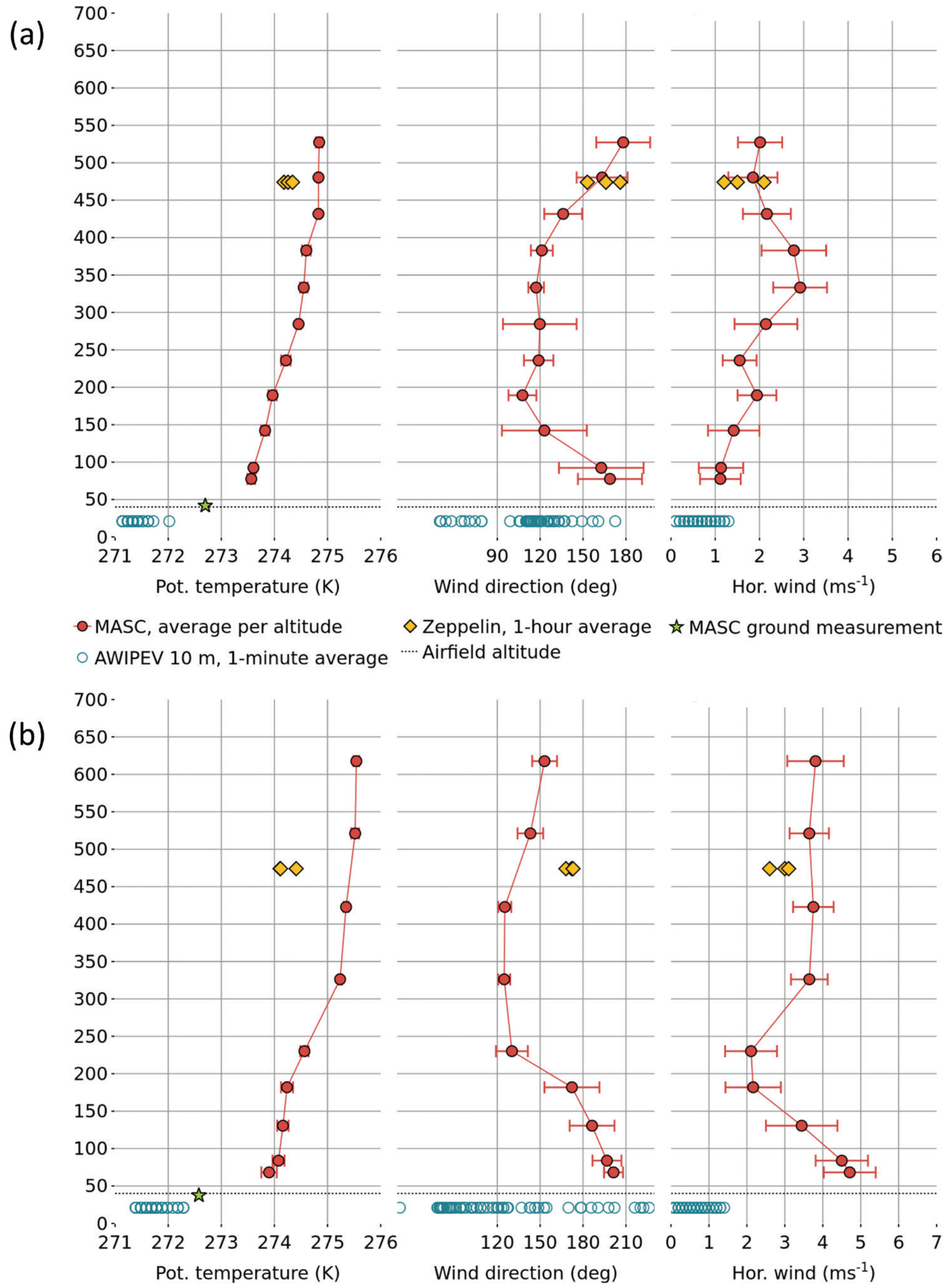

Fig. 6 Vertical profiles of potential temperature, wind direction and horizontal wind speed for MASC-3 measurements and ground-based measurements at AWIPEV and the Zeppelin Observatory: (a) flight 5, 1 May 2018 09:31–10:39 UTC and (b) flight 7, 15:30–16:55 UTC. For MASC-3, the horizontal bars show the standard deviation within measurement altitude. AWIPEV data are provided as 1-min average, and Zeppelin data as 1-hour average.

direction at MASC-3 was either south-east (flights 3, 4 and 6) or more south to west than at AWIPEV (flights 1, 2, 5 and 7). The last three flights (flights 8, 9 and 10) were exceptions to this pattern, and for flights 9 and 10, different wind conditions prevailed at AWIPEV, with west–north-west and south-west wind, respectively. A recurring pattern in the vertical profiles measured by MASC-3 near Ny-Ålesund was a backing (counterclockwise rotation with increasing altitude) of the wind direction from the lowest altitude up to 120 m – 230 m a.s.l. For example, during flight 5, the wind direction rotated from the south at 77 m a.s.l. to an east–south-east wind direction at 180 m a.s.l. by 80°. Since this backing is a typical feature of the wind profiles measured with

MASC-3, it is categorized using the two values in the wind direction profile column of Table 2, b_{top} and $b°$.

Case study selection: 1 May 2018

For a detailed look at the wind field characteristics from flight data, two measurement flights are selected as case studies. Flight 5, which took place on 1 May 2018 between 09:31 and 10:39 UTC, at altitudes ranging 77–528 m a.s.l., showed the backing of the wind direction described above, as well as the typical south-west wind direction at AWIPEV. Furthermore, data are available for this flight up to 528 m altitude, i.e., the vertical profile of the wind was measured up to the altitude of the Zeppelin Observatory. The vertical profile of flight 5 is typical for the available vertical profiles. It also contains data above 474 m a.s.l., so a comparison with the Zeppelin Observatory is possible. The second case study, flight 7, also took place on 1 May 2018, 15:30 to 16:55 UTC, at altitudes between 66 and 619 m a.s.l. This flight also showed the backing in the wind direction. In addition, in this flight, the wind speed shows a strong local maximum at the lowest flight altitude, along with a south–south-west wind direction (Figs. 5, 6, and Table 2). This local maximum in wind speed at the lower flight altitudes was not a common feature and was only measured in flights 2, 7 and 8. In the profile cross-section (Fig. 2b), the case studies' extent on 1 May is shown.

To put the case studies into context, long-term observations from radiosondes and ground stations are used to describe the typical wind speed and wind directions for April and May in Ny-Ålesund. Then, the synoptic situation for 1 May 2018 is described. Finally, the case studies are described in detail, with cross-sections and vertical profiles, as explained in the data processing section. The wind field's vertical variation for both flights on 1 May 2018 is shown using vertical profiles for potential temperature, wind direction and horizontal wind speed (Fig. 6). The profiles show the averaged values and the standard deviation in the high-resolution data for each measurement altitude for each flight.

The potential temperature measured at 10 m above the ground at AWIPEV was 2–2.5 K lower than at the lowest MASC-3 altitude during both flights. A possible reason for this is a surface-based temperature inversion. This is supported by a MASC-3 measurement on the ground directly after landing (Fig. 6). On the ground, MASC-3 measured 272.7 K for flight 5 and 272.6 K for flight 7. For flight 5, the potential temperature profile above the surface-based inversion measured with MASC-3 showed a weakly stable ABL from 273.6 K at 80 m to 274.9 K at 430 m a.s.l. and a neutral stratification between 430 m and 520 m a.s.l. For flight 7, there was still a weakly stable stratification at altitudes below 530 m a.s.l., but between 230 m and 320 m a.s.l., there was an inversion in the temperature profile, where the potential temperature increased by 0.8 K within a vertical distance of 90 m.

For flight 5, the wind direction at the lowest MASC-3 altitude was south. Above this altitude, there was backing in the wind direction to the east–south-east at 200 m a.s.l. This wind direction of east–south-east (to south-east), along Kongsfjorden, was also dominant in the long-term measurements in Ny-Ålesund (Fig. 4). Above 200 m a.s.l., the wind direction rotated from the east–south-east to the south, at 530 m a.s.l. The wind speed increased with altitude, from 1 m s^{-1} at the lowest measurement altitude to a maximum wind speed of 2.9 m s^{-1} at 380 m a.s.l. While the measured horizontal wind speed and wind direction at Zeppelin lay largely within the standard deviation of the MASC-3 values for the same altitude, AWIPEV data showed a low wind speed below 1 m s^{-1}. The morning wind direction measurement at AWIPEV had a very high standard deviation due to the low wind speed.

For flight 7, from the lowest MASC-3 altitude of 60–230 m a.s.l., there was backing in the wind direction from the south–south-west to the south-east. Between 230 and 420 m a.s.l., the wind direction was the south-east. Above 420–620 m a.s.l., the wind direction rotated from the south-east to the south–south-east. The maximum wind speed was 4–5 m s^{-1} at 60 m a.s.l., decreasing with altitude to 2 m s^{-1} at 180 m a.s.l. and then increasing again to 3–4 m s^{-1} above 300 m a.s.l. Horizontally, the wind speed and wind direction above 230 m a.s.l. were homogeneous, with similar values over the valley and the shore (Fig. 5).

Synoptic conditions on 1 May 2018

Towards the end of April 2018, a large low-pressure system deepened east of Greenland. On its eastern side, a ridge of high pressure stretched from the northern coast of Scandinavia to the western coast of Svalbard. According to the AROME Arctic NWP model output, the central line of the ridge was located roughly along the western coast of Spitsbergen at 00:00 UTC on 1 May and moved gradually inland during the day (Fig. 7). The low wind speed at the 925 hPa level and above with a west–south-west direction in the morning of May changed to a south–south-west direction with increasing wind speed towards the evening. AROME Arctic forecasts showed a warm-air advection by about 1.5 degrees in the 6 hours between 10:00 and 16:00 UTC (i.e., between the flights) at heights between 200 m and 1000 m a.s.l. (Fig. 8). This led to an increased thermal stratification near the surface.

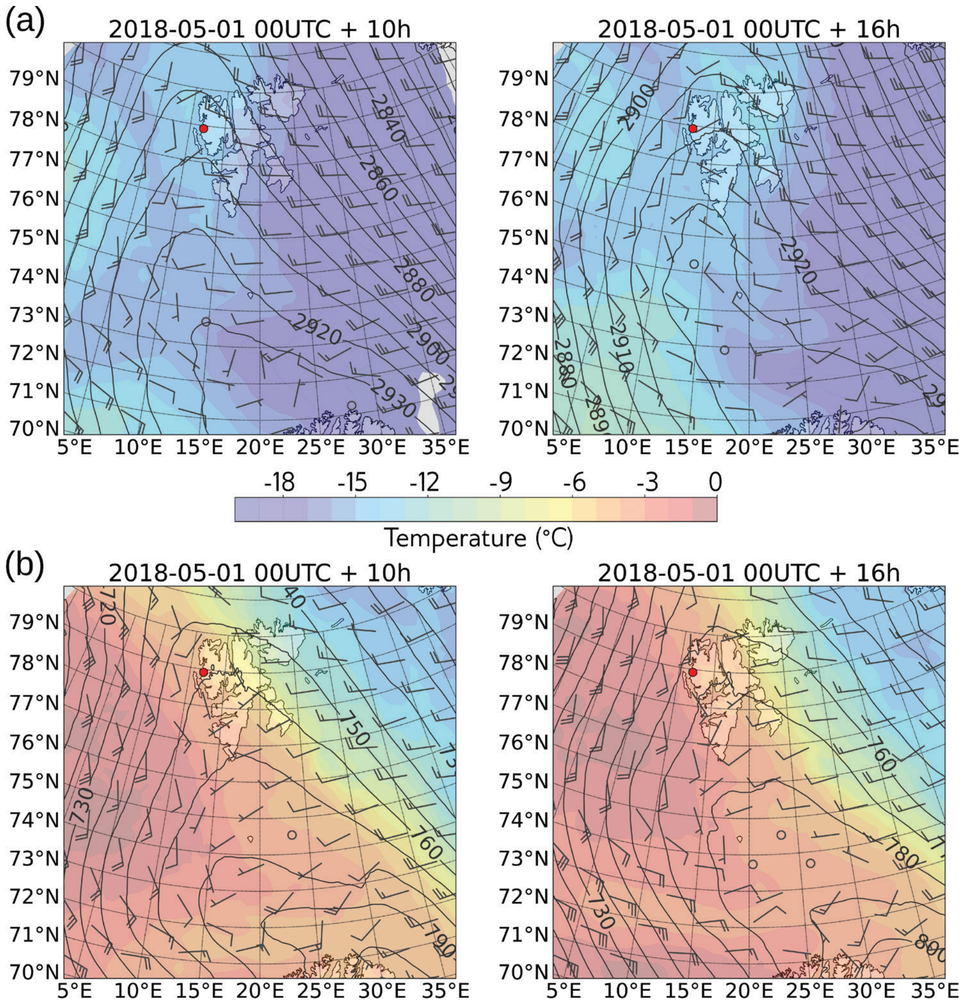

Fig. 7 Synoptic situation on 1 May 2018 based on operational forecasts of the AROME Arctic model (MET Norway 2021), (a) for the 700 hPa level and (b) for the 925 hPa level. Geopotential height (grey contours), temperature (colour contours) and wind barbs are shown. The output is shown for 10:00 UTC (left) and 16:00 UTC (right) on 1 May. The location of Ny-Ålesund is shown as a red dot.

Discussion

The measurements with MASC-3 are snapshots of the ABL, so it is useful to compare and contextualize them with long-term measurements. Cisek et al. (2017) analysed the multiannual monthly mean of wind speed from 2005 to 2016 in Ny-Ålesund, based on measurements by the AWIPEV station. For this timeframe, the maximum mean wind speed was between 5 and 6 m s^{-1} during November and December, with the minimum mean wind speed in August, at 2–3 m s^{-1}. The most common wind conditions at AWIPEV in April and May were east–south-east to south-east wind direction with low (less than 5 m s^{-1}) wind speeds, which is also supported by more recent AWIPEV data and radiosonde data (Fig. 4). Therefore, the measurements of MASC-3 (Table 2) were carried out under wind conditions typical for spring in Ny-Ålesund.

The typical wind direction measured at AWIPEV is east–south-east–south-east, which corresponds to the flow along the fjord. The wind direction measured by MASC-3 at lower altitudes, 80–200 m a.s.l., in Brøggerdalen, differs significantly from this flow along the fjord in both case studies on 1 May 2018 (Fig. 6). Only at higher altitudes, between 200 and 500 m a.s.l., MASC-3 did also measure this east–south-east–south-eastwind direction. MASC-3, therefore, showed a backing from the south–south-west at the lowest flight altitude to south-east at around 200 m a.s.l. In most of the MASC-3 flights (Table 2), this backing is exemplified by flight 5 (Fig. 6a), with a continuous, stable temperature profile and with a wind speed profile, in which the wind speed increased with altitude and had a maximum above 300 m a.s.l.

Flight 7 showed, in addition to the backing in the lower altitudes, other noteworthy features. The

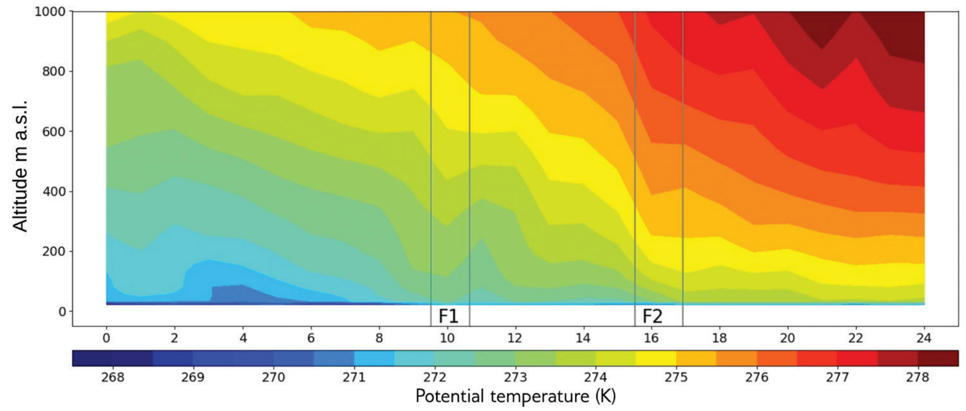

Fig. 8 Time-height cross-sections of potential temperature (Θ) at the grid point closest to Ny-Ålesund based on operational forecasts of AROME Arctic model starting from 00:00 UTC on 1 May 2018. F 5 and F 7 indicate the case study flight times by vertical lines showing the beginning and the end of each flight. Data are from the Norwegian Meteorological Institute (MET Norway 2021).

Table 2 Key measurement results for all flights listed in Table 1. For the period of the flights, the horizontal wind speed in m s^{-1} (v_h) and the wind direction (wd) in degrees are listed from the following sources: AWIPEV ground measurement at 10 m above ground, averaged MASC measurement values at lowest flight altitude (h_{min}, m a.s.l.), the mountain Zeppelinfjellet at 474 m a.s.l. and averaged MASC measurement values at maximum flight altitude (h_{max}, m a.s.l.). AROME Arctic (MET Norway 2021) wind speed (v_h) in m s^{-1} and wind direction (wd) for the 700 hPa and the 925 hPa pressure level provide information on the synoptic situation. AWIPEV data are averaged for the time interval of the measurement flight, and AROME and Zeppelin Observatory data are averaged for the time interval of the measurement flight rounded to the closest full hour. In addition, the structure of the backing of the wind direction with increasing altitude (backing, in degrees) is shown. For most of the measurement flights, there is a backing of the wind direction from the lowest altitude up to b_{top}, above that there is a veering of the wind direction. The amount of rotation of the wind direction between h_{min} and h_{max} is given in degrees with the value $b°$. The two case studies on 1 May are highlighted in boldface. See the results section for MASC-3 measurement flights from 24 April 2018 to 12 May 2018 for further explanation.

Flight no.	AWIPEV		MASC h_{min}		Zeppelin		MASC h_{max}		AROME 925 hPa		AROME 700 hPa		Backing	
	v_h	wd	v_h	wd	v_h	wd	v_h	wd	v_h	wd	v_h	wd	b_{top}	$b°$
1	1.7	SSE	1.6	SSW	1.5	SSE	3.9	SE	1.2	ENE	6.0	NNW	180	100
2	1.5	S	0.9	SSW	1	SW	1.8	NNE	2.1	W	6.5	NW	230	100
3	2.9	SE	1.9	SE	2.8	S	3	WSW	5.4	ESE	5.4	WSW	120	50
4	2	SE	3.1	SE	2.2	S	2	W	4.7	SSW	5.7	WSW	140	45
5	**0.7**	**SE**	**1**	**S**	**1.8**	**S**	**2**	**WSW**	**3.7**	**S**	**2.4**	**SW**	**180**	**80**
6	0.9	SE	1.7	SE	2.4	SSE	4	SW	5.0	SE	3.5	SSW		
7	**0.5**	**ESE**	**4.4**	**SSW**	**2.9**	**S**	**4**	**SW**	**6.3**	**SSE**	**6.4**	**SSW**	**200**	**80**
8	2.6	SE	3.5	ESE	3	S	4.5	WSW	8.8	S	9.7	SSW		
9	1.9	WNW	2.4	W	1.3	SE	2	WNW	7.8	WNW	11.3	NW	200	30
10	2	SW	3.8	SW	1.8	SSW	1.8	WNW	4.4	W	14.8	WNW		

maximum wind speed was at the lowest measurement altitude, with a decrease in wind speed up to 200 m a.s.l. (Fig. 6b). Also, the potential temperature profile was not as continuous as in flight 5: in flight 7, there was a sudden change in the temperature profile between 250 m and 300 m a.s.l. The change in the temperature profile and the higher wind speed coincided with the backing of the wind direction. These features are not visible in the AWIPEV data for the same timeframe, which shows very low wind speed below 1 m s^{-1} and the typical east–south-east to south-east wind direction.

The wind direction and wind speed deviation from the flow along the fjord were restricted to the lower, cold air layer in Brøggerdalen. This layer was continuous over the entire horizontal extent of the measurement flight, and its upper limit at approximately 200 m a.s.l. was related to the rotation of the wind direction from the south–south-west to the south-east (Fig. 5b). This cold air mass is, therefore, interpreted as katabatic flow, which moves near the ground towards the fjord, causing the south–south-west wind direction in the measurement area of MASC-3, but does not influence the measurement at AWIPEV, which lies outside of the axis of Brøggerdalen (Fig. 9). The development of the katabatic flow is facilitated by the development of a more stable ABL during the day, which is visible in the AROME Arctic model (Fig. 8). Generally, a more pronounced stable boundary layer may lead to a stronger local katabatic flow from Brøggerdalen. The formation of a katabatic flow in an Arctic fjord is described by Vihma et al. (2011). In both frozen and unfrozen fjords, katabatic flows can occur, carrying cold air down from the glaciers at the edge of the fjord. In the cases measured by MASC-3, the fjord was not frozen; therefore, the air moving along the Brøggerdalen was colder and denser than the air in the fjord and stayed close to the ground. Out of the MASC-3 measurements, flight 7 shows this local katabatic flow most clearly. The backing in the wind direction at lower altitudes, which is a common feature in the vertical profiles measured by MASC-3 (Table 2), may have resulted from a less pronounced katabatic flow from Brøggerdalen mixing with the flow along the fjord in cases where the temperature difference between the air masses is not as pronounced. Only in cases like flight 7, in which there was a well-developed stable ABL and low synoptic wind speed, this local katabatic flow got strong enough to be visible in the vertical profile of the wind speed. The dominant east–south-east to south-east wind direction visible in the long-term measurements (Fig. 4a, c) resulted from a flow from the south-east (Fig. 9). In earlier studies, this flow was interpreted either as a katabatic flow (Beine et al. 2001; Argentini et al. 2003) or a channelled flow along the fjord (Esau & Repina 2012). In this regard, the MASC-3 measurements correspond well to the SODAR measurements from the ARTIST campaign (Beine et al. 2001). In the SODAR measurements, the east–south-east to south-east wind direction of the fjord flow is visible from the lowest measurement altitude up to 200–600 m a.s.l., depending on the measurement day (Beine et al. 2001). In the MASC-3 data, the fjord flow is visible at altitudes between 120 m and 500 m a.s.l., depending on the flight. For the two case studies presented here (flights 5 and 7), the fjord flow was measured between 200 m and 400 m a.s.l. over the entire horizontal extent of the flight (Fig. 5). However, the MASC-3 data do not provide any information on whether the flow along the fjord is a katabatic flow or a channelled flow. More large-scale measurements crossing the entire fjord would be necessary to investigate this.

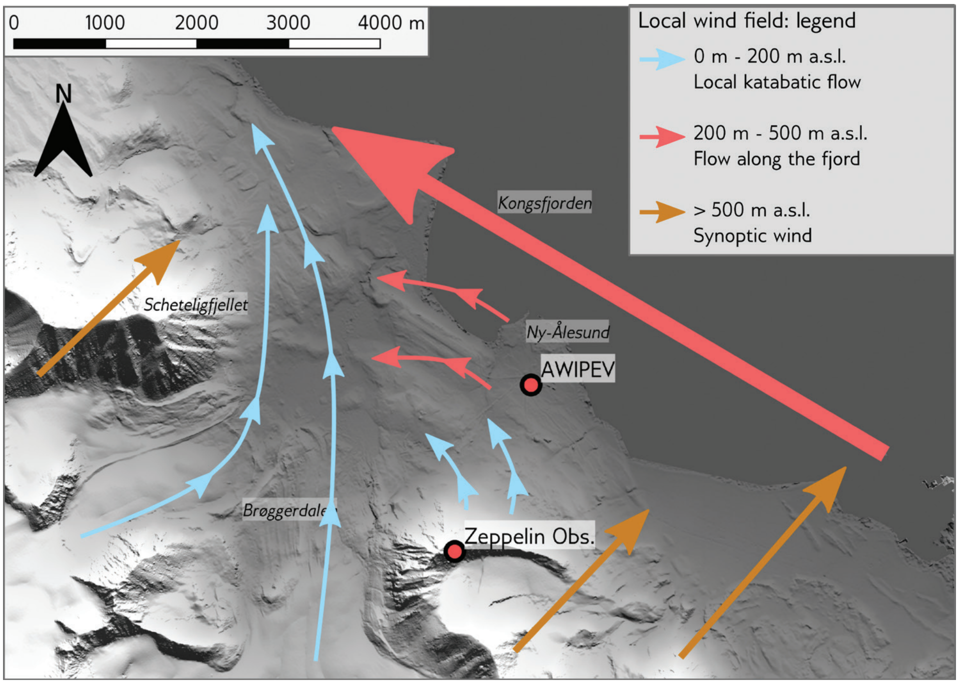

Fig. 9 Interpretation of the wind field around Ny-Ålesund, based on the measurements presented in this work. Light blue arrows show katabatic flow up to 100–200 m, and red arrows show the flow along the fjord. This flow reaches from sea level to an altitude of 500 m a.s.l. over the fjord. In Ny-Ålesund and over Brøggerdalen, it starts at 200 m a.s.l. and goes up to 500 m a.s.l. Yellow arrows show the wind above 500 m, which is already influenced by synoptic processes. The synoptic wind direction displayed represents the wind conditions on 1 May 2018 provided by AROME Arctic data (Fig. 7). Map created from Artic DEM elevation data (Porter 2018).

Above the fjord flow, the wind direction turns with increasing altitude in the direction of the synoptic wind. This rotation is also visible in the long-term ground measurements and the radiosonde data (Fig. 4). At AWIPEV, and in the radiosonde measurements between 400 and 500 m a.s.l., an east–south-east wind direction dominates, rotating with increasing altitude until it matches the synoptic wind between 2000 and 2100 m a.s.l. In the case of flights 5 and 7, this rotation manifested as a veering from the fjord flow to a southern wind direction between 400 m a.s.l. and the maximum flight altitude and a further veering between the maximum flight altitude and a south-west to west–south-west wind direction at the 700 hPa level, according to the AROME data (Table 2). A backing of the wind direction with altitude is also possible if the synoptic wind has a different direction. An example of this is the SODAR wind profiles of 5 April to 7 April 1998, shown by Beine et al. (2001). Here, the fjord flow is also visible in the lower altitudes, but there is a backing of the wind direction in the upper part of the wind profiles. This is because the synoptic wind had a northern direction during the SODAR measurements (Maturilli & Kayser 2016; radiosonde data for Ny-Ålesund, 5–7 April 1998). The measurement at Zeppelinfjellet follows this rotation of the wind direction. Depending on the maximum altitude and strength of the fjord flow, the wind direction on Zeppelinfjellet deviates from the wind direction in the fjord flow. In most cases measured with MASC-3, an east–south-east to south-east wind direction at AWIPEV corresponds to a south wind direction at Zeppelinfjellet. For flight 5, the wind direction on Zeppelinfjellet corresponded to the wind direction measured above Brøggerdalen by MASC-3 (Fig. 6). However, for flight 7 and most other flights, this correspondence was not present, so other factors differentiated the wind at Zeppelin Observatory from the wind measured over Brøggerdalen. The wind direction at the Zeppelin Observatory also differed from the 925 hPa level wind direction provided by AROME during all measurement flights (Table 2). Beine et al. (2001) suggest local drainage flows along the slope of Zeppelinfjellet, which would explain the south wind directions measured at the Zeppelin Observatory (Fig. 9).

Conclusion

The measurements with MASC-3 show the flow along the Kongsfjorden, which has already been described in literature, up to altitudes above 500 m a.s.l. in several measurements. It is also shown that a local katabatic flow along Brøggerdalen has an impact on the wind field around Ny-Ålesund. Since some measurement stations around Ny-Ålesund are located within Brøggerdalen (e.g., the Gruvebadet Observatory and measurements at the Ny-Ålesund airfield), this local katabatic flow has to be considered when comparing these measurements with measurements from Ny-Ålesund village or the Zeppelin Observatory. This is important because reliable long-term data from measuring stations are essential for climate analyses. In a more direct context, the measurements made with MASC-3 in spring 2018 can be seen as a snapshot of conditions in Ny-Ålesund at that time. As climate change progresses, wind conditions in Kongsfjorden are likely to change as well. This will need to be monitored in future measurements. The MASC-3 measurements show that the wind measurements at AWIPEV in Ny-Ålesund are representative of the flow along the fjord. However, the wind measurements at the Zeppelin Observatory do not correlate to the MASC-3 measurements, the AWIPEV measurements or the synoptic wind conditions provided by the AROME model. It also becomes evident that the wind speed and direction provided by the weather prediction model data are insufficient to make a statement about the wind conditions in Ny-Ålesund. Still, the thermal stratification shown in the models can help with the interpretation of the local wind field. The MASC-3 measurements presented in this work only covered a relatively small part of Kongsfjorden, both vertically and horizontally.

Measurements on a larger scale, going across the fjord and well above the ABL, could help improve our understanding of the interaction between the Kongsfjorden wind situation and the synoptic conditions. Further measurements in the Kongsfjorden, especially during stable ABL conditions, could also provide information on the development of low-level jets, both close to Ny-Ålesund along Brøggerdalen and along Kongsfjorden. As in this work, the interaction of time-limited UAS measurements covering a dedicated area and localized but time-unlimited ground measurements have the potential to provide an accurate, comprehensive picture of a local wind field, not only in Ny-Ålesund but also in other locations with small-scale and variable wind fields influenced by a complex topography.

Acknowledgements

The authors thank the following people for their support for this work: the pilots of MASC-3, Alexander Rautenberg and Markus Schygulla; colleagues in the Environmental Physics Workgroup of the University of Tübingen, Claudio Crazzolara, Patrick Manz, Hasan Mashni and Moritz Mauz, who operated MASC-3 or provided the logistics for the measurement campaign; the team around the UAS ALADINA from the Technische Universität Braunschweig and the TROPOS Institute Leipzig, Konrad Baerfuss, Lutz Bretschneider, Ralf Kaethner and Alexander Peuker, for all their help and support during the project; Carl Fortelius, for assisting with numerical weather prediction model analyses; Wenche Aas (NILU) and Marion Maturilli (Alfred Wegener Institute) for providing the ground and radiosonde measurements used in this work; and Andy Clifton for creating the script for the wind rose plots. Finally, the authors also thank the station leaders of AWIPEV, Piotr Kupiszewski and Rudolf Denkmann, for their support during the measurements.

Disclosure statement

The authors report no conflict of interest.

Funding

This research was funded by the German Research Foundation under the project number BA 1988/14-3.

References

Aas W. 2007a. Zeppelin Mountain meteorological measurement (wind speed). Data set. Norwegian Institute for Air Research. Accessed on the internet at https://ebas-data.nilu.no/DataSets.aspx?stations=NO0042G&nations=NO578NOR&components=wind_speed&matrices=met&fromDate=1970-01-01&toDate=2022-12-31 on 25 September 2019.

Aas W. 2007b. Zeppelin Mountain meteorological measurement (wind direction). Data set. Norwegian Institute for Air Research. Accessed on the internet at https://ebas-data.nilu.no/DataSets.aspx?stations=NO0042G&naNO578NOR&components=wind_speed&matrimet&fromDate=1970-01-01&toDate=2022-12-31 on 25 September 2019.

Altstädter B., Platis A., Wehner B., Scholtz A., Wildmann N., Hermann M., Käthner R., Baars H., Bange J. & Lampert A. 2015. ALADINA—an unmanned research aircraft for observing vertical and horizontal distributions of ultrafine particles within the atmospheric boundary layer. *Atmospheric Measurement Techniques 8*, 1627–1639, doi: 10.5194/amt-8-1627-2015.

Argentini S., Viola A.P., Mastrantonio G., Maurizi A., Georgiadis T. & Nardino M. 2003. Characteristics of the boundary layer at Ny-Ålesund in the Arctic during the ARTIST field experiment. *Annals of Geophysics 46*, 185–196, doi: 10.4401/ag-3414.

Beine H.J., Argentini S., Maurizi A., Viola A. & Mastrantonio G. 2001. The local wind field at Ny-Ålesund and the Zeppelin Mountain at Svalbard. *Meteorology and Atmospheric Physics 78*, 107–113, doi: 10.1007/s007030170009.

Cisek M., Makuch P. & Petelski T. 2017. Comparison of meteorological conditions in Svalbard fjords: Hornsund and Kongsfjorden. *Oceanologia 59*, 413–421, doi: 10.1016/j.oceano.2017.06.004.

Egerer U., Ehrlich A., Gottschalk M., Griesche H., Neggers R.A.J., Siebert H. & Wendisch M. 2021. Case study of a humidity layer above Arctic stratocumulus and potential turbulent coupling with the cloud top. *Atmospheric Chemistry and Physics 21*, 6347–6364, doi: 10.5194/acp-21-6347-2021.

Esau I. & Repina I. 2012. Wind climate in Kongsfjorden, Svalbard, and attribution of leading wind driving mechanisms through turbulence-resolving simulations. *Advances in Meteorology 2012*, article no. 568454, doi: 10.1155/2012/568454.

Ferrero L., Cappelletti D., Busetto M., Mazzola M., Lupi A., Lanconelli C., Becagli S., Traversi R., Caiazzo L., Giardi F., Moroni B., Crocchianti S., Fierz M., Močnik G., Sangiorgi G., Perrone M.G., Maturilli M., Vitale V., Udisti R. & Bolzacchini E. 2016. Vertical profiles of aerosol and black carbon in the Arctic: a seasonal phenomenology along two years (2011–2012) of field campaign. *Atmospheric Chemistry and Physics 16*, 12601–12629, doi: 10.5194/acp-16-12601-2016.

Garratt J.R. 1992. *The atmospheric boundary layer*. Cambridge: Cambridge University Press.

Hartmann J., Albers F. & Argentini S. 1999. *Arctic radiation and turbulence interaction study (ARTIST). Berichte zur Polarforschung (Reports on Polar Research) 305*. Bremerhaven: Alfred Wegener Institute for Polar and Marine Research.

Køltzow M., Casati B., Bazile E., Haiden T. & Valkonen T. 2019. An NWP model intercomparison of surface weather parameters in the European Arctic during the year of polar prediction special observing period Northern Hemisphere 1. *Weather and Forecasting 34*, 959–983, doi: 10.1175/WAF-D-19-0003.1.

Lampert A., Altstädter B., Bärfuss K., Bretschneider L., Sandgaard J., Michaelis J., Lobitz L., Asmussen M., Damm E., Käthner R., Krüger T., Lüpkes C., Nowak S., Peuker A., Rausch R., Reisder F., Scholtz A., Zakharov D.S., Gaus D., Bansmer S., Wehner B. & Pätzold F. 2020. Unmanned aerial systems for investigating the polar atmospheric boundary layer—technical challenges and examples of applications. *Atmosphere 11*, article no. 416, doi: 10.3390/atmos11040416.

Maturilli M. 2020a. Continuous meteorological observations at station Ny-Ålesund (2020-04). Data set. Alfred Wegener Institute, Research Unit Potsdam, PANGAEA®—Data Publisher for Earth & Environmental Science, doi: 10.1594/PANGAEA.925612.

Maturilli M. 2020b. Continuous meteorological observations at station Ny-Ålesund (2020-05). Data set. Alfred Wegener Institute, Research Unit Potsdam, PANGAEA®—Data Publisher for Earth & Environmental Science, doi: 10.1594/PANGAEA.925613.

Maturilli M. 2020c. High resolution radiosonde measurements from station Ny-Ålesund (2017-04 et seq). Data set. Alfred Wegener Institute, Research Unit Potsdam, PANGAEA®—Data Publisher for Earth & Environmental Science, doi: 10.1594/PANGAEA.914973.

Maturilli M. & Kayser M. 2016. Homogenized radiosonde record at station Ny-Ålesund, Spitsbergen, 1993–2014. Data set. Alfred Wegener Institute, Research Unit Potsdam, PANGAEA®—Data Publisher for Earth & Environmental Science, doi: 10.1594/PANGAEA.845373.

MET Norway 2021. MET AROME Arctic. Data set. Accessed on the internet https://thredds.met.no/thredds/metno.html on 6 August 2021.

Müller M., Batrak Y., Kristiansen J., Køltzow M.A., Noer G. & Korosov A. 2017. Characteristics of a convective-scale weather forecasting system for the European Arctic. *Monthly Weather Review 145*, 4771–4787, doi: 10.1175/MWR-D-17-0194.1.

Petäjä T., Duplissy E.-M., Tabakova K., Schmale J., Altstädter B., Ancellet G., Arshinov M., Balin Y., Baltensperger U., Bange J., Beamish A., Belan B., Berchet A., Bossi R., Cairns W.R.L., Ebinghaus R., El Haddad I., Ferreira-Araujo B., Franck A., Huang L., Hyvärinen A., Humbert A., Kalogridis A.-C., Konstantinov P., Lampert A., MacLeod M., Magand O., Mahura A., Marelle L., Masloboev V., Moisseev D., Moschos V., Neckel N., Onishi T., Osterwalder S., Ovaska A., Paasonen P., Panchenko M., Pankratov F., Pernov J.B., Platis A., Popovicheva O., Raut J.-C., Riandet A., Sachs T., Salvatori R., Salzano R., Schröder L., Schön M., Shevchenko V., Skov H., Sonke J.E., Spolaor A., Stathopoulos V.K., Strahlendorff M., Thomas J.L., Vitale V., Vratolis S., Barbante C., Chabrillat S., Dommergue A., Eleftheriadis K., Heilimo J., Law K.S., Massling A., Noe S.M., Paris J.-D., Prévôt A.S.H., Riipinen I., Wehner B., Xie Z. & Lappalainen H.K. 2020. Overview: integrative and comprehensive understanding on polar environments (iCUPE)—concept and initial results. *Atmospheric Chemistry and Physics 20*, 8551–8592, doi: 10.5194/acp-20-8551-2020.

Porter C. 2018. Arctic DEM. Data set. University of Minnesota, doi: 10.7910/DVN/OHHUKH.

Rautenberg A., Schön M., zum Berge K., Mauz M., Manz P., Platis A., van Kesteren B., Suomi I., Kral S.T. & Bange J. 2019. The multi-purpose airborne sensor carrier MASC-3 for wind and turbulence measurements in the atmospheric boundary layer. *Sensors 19*, article no. 2292, doi: 10.3390/s19102292.

Schön M., zum Berge K., Platis A. & Bange J. 2022. UAS-based measurement of wind vector, temperature and humidity in Ny-Alesund, Svalbard, during April and May 2018. Data set. Tübingen University, PANGAEA, doi: 10.1594/PANGAEA.946961.

Svendsen H., Beszczynska-møller A., Hagen J.O., Lefauconnier B., Tverberg V., Gerland S., Ørbæk J.B., Bischof K., Papucci C., Zajaczkowski M., Azzolini R., Bruland O., Wiencke C., Winther J. & Dallmann W. 2002. The physical environment of Kongsfjorden–Krossfjorden, an Arctic fjord system in Svalbard. *Polar Research 21*, 133–166, doi: 10.3402/polar.v21i1.6479.

Tjernström M. & Graversen R.G. 2009. The vertical structure of the lower Arctic troposphere analysed from observations and the ERA-40 reanalysis. *Quarterly Journal of the Royal Meteorological Society 135*, 431–443, doi: 10.1002/qj.380.

van den Kroonenberg A., Martin T., Buschmann M., Bange J. & Vörsmann P. 2008. Measuring the wind vector using the autonomous mini aerial vehicle M2AV. *Journal of Atmospheric and Oceanic Technology 25*, 1969–1982, doi: 10.1175/2008JTECHA1114.1.

Vihma T., Kilpeläinen T., Manninen M., Sjöblom A., Jakobson E., Palo T., Jaagus J. & Maturilli M. 2011. Characteristics of temperature and humidity inversions and low-level jets over Svalbard fjords in spring. *Advances in Meteorology 2011*, article no. 486807, doi: 10.1155/2011/486807.

Wildmann N., Hofsäß M., Weimer F., Joos A. & Bange J. 2014. MASC-a small remotely piloted aircraft (RPA) for wind energy research. *Advances in Science and Research 11*, article no. 55, doi: 10.5194/asr-11-55-2014.

Wildmann N., Mauz M. & Bange J. 2013. Two fast temperature sensors for probing of the atmospheric boundary layer using small remotely piloted aircraft (RPA). *Atmospheric Measurement Techniques 6*, 2101–2113, doi: 10.5194/amt-6-2101-2013.

Wildmann N., Ravi S. & Bange J. 2014. Towards higher accuracy and better frequency response with standard multi-hole probes in turbulence measurement with remotely piloted aircraft (RPA). *Atmospheric Measurement Techniques 7*, 1027–1041, doi: 10.5194/amt-7-1027-2014.

A.2 Fair-Weather Atmospheric Charge Measurements with a Small UAS

Fair-Weather Atmospheric Charge Measurements with a Small UAS

MARTIN SCHÖN,[a] KERI ANNE NICOLL,[b] YANN GEORG BÜCHAU,[a] STEFAN CHINDEA,[c]
ANDREAS PLATIS,[a] AND JENS BANGE[a]

[a] *Department of Geosciences, Tübingen University, Tübingen, Germany*
[b] *Department of Meteorology, University of Reading, Reading, United Kingdom*
[c] *Department of Electronic and Electrical Engineering, University of Bath, Bath, United Kingdom*

(Manuscript received 10 March 2022, in final form 4 August 2022)

ABSTRACT: Atmospheric electricity measurements made from small unmanned aircraft systems (UAS) are rare but are of increasing interest to the atmospheric science community due to the information that they can provide about aerosol and turbulence characteristics of the atmospheric boundary layer (ABL). Here we present the first analysis of a new dataset of space charge and meteorology measurements made from the small, electric, fixed-wing UAS model MASC-3. Two distinct experiments are discussed: 1) Flights past a 99 m metal tower to test the response of the charge sensor to a fixed distortion of the electric field caused by the geometry of the tower. Excellent agreement is found between the charge sensor response from the MASC-3 and modeled electric field around the tower. 2) Vertical profiles up to an altitude of 2500 m to study the evolution of the ABL with the time of day. These flights demonstrated close agreement between the space charge profiles and temperature, relative humidity, and turbulence parameters, as would be expected on a fair-weather day with summertime convection. Maximum values of space charge measured were of order 70 pC m^{-3}, comparable with other measurements in the literature from balloon platforms. These measurements demonstrate the suitability of small UAS for atmospheric electrical measurements, provided that care is taken over the choice of aircraft platform, sensor placement, minimization of electrical interference, and careful choice of the flight path. Such aircraft are typically more cost-effective than manned aircraft and are being increasingly used for atmospheric science purposes.

KEYWORDS: Atmosphere; Atmospheric electricity; Aircraft observations; In situ atmospheric observations; Instrumentation/sensors; Measurements

1. Introduction

Charge is ubiquitous in Earth's atmosphere and is created by galactic cosmic rays from space, as well as surface radioactivity. Vertical separation of this positive and negative charge occurs in thunderstorms and electrified shower clouds, causing Earth's surface to become negatively charged, and the ionosphere (at approximately 70 km altitude) positively charged (Wilson 1921). This potential difference generates an atmospheric electric field (E-field), which is present globally, and is directed vertically, such that positive charge flows downward to Earth. Near the surface, the E-field is approximately -100 V m^{-1} during fair-weather conditions, and typically decreases in magnitude with height exponentially (Gish 1944). Clark (1957) devised a rough parameterization for the decrease of the E-field with height (E_z) in the troposphere in clear air [Eq. (1)]:

$$E_z = E_0 \exp^{-az}, \tag{1}$$

where E_0 is the surface E-field. The reciprocal of the scale height ($a = 0.25$ km^{-1}), and height (z) are in km. The presence of the atmospheric boundary layer as well as aerosol and cloud layers generally perturb this idealized profile, causing regions of increased E-field from the clear-air case (Fig. 1). Measurements of the E-field in fair-weather conditions are important for investigating Earth's global electric circuit, its connection to climate processes and processes in the atmospheric boundary layer (ABL) (Markson and Price 1999; Williams 2009; Rycroft et al. 2012). Atmospheric electrical variables can also provide information on the aerosol content of air (Sagalyn and Faucher 1954), including Saharan dust (Gringel and Muhleisen 1978; Nicoll et al. 2011) and volcanic ash (Harrison et al. 2010), as well as well as local turbulence characteristics (Markson et al. 1981). This is because the same meteorological processes that transport heat, momentum, moisture, and aerosol within the lower atmosphere also transport charge (Hoppel et al. 1986).

The vertical profile of the atmospheric electric field has been measured since the late 1800s (Tuma 1899), originally using water dropper sensors flown on hot air balloons. Since the early days of these measurements, electric field sensors and airborne platforms have developed substantially, with vertical profiles now typically measured with electric field mills carried by manned aircraft (Winn 1993; Bateman et al. 2007). Measuring the atmospheric E-field using an aircraft is challenging, because every measurement will be influenced by the aircraft's own E-field, which can lead to substantial measurement errors in regions of high E-fields, such as in convective clouds, thunderstorms, precipitation, or inside dust and aerosol plumes. While early aircraft measurements of E-field were made by using two E-field sensors mounted above and below the wing (Gunn 1947, 1948; Gish and Wait 1950), it was recognized that multiple E-field sensors were required in order to remove the effect of aircraft charge on the

---

Corresponding author: Martin Schön, martin.schoen@uni-tuebingen.de

DOI: 10.1175/JTECH-D-22-0025.1

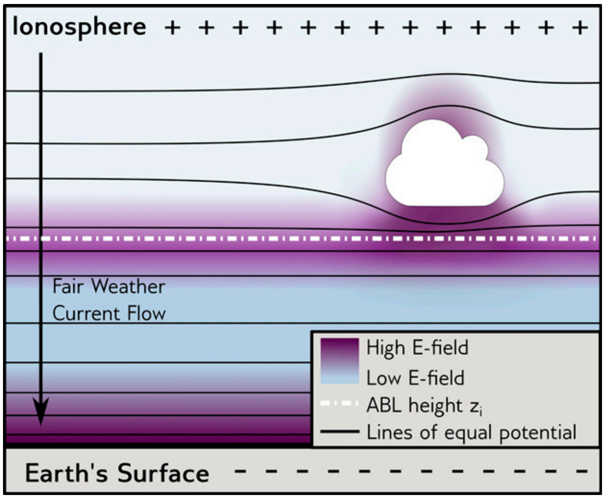

FIG. 1. Schematic of the atmospheric E-field, with the color shading representing the E-field intensity, and the black lines representing equal electric potential. In fair-weather conditions, current flows from the positively charged ionosphere to Earth's surface. Changes in the atmosphere's resistance, such as the capping inversion of the ABL or clouds create local distortions in the E-field. Distortions in the E-field can also be caused by thermodynamic processes. The E-field close to the surface is approximately -100 V m^{-1} during fair-weather conditions, and typically decreases in magnitude with height exponentially (Gish 1944).

measurements. In addition, charging of aircraft surfaces, which influences E-field measurements, can also result from the engine exhaust gases. Subsequent aircraft flights by Clark (1957, 1958) further characterized this distortion of the ambient E-field by the presence of the aircraft ("aircraft reduction factor"). Aircraft measurements of the atmospheric E-field are also affected by the movement of the aircraft itself. Since the total E-field $\mathbf{E}$ is a vector quantity, consisting of components E_x, E_y, and E_z, the motion of the aircraft can act to perturb one or more of these E-field components. This effect becomes even more pronounced with large changes in attitude, such as in turns. Winn (1993) discusses the various methods which have been used to correct for the motion of the aircraft. These include using scale models of aircraft (Laroche 1986), electrostatic modeling of the airframe (Mazur et al. 1987), and calibration maneuvering techniques (Winn 1993) to account for pitch and roll motion. More recent aircraft measurements of E-field have attempted to develop procedures to remove all of the above-described effects of the aircraft from the E-field measurements using ever more sophisticated methods. Koshak et al. (1994), Mach and Koshak (2007), and Mach (2015) discuss a detailed inversion matrix technique for calibrating aircraft E-field sensors, as well as a series of aircraft calibration maneuvers required to determine various calibration coefficients. For this technique to work well, several E-field sensors must be mounted on the aircraft (enough to measure at least one component of the E-field), with five to eight E-field sensors typically used. If the E-field sensors are small (as developed by Bateman et al. 2007), this is possible to implement on a large airframe, but not if payload capacity is limited, such as on small unmanned aerial systems (UAS).

The measurements mentioned above demonstrate that the E-field measured on a moving aircraft platform is often not a direct detection of the ambient E-field, but rather a combination of the aircraft-enhanced ambient field, aircraft motion, charge on the aircraft, and various other effects due to engine exhaust charging, or corona discharge when large E-fields are present. Therefore, it is necessary to remove all perturbations of the natural ambient field caused by the presence of the aircraft to detect the actual ambient field with aircraft measurements.

As opposed to the large aircraft mentioned above, small UAS as a platform for atmospheric electricity measurements are flexible, inexpensive, and allow measurements in conditions that are not possible for crewed aircraft (e.g., very close to the ground, near obstacles, or when launching and landing without any infrastructure). Despite the abundant availability of UAS for commercial and hobbyist applications, meteorological measurements from UAS are still relatively rare. Reasons for this include a lack of commercially available, low cost, high accuracy meteorological sensors, a lack of commercially available fixed wing platforms which are suitable for such measurements, complexities of autopilot operation, as well as challenges (both legal and practical) associated with flying at altitudes above standard visual line of sight limits. Technological developments are leading to more meteorological measurements from UAS (e.g., Pinto et al. 2021). Examples of UAS measurements in atmospheric electricity include the development of an "electrostatic autopilot" (Hill 1972, 1982), as well as the miniature E-field sensor measurements of Bateman et al. (2007) on the NASA Altus II UAS. More recently Zhang et al. (2016) instrumented a small UAS with multiple AC electrical potential sensors which utilize the pitch and roll movement of the aircraft to generate voltage differences between pairs of sensors mounted on the pitch and roll axes of the aircraft. Finally, Harrison et al. (2021) described measurements of space charge from a 2 m wingspan fixed UAS through a thin cloud layer.

In this work, we describe two types of measurement, made from a small fixed-wing UAS, model Multiple Purpose Airborne Sensor System (MASC-3). Its small size means that it is not feasible to carry a large number of E-field sensors as per the common approach used on larger aircraft. Instead, we have instrumented the airframe with highly sensitive bespoke miniature space charge sensors (Nicoll and Harrison 2009). Space charge ρ is the difference between positive and negative charge per unit volume, and is related to the divergence of the E-field, by Gauss's law [Eq. (2)]:

$$\nabla \cdot \mathbf{E} = \frac{\rho}{\epsilon_0}, \tag{2}$$

where ϵ_0 is the permittivity of free space, and $\mathbf{E}$ is a three-dimensional vector of orthogonal components E_x, E_y, and E_z. When measuring space charge in the ABL, we are concerned with the vertical profile of ρ which can be derived by considering the vertical component of the electric field, E_z (provided

TABLE 1. Technical data for the MASC-3 UAS with charge measurement pods attached.

Wingspan	4 m
Takeoff weight	8 kg
Payload	1.8 kg
Max endurance	1.5 h
Cruising/measurement airspeed	18.5 m s^{-1}
Service ceiling	4500 m AGL
Propulsion	Electric (pusher configuration)
Autopilot system	Cube, Arduplane firmware
Fuselage material	Glass fiber composite
Wing material	Carbon fiber composite

that variations in E_x and E_y are smaller than those in E_z, as is often the case in fair-weather conditions). Thus, ρ can be derived by Eq. (3), where z is the vertical coordinate, and the positive z direction is upward:

$$\rho = \epsilon_0 \frac{dE_z}{dz}. \tag{3}$$

We performed two types of measurements at the Meteorological Observatory Lindenberg, Richard-Aßmann Observatory (MOL-RAO) of the German Meteorological Service [Deutscher Wetterdienst (DWD)] in Germany. First, the validity of the charge sensor is tested by detecting a known distortion in the E-field caused by a 99 m metal tower, and comparing the measurement results with a model (section 3a). Second, we describe new measurements of vertical profiles of space charge. Flights took place only during fair-weather conditions, which minimized the effect of charge buildup on the airframe or corona discharge issues; and the lack of aircraft exhaust from the UAS (which uses an entirely electric propulsion system) means that there is no aircraft charging from emissions, unlike on a manned aircraft.

The instrumentation and aircraft platform are described in section 2a, and the flight location and experimental setup are described in section 2b. Sections 2c and 2d investigate the effect of aircraft movement on the charge measurements, and the development of a technique to remove it. While section 3a serves as a validation for the charge sensor by comparing the measurement to a known perturbation in the E-field caused by a metal tower, section 3b demonstrates the effectiveness of the charge sensor at measuring natural variations in space charge by describing vertical profiles of space charge and meteorological measurements in a series of flights within the ABL at different hours. A discussion section is provided in section 4 and conclusions in section 5.

2. Methods

a. UAS platform

The UAS flights described in this paper were performed by the MASC-3, a 4 m wingspan fixed-wing UAS for atmospheric measurements (Wildmann et al. 2014a; Mauz et al. 2019; Rautenberg et al. 2019) (Table 1, Fig. 2b). MASC-3 carries a sensor payload of up to 1.8 kg for measuring the three-dimensional wind vector and air temperature with a temporal resolution of up to 30 Hz, using a five-hole probe and a fine-wire platinum thermometer (Wildmann et al. 2013, 2014b) in combination with an inertial measurement unit (IMU). In addition, the relative humidity is measured using a slower digital temperature and humidity sensor. Data are logged and saved on board the aircraft at a sampling rate of 100 Hz (Rautenberg et al. 2019). MASC-3 is controlled by an autopilot, so it can repeat measurement patterns reliably. It performs all measurements during straight flight sections, with a constant airspeed of 18.5 m s^{-1}, and with the autopilot stabilizing the aircraft's attitude along the roll, yaw, and pitch axes (Fig. 2). Changes in flight direction are achieved by a change in the aircraft's attitude, mainly along the roll and yaw axes. However, turbulence can also change the aircraft's attitude during a straight section, with the autopilot working against these movements to stabilize the aircraft.

In addition to the standard sensor payload, two pods carrying charge sensors are attached to the wings, 1 m from the fuselage of the aircraft (Fig. 2). The charge sensors are similar to those described in Nicoll and Harrison (2009) and Nicoll (2013). They consist of a small (12 mm) spherical sensing electrode connected to an electrometer circuit. The sensors measure the rate of voltage change on the electrode, where the voltage change is due to the current flow between the atmosphere and the electrode due to the sensor's motion through an E-field. The circuit uses a current to voltage converter with a T network of resistors to minimize the need for high value resistors (as discussed in Nicoll 2013). Details of the method used to convert the measured charge sensor current to space charge are described in section 3e.

MASC-3 carries four of these charge sensors, with one "normal" range sensor and one "sensitive" sensor on each wing. The "sensitive" sensor provides an increased resolution, while the "normal" sensor has a wider range and is therefore more robust against saturation when measuring a strong signal. Both for the tower flyby (section 3a) and the vertical profiles of the ABL (section 3b) the "normal" sensor is better suited. Generally, the selection of the sensor sensitivity is done in post processing based on the range of the captured signal.

The sensors are mounted in the front of the pods so that the electrodes are about 20 cm away from the leading edge of the wing. The front part of the pods is wrapped with conductive copper foil. This reduces the potential influence of static charge buildup on the charge measurement. Both pods include a microcontroller-based logging system, which captures the analog 0–5 V signal from the charge sensors with a resolution of 14 bits and a sampling rate of 100 Hz directly to an SD card inside the pod. The time stamp of the charge sensor data and the rest of the sensor system are referenced to GPS time for synchronization.

b. Site description and experimental setup

The UAS flights described here took place at the DWD MOL-RAO, about 60 km southeast of Berlin (Fig. 3). Flights were performed during June 2021 by the Environmental Physics Workgroup of the University of Tübingen. The MOL-RAO site also includes a 99 m high meteorological measurement

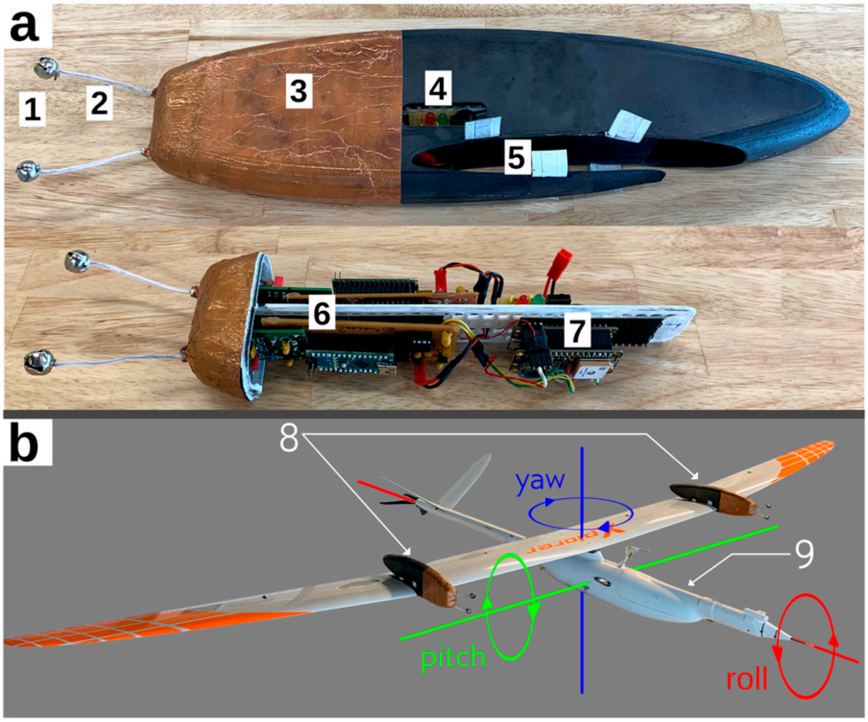

FIG. 2. (a) Charge sensor pod for MASC-3. 1) Sensing electrode, 2) plastic-covered connector to sensor board, 3) shell painted with conductive graphite paint, front section covered in conductive copper foil, 4) status lights, 5) wing mount, 6) sensor board, and an analog-digital converter, 7) Adafruit Feather microcontroller for logging and GPS antenna for creating time stamps. (b) MASC-3 with charge sensor pods attached. 8) The charge sensor pods are covered in conductive copper foil to reduce the influence of static charge around the nonconductive surface of the wings. 9) The sensor payload is in the front for measuring the wind vector, temperature, and humidity. The three dimensions of movement (yaw, pitch, roll) of MASC-3 are measured by the IMU mounted in the sensor payload.

mast, located at 14.1222°N, 52.1665°E, 73 m above mean sea level (MSL). The site is flat, with a maximum variation in terrain elevation of 10 m within a 5 km radius.

To test the response of the charge sensors on the UAS, two types of measurement flight were conducted. To validate the MASC-3 space charge measurement, an experiment was designed in which MASC-3 flies through a known distortion in the E-field, caused by the measurement tower. To establish this reference for the measurements of MASC-3, the E-field around the tower was modeled in the COMSOL physics software (electrostatics package) (COMSOL 2021). Like any large metal object, the tower perturbs the E-field around it, which causes changes in the charge sensor output as the MASC-3 flies past it. The space charge calculated from the charge sensor output is then compared to the divergence of the modeled E-field. (section 3a).

The second pattern involved vertical profiles, where MASC-3 climbs to 2500 m above ground with a constant vertical velocity of 1.5 m s^{-1} in a series of 1.5-km-long sections (Fig. 4). From these sections, only a central section of 800 m length is used for analysis to further reduce the influence of the turns at the end of the sections. This flight pattern aimed to measure natural perturbations in the E-field caused by variation of the ABL in fair weather and is discussed in section 3b. Of this pattern, a total of 13 flights were conducted (as shown in Table 2).

To perform these measurement flights beyond the pilot's visual line of sight (BVLOS) at these altitudes, special permits are required in most countries. In the case presented here, the flights were made possible by the establishment of a no-fly zone and subsequent permits for BVLOS UAS flights. In the European Union, these permits are not necessarily expensive, but it is important to contact the relevant authorities at an early stage, as such procedures may take a long time and be quite extensive, depending on the risk assessment of the planned flights.

c. *Effect of UAS movement on charge measurements*

Aircraft movement is well known to affect E-field measurements made from manned aircraft platforms (Winn 1993; Mach and Koshak 2007). Winn (1993) suggest that the total charge Q induced on an E-field sensor electrode is a linear sum of the contributions of the E-field in the x, y, and z directions (E_x, E_y, E_z) as well as the charge on the aircraft Q_A [Eq. (4)]:

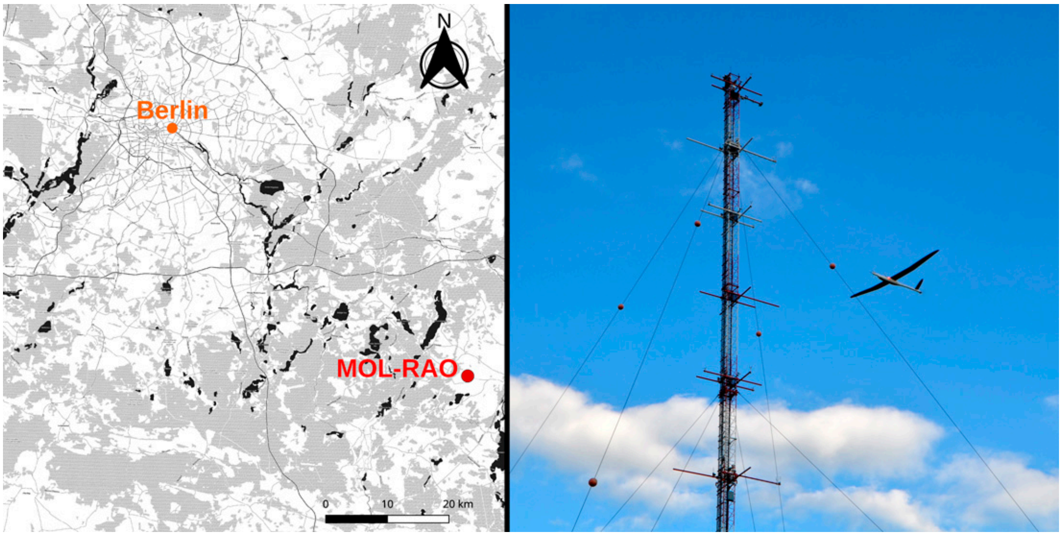

FIG. 3. (left) Location of the MOL-RAO meteorological tower and (right) MASC-3 passing the tower during a measurement flight.

$$Q = aE_x + bE_y + cE_z + Q_A \tag{4}$$

(where *a*, *b*, and *c* are coefficients specific to the aircraft). Aircraft charging is most likely to occur when flying through layers of droplets (e.g., clouds) or particles (dust, sand, smoke, ash). By flying in only fair-weather conditions with no clouds or haze layers, the effects of Q_A are minimized so that this term becomes negligible.

The E_x and E_y terms will likely be most sensitive to pitch and roll maneuvers from the UAS, and the E_z term will vary with UAS altitude as the aircraft climbs or descends. The degree to which the E-field measurement is affected by pitch and roll movements depends on the placement of the sensors with respect to the various axes of rotation of the UAS. For the MASC-3, the charge sensor pods were deliberately mounted on the wings, relatively close to the aircraft's main body (1 m distance), rather than nearer the wingtips. Placement toward the end of the wings would result in a much larger sensitivity to roll maneuvers due to the larger angles through which the UAS wings move.

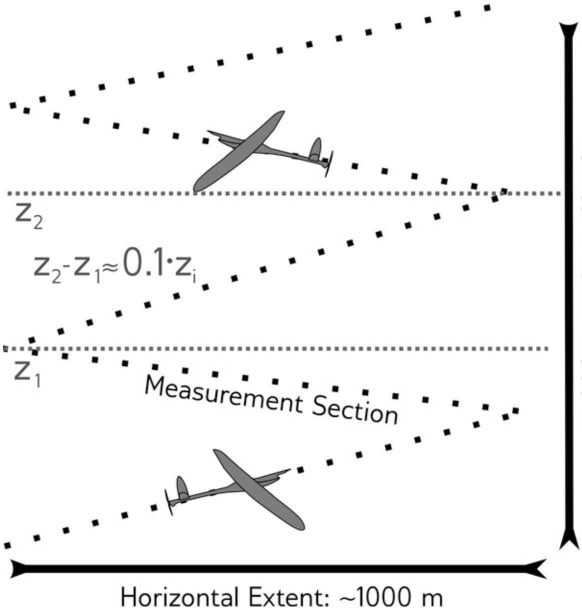

FIG. 4. MASC-3 flight path for the vertical profile flights. The profile is divided into several sections. Each pair of these sections (upwind and downwind) covers a height of 10% of the boundary layer height $0.1z_i$. The maximum altitude for each flight varies, dependent on weather situation and airspace restrictions; see Table 2.

The dependence of the charge sensors on the UAS movement was investigated by cross correlating the charge sensor voltage output with all MASC-3 flight parameters, including roll angle, roll velocity, pitch velocity, and yaw velocity (aircraft axes are depicted in Fig. 2b), for multiple measurement flights. The result of this was an observed high correlation between charge sensor output and roll velocity (with a maximum correlation coefficient between 0.6 and 0.9, at a lag between 0.1 and 0.3 s). A less significant correlation with pitch velocity was observed, with typical correlation coefficients between 0.2 and 0.4. The high correlation with roll velocity is likely due to the placement of the charge sensors. Since the sensors are mounted on the wings, 1 m away from the aircraft's axis of rotation, a slight roll movement is translated by the leverage into a fast absolute movement of the charge sensor, while the sensor's movement is minimal during a pitch movement, since it is only about 20 cm away from the pitch axis. Correlation to movement around the yaw axis is not detected, and MASC-3 is generally more stable in the yaw axis than in the roll or pitch axes.

To further investigate the sensitivity of the charge sensors to changes in the UAS roll velocity, calibration maneuvers were devised in which the human pilot deliberately performed a slow rolling motion of the aircraft. This is demonstrated in Fig. 5. A strong correlation is seen between the charge sensor output and the roll velocity of the MASC-3. Figure 5 shows the data for the sensor located on the right wing (which is

TABLE 2. Overview of the MASC-3 measurement flights with charge sensor pods performed in May and June 2021. The tower flyby flight (discussed in section 3a), and vertical profiles discussed in section 3b are highlighted in boldface. Time is local time (LT): central European summer time.

Flight No.	Date	Time (LT: CEST)	Type	Max altitude (m AGL)
Calibration	3 May 2021	1400–1423	Horizontal legs	100
1	9 Jun 2021	1553–1700	Vertical profile	2200
2	10 Jun 2021	0914–1032	Vertical profile	700
3	10 Jun 2021	1124–1233	Vertical profile	1700
4	10 Jun 2021	1413–1530	Vertical profile	2000
5	10 Jun 2021	1556–1645	Vertical profile	2000
6	13 Jun 2021	1902–2000	Vertical profile	2100
7	14 Jun 2021	0705–0808	Vertical profile	2100
8	14 Jun 2021	0903–1015	Vertical profile	1600
9	14 Jun 2021	1357–1501	Vertical profile	1780
10	14 Jun 2021	1657–1745	Vertical profile	1750
11	16 Jun 2021	2016–2130	Tower flyby	150
12	17 Jun 2021	0953–1130	Vertical profile	2360
13	17 Jun 2021	1400–1500	Vertical profile	2500
14	17 Jun 2021	1653–1830	Vertical profile	2300

positively correlated with roll velocity). The left wing charge sensor shows an equal but opposite (i.e., negative) correlation with roll velocity, as expected (not shown here). To minimize the influence of the roll maneuvers of MASC-3 on the charge sensor output, the measurement flights were carried out as a series of straight, 1-km-long sections, which are called measurement legs (for straight and level sections) or measurement sections (for straight sections including an ascent/descent) in the remainder of this study. Only these sections are taken into account in the data analysis sections 3a and 3b, and data from the turns are discarded (as the charge sensor often saturates due to the high roll velocities from the UAS). For sections with roll velocities below 0.2 rad s^{-1}, the correlation coefficient of the charge sensor and the roll velocity drops below 0.5. Although this approach minimizes the influence of the roll velocity on the charge sensor data, it does not remove it completely. For example, the roll influence is visible in straight measurement sections when the MASC-3 autopilot performs roll movements to compensate for atmospheric turbulence. This may be a problem in turbulent conditions, such as a convective ABL, where a charge signal with a higher amplitude is measured due to the stronger roll movements. Therefore, a roll velocity correction to the charge sensor data is required to interpret the charge sensor measurements.

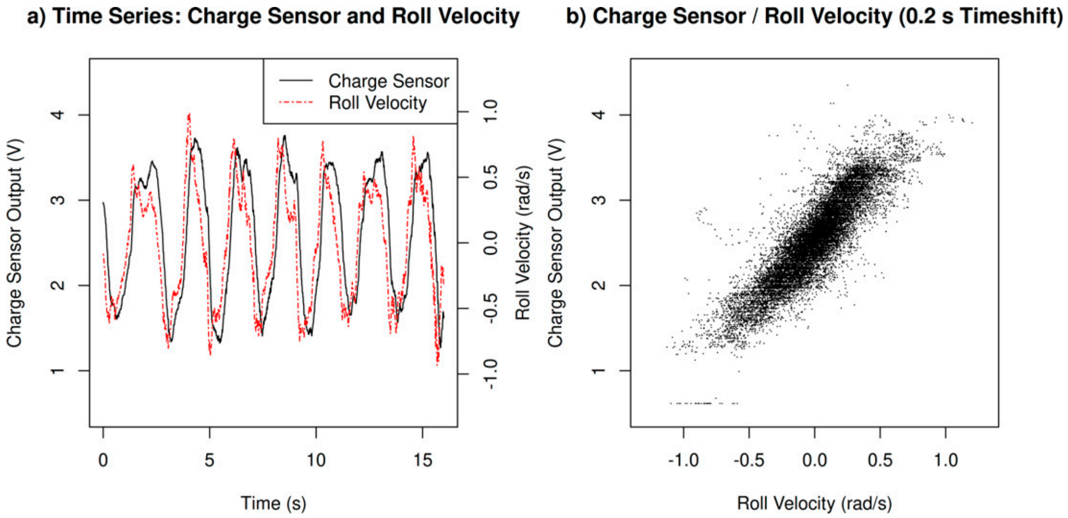

FIG. 5. (a) Time series of charge sensor signal (black) and roll velocity (red) for a calibration leg with an oscillating roll movement generated by the pilot. The time shift between roll movement and charge sensor response is approximately 0.2 s. (b) Relationship between roll speed and charge sensor output for an entire flight with pilot-generated roll movement, created from 108 s of data sampled with 100 Hz. Roll velocity data are time-shifted by 0.2 s to account for the lag in the charge sensor response.

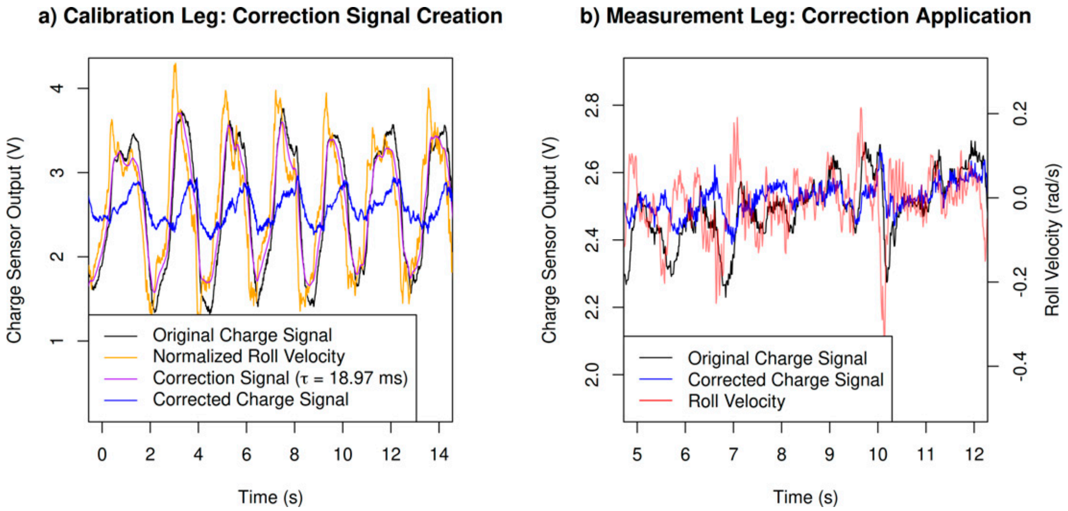

FIG. 6. (a) Calibration leg containing a rolling motion created by the pilot to determine the charge signal's time constant. The normalized roll velocity ($v_{\mathrm{roll,norm}}$, orange) is filtered with an exponentially weighted moving average (EMWA) to match the original charge signal (U_{raw}, black) as closely as possible. The resulting optimized signal (S_{corr}, purple) is then subtracted from the charge signal to obtain a corrected charge signal (U_{corr}, blue). The optimization of the EMWA kernel yields a time constant τ of 18.97 ms for the charge sensor signal. (b) The parameters calculated in the calibration leg are used to filter the influence of roll velocity (red) on the charge measurement (black) in a measurement leg of the same flight as the calibration leg. The filtered signal (blue) shows a reduced influence of the rolling motion. Note the lower amplitude of both charge and roll velocity during measurement legs without intentionally created rolling motion.

d. *Exponential smoothing correction method*

With the roll velocity and charge measurements recorded during the calibration flight (Table 2), a correction method for the charge measurements can be implemented. This method uses the roll velocity to generate a correction signal that is subtracted from the charge sensor signal to eliminate roll influence as much as possible. When comparing the charge sensor output signal (0–5 V), U_{raw} and roll velocity signal v_{roll}, a lag between the two signals is apparent (typically 0.1–0.3 s, depending on the sensor). The charge sensors slower response time causes its response to resemble a smoothed and lagged version of the roll velocity signal. A simple method of modeling this response is by filtering an appropriately normalized roll velocity signal $v_{\mathrm{roll,norm}}$ with an exponentially weighted moving average (EWMA) (Holt 2004). We obtain $v_{\mathrm{roll,norm}}$ using the anomalies of roll velocity during a calibration leg, $v'_{\mathrm{roll,calib}}$, which are scaled to have the same signal energy as the charge signal anomalies $U'_{\mathrm{raw,calib}}$ (Guido 2016) and then shifted to match the charge signal mean [Eq. (5)]:

$$v_{\mathrm{roll,norm}} = \sqrt{\frac{\int |U'_{\mathrm{raw,calib}}|^2 dt}{\int |v'_{\mathrm{roll,calib}}|^2 dt}}\, v'_{\mathrm{roll}} + \overline{U_{\mathrm{raw}}}. \qquad (5)$$

Applying the EMWA filter on the normalized roll velocity $v_{\mathrm{roll,norm}}$ yields a correction signal s_{corr}, which closely models the roll velocity's influence on the charge signal [Eq. (6)]:

$$s_{\mathrm{corr}} = v_{\mathrm{roll,norm}} k_{\mathrm{exp}}(\tau). \qquad (6)$$

To find the kernel $k_{\mathrm{exp}}(\tau)$ for the EMWA filter, we use the charge sensor's time-constant τ. Determining τ is possible by minimizing a cost function representing the deviation between $s_{\mathrm{corr}}(\tau)$ and U_{raw} in a flight leg with reasonably strong, controlled, pilot-induced roll movements where no external influence on the charge sensor is expected (Fig. 6). The roll velocity during this calibration must be high enough to produce a clear signal in the charge sensor but low enough not to cause saturation of the sensor. We used the root-mean-squared error (RMSE) as a cost function. Subtracting s_{corr} from the raw charge signal c_{raw} results in a corrected charge signal c_{corr} with reduced roll velocity influence [Eq. (7)]:

$$U_{\mathrm{corr}} = U_{\mathrm{raw}} - s_{\mathrm{corr}}. \qquad (7)$$

The results of this correction method are shown in Fig. 6 for both a calibration leg and a normal straight leg during a measurement flight. Our proposed correction method greatly reduces the roll velocity's influence on the charge sensor signal. For the calibration period (Fig. 6a), the signal energy of the erroneously oscillating charge signal is reduced by 85%. In a straight leg of the same flight, numerous roll-induced peaks in the charge measurement are diminished, leaving a cleaner and easier to interpret time series (Fig. 6b). For legs and flight sections during the measurement flights performed in Lindenberg (Table 2), the correlation coefficients between v_{roll} and charge are reduced from 0.5–0.6 to ≈0.4 by implementing the filtering approach.

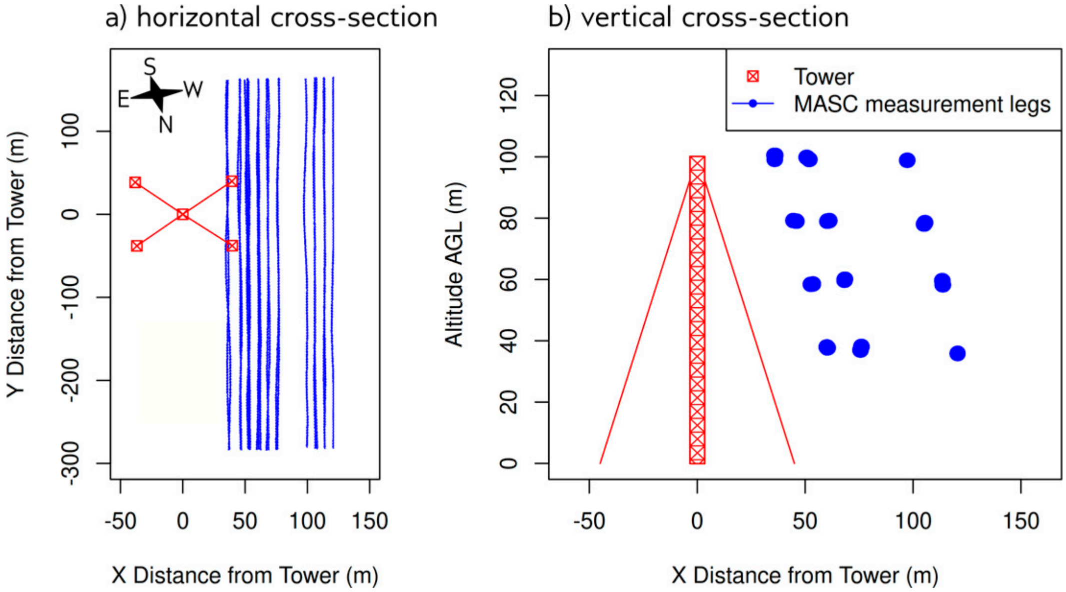

FIG. 7. (a) Top view and (b) profile of the meteorological tower at Falkenberg including its guy ropes (red) and the MASC-3 measurement legs next to the tower (blue). The coordinate system is relative to the position of the tower.

e. *Space charge calculation*

The space charge measured by the charge sensor is derived using a series of procedures detailed below. First, the current I_i is calculated from the corrected (as described in section 2d) 0–5 V output of the sensor U_{corr}, as the sensor is essentially a displacement current sensor, which produces a current in response to a varying E-field [Eq. (8)]:

$$I_i = \frac{-(U_{\mathrm{corr}} - U_{\mathrm{bg}})}{R_{\mathrm{sensor}}}. \tag{8}$$

The value of the gain resistor is $R_{\mathrm{sensor}} = 2.4 \times 10^{11}\Omega$, and U_{bg} is the background voltage of the charge sensor (this is typically 2.55 V for the flights discussed on 14 June).

Second, I_i is then converted to space charge ρ [Eq. (9)], by dividing I_i by the vertical speed of MASC-3 w_{MASC} multiplied with the effective area term of the sensor $A_{\mathrm{eff}} = 0.02\ \mathrm{m}^2$, derived from experimental calibration (Nicoll and Harrison 2016):

$$\rho = \frac{I_i}{A_{\mathrm{eff}}} w_{\mathrm{MASC}}. \tag{9}$$

It is assumed that in fair-weather conditions, any changes in space charge in the horizontal will be minimal and that changes in the vertical will dominate the space charge measurement. For vertical profiles of the ABL, we therefore use the vertical speed w_{MASC} measured by the IMU aboard MASC-3 (in m s $^{-1}$, positive upward). For the flights presented here, this is $w_{\mathrm{MASC}} \approx 1.5\ \mathrm{m\ s}^{-1}$. Finally, only the absolute value of space charge is used here as discussed in Nicoll et al. (2018).

3. Results

a. *Tower flyby*

To validate the response of the charge sensor to changes in the ambient E-field on a moving UAS platform, a series of flights were performed next to a 99 m meteorological measurement tower. This was located at the MOL-RAO of the DWD in the area of Brandenburg, Germany, 60 km southeast from Berlin. The structure of the tower consists of a 99 m metal mast, supported by four guy ropes (which extend diagonally 45 m from the center of the tower), as shown in Fig. 7. It is well understood that the existence of such a tower will distort the ambient atmospheric E-field around it due to the enhanced geometry of the structure. As such, flying the UAS past the tower at various distances and altitudes provides a control experiment testing the response of the charge sensor to the variations in the E-field caused by the tower. Figure 7 shows the various flight legs performed with the UAS at four altitudes (40, 60, 80, and 100 m). Per altitude, measurement legs were flown as repeated 400 m straight legs past the tower at three different horizontal distances (coordinate x). For the lowest altitude of 40 m, these distances are 60, 80, and 120 m from the center of the tower. In an attempt to follow the angle of the guy ropes, the horizontal distance from the tower became smaller with altitude (as shown in Fig. 7b), but always maintained a consistent (closest) distance of 40 m from the guy ropes.

To model the distortion of the E-field around the tower, the COMSOL physics software was used. This solves Gauss's law for the electric field using the scalar electric potential as the dependent variable. The tower was modeled as a 99 m tall, 5 m diameter metal conductor, with four diagonal conductive guy ropes, all of which are earthed. As an approximation of the ambient fair-weather atmospheric E-field, the

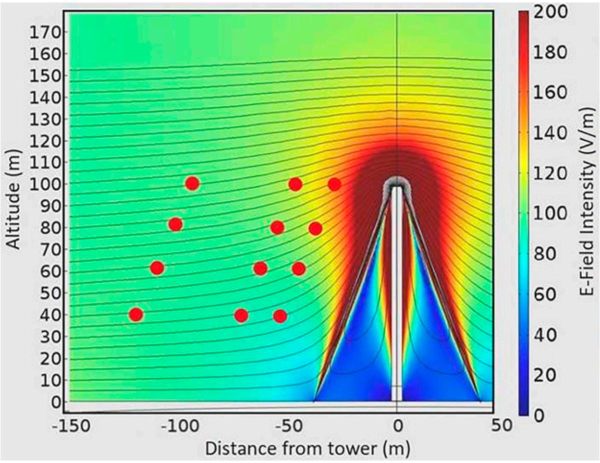

FIG. 8. COMSOL modeling of distortion of E-field around a 99 m mast. Colored contours show modeled E-field and black lines are lines of equal electric potential at 20 m intervals (from 20 to 100 m). Red circles denote the location of the UAS flight legs as in Fig. 7.

E-field is generated by a parallel plate capacitor setup with a vertical separation distance between the plates of 300 m. The capacitor is cylindrical (to enable axial symmetry), and the top plate is at 30 000 V, in effect generating a uniform E-field of 100 V m^{-1}. Figure 8 shows the modeled E-field around the tower through a cut plane at 45° to the x axis (i.e., the guy ropes appear on either side of the tower as in Fig. 7b). It is seen that the intensity of the E-field drops significantly in between 0 and 50 m distance from the tower and varies with altitude. The equipotential lines are highly curved close to the tower and guy ropes, but this decreases with horizontal distance and is negligible at distances of 2–3 times the towers height (i.e., beyond 200 m). It should be noted that the model of the tower is very much an approximation of the real tower, hence the COMSOL simulation will not capture any effects of corona discharge, which may affect the E-field and space charge around sharp points such as crossbeams on the tower. The fair-weather conditions (and hence small ambient atmospheric E-fields) during the flights should minimize this issue.

An example of the typical response of the charge sensor as the UAS flies past the tower is shown in Fig. 9. This illustrates that the charge sensor voltage is relatively stable on approach to the tower (i.e., left-hand side of the plot). When the UAS gets within 50 m (coordinate y as shown in Fig. 8b) of the tower, the charge sensor voltage decreases and reaches a minimum at the closest distance to the tower. As the UAS continues to fly past the tower, the charge sensor voltage increases and returns to approximately its original value. Although the example shown in Fig. 9 is for the flight leg flown at 40 m horizontal x distance from the tower at an altitude of 80 m AGL, all of the flight legs in Fig. 7 show a similar type of response for the charge sensor, just with varying values of voltage change. To calculate the space charge ρ from this signal, Eq. (9) has to modified for this experiment to use the velocity along the flight path v instead of the vertical velocity w, since the E-field mainly changes along the flight path, as the aircraft passes the influence of the tower.

As such, we calculate the maximum space charge $\rho_{\max}$ for each flight leg within a coordinate y of ±100 m from the center of the tower. This calculation is made for each of the 12 flight legs (i.e., straight and level flight sections) at different x distances and altitudes from the tower as shown in Fig. 8b. $\rho_{\max}$ for each leg are shown as black crosses in Fig. 10, illustrating an exponential decrease in ρ with x distance from the tower.

As described in Eq. (3), ρ is directly related to the divergence of the E-field along the component along which the E-field is changing most. For the E-field around the tower, we assume this component to be the distance to the tower r. Therefore, a qualitative comparison between the divergence of the simulated E-field with respect to the distance to the

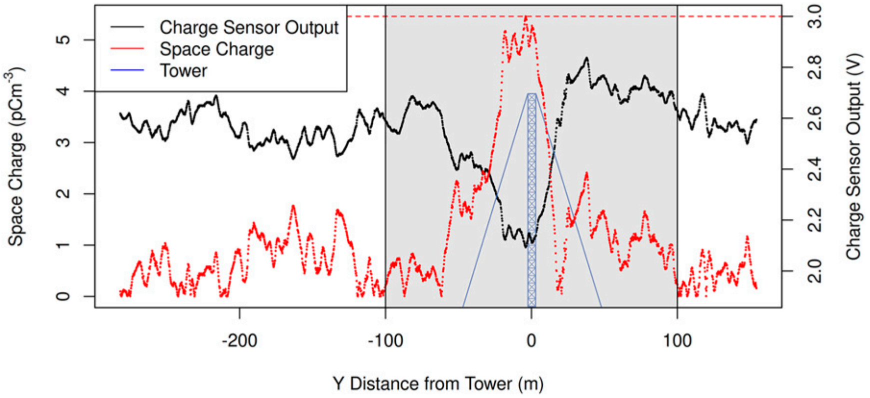

FIG. 9. The typical response of the charge sensor (black) during a measurement leg at an altitude of 80 m AGL with the closest distance of 40 m to the tower. The local minimum of the waveform is typically around the point closest to the tower, the local maximum within 100 m after passing the tower. Space charge is calculated from this measurement leg (red), with the maximum space charge within a ±100 m distance along the y coordinate along the tower (red dashed line).

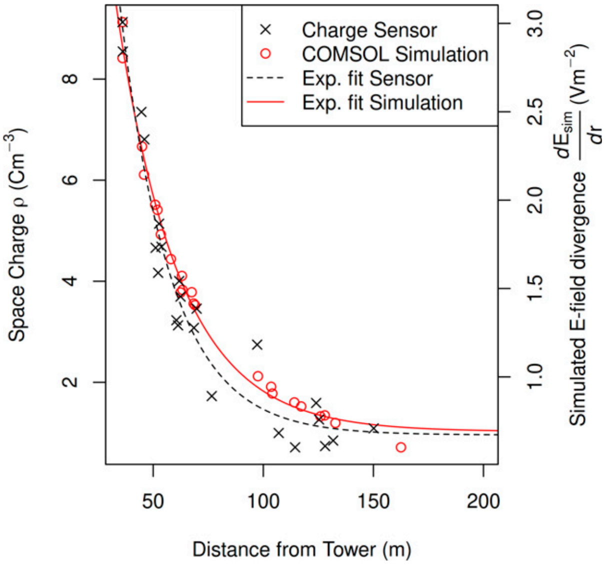

FIG. 10. Comparison of E-field divergence in relation to the distance to the tower dE_{sim}/dr from COMSOL simulation with charge sensor space charge ρ in relation to the lateral distance from the tower. Exponential fit is of the form $y(x) = y_f + (y_0 - y_f)e^{-\alpha x}$, where $\alpha = 0.043$ km^{-1} for the measured data and $\alpha = 0.035$ km^{-1} for the simulation.

tower, dE_{sim}/dr, and the measured space charge ρ is possible. Both dE_{sim}/dr and ρ show an exponential decrease with increasing r (Fig. 10). Exponential fits of the form $y(x) = y_f + (y_0 - y_f)e^{-\alpha x}$ to the measured and modeled data demonstrate that the values of the coefficients of the exponents, α, are similar between the two fits (0.043 km^{-1} for the measured data and 0.035 km^{-1} for the modeled data). This gives confidence that the charge sensor responds to the E-field distortion produced by the tower in an expected way.

b. *Vertical profiles*

To investigate the response of the charge sensor mounted on MASC-3 to natural variations in E-field, vertical profiles were performed throughout the ABL at the MOL-RAO. Of the 13 vertical profiles mentioned in Table 2, three of these are selected here for detailed analysis. These flights were performed on the same day (14 June 2021) to study the evolution of the ABL, with flights occurring at 0700, 0900, and 1400 local time (LT; CEST). The weather conditions were dominated by fair weather, with relatively high pressure (1016–1011 hPa). Scattered clouds in the early morning dissipated shortly after sunrise, followed by cloudless conditions for the remainder of the day. The maximum temperature was 25°C, and near-surface wind speed was very low throughout the day, at 1–2 m s^{-1}. Figure 11 shows vertical profiles of the meteorological variables measured during 14 June from MASC-3 (including temperature, relative humidity, wind speed, k), and the absolute value of space charge derived from the normal charge sensor on the right wing.

Starting with the first vertical profile at 0700 LT, the temperature profile is stable, with an inversion at 190 m MSL (120 m AGL) (Fig. 11a). This is a manifestation of the nocturnal boundary layer from the previous night. The wind speed (Fig. 11b) increases almost linearly up to the altitude of the capping inversion (z_i). Examination of the space charge profile (Figs. 11c,d) shows little variation in space charge with height and values typically up to 20 pC m^{-3}. There is a hint of slightly larger values of space charge within the ABL, but this is not significant. By the time of the second flight at 0900 LT (Fig. 11e), the morning transition eroded the ground-based temperature inversion, and the temperature decreases almost linearly with height, following the dry adiabatic lapse rate (DALR). The temperature inversion at 1 km has strengthened. Figure 11f shows that k also starts to increase within the ABL, signifying that convective processes are becoming dominant. Evidence of this is also present in the space charge profile (Figs. 11g,h), which shows much more variability than the previous flight, with three distinct layers forming at approximately 0–400, 600–700, and 800–1000 m. Values of up to 70 pC m^{-3} are now observed. The space charge correlates with k and is significantly stronger within the ABL than above, demonstrating the strong link between space charge and turbulent processes and that the space charge is prevented from mixing to higher altitudes by the capping inversion. By the time of the final flight at 1400 LT, the ABL is well mixed, with the height of z_i increasing to 1.5 km, and the k values approximately constant with height to this altitude. The distinct layers of space charge from the 0900 LT profile have been replaced by a profile that shows high variability with values of up to 40 pC m^{-3} over the complete profile up to the maximum flight altitude of 1.5 km (Fig. 11k).

4. Discussion

This paper addresses three aspects to test whether a small UAS is a suitable platform for atmospheric electricity measurements.

First, the influence of aircraft movement on the E-field around an aircraft, which is a phenomenon described in depth in the literature (Clark 1957, 1958; Winn 1993; Laroche 1986; Mazur et al. 1987; Koshak et al. 1994; Mach and Koshak 2007; Mach 2015) has to be evaluated, and the influence of the aircraft on the charge sensor signal must be isolated as far as possible. MASC-3 is a pusher aircraft, with the propeller located at the back of the UAS, more than 1 m distant from any of the sensors. This ensures minimal disruption to the charge sensors from the propulsion system. The design of the sensor pods also helps reducing interference to the charge sensors. The geometry of the pods was specially designed to minimize turbulent airflow around the sensors, and mounting them tens of centimeters in front of the wings also assists with this. The placement of the pods, relatively close to the center of the aircraft body, is a compromise between minimizing the effect of roll velocity on the charge measurements and an increased risk of problems from a buildup of static charge on the aircraft fuselage (which cannot be made entirely conductive as this would affect radio communication with the UAS). By

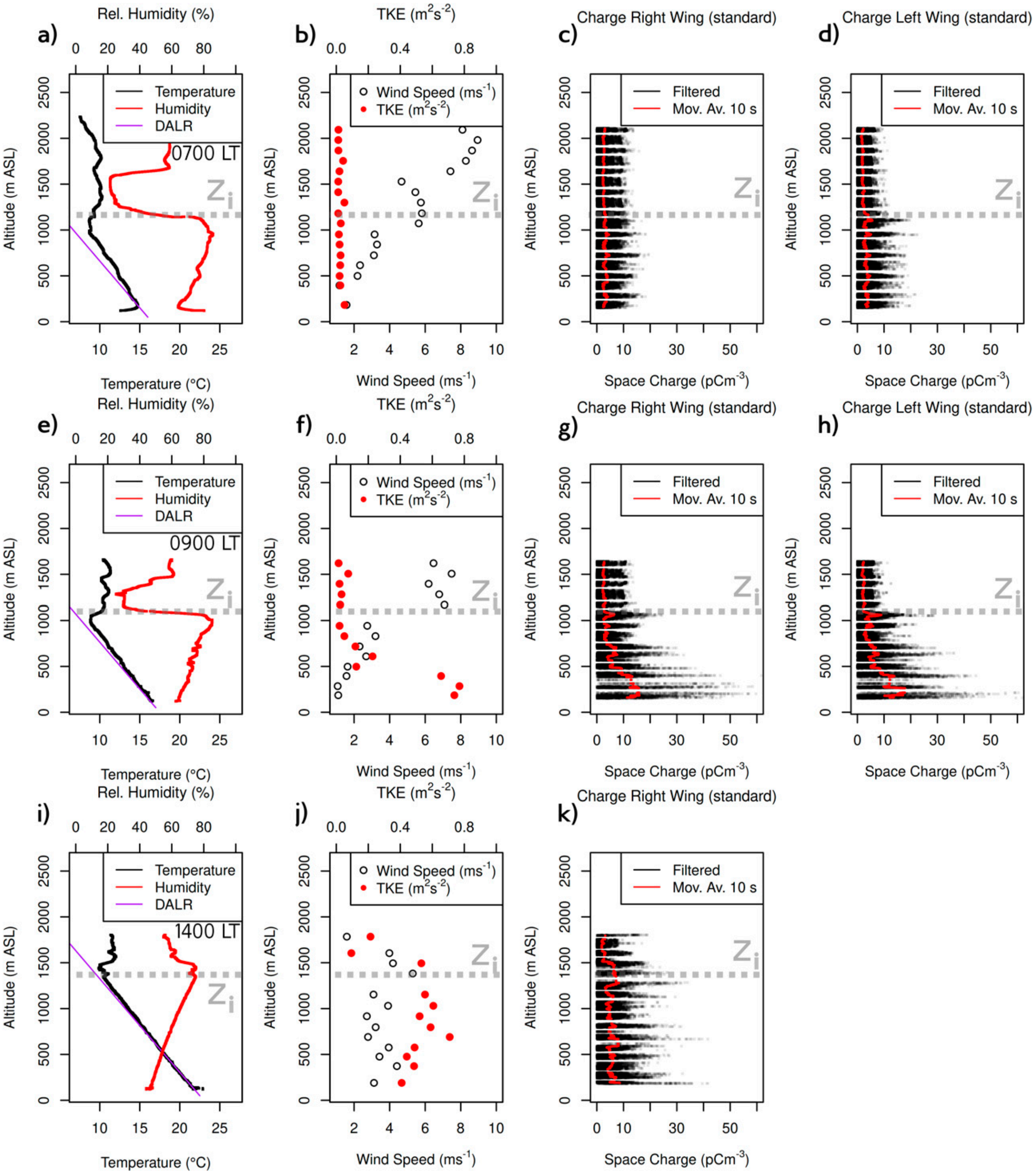

FIG. 11. MASC-3 vertical profiles showing the ABL development on 14 Jun 2021. The altitude of the capping inversion z_i is marked by a dashed gray line. Time information is in local time (LT; CEST). Wind speed and TKE k (as described in the appendix) is per 800 m measurement section, space charge is calculated according to the method in section 2e, with each black dot representing a space charge measurement at 100 Hz sampling rate. The red line in the space charge profiles shows a 10 s moving average of space charge. For the flights at 0700 and 0900 LT, the space charge is calculated from the “standard” range sensors on the left and right wings; for the flight at 1400 LT, the left wing sensor malfunctioned, so only the right wing sensor is shown.

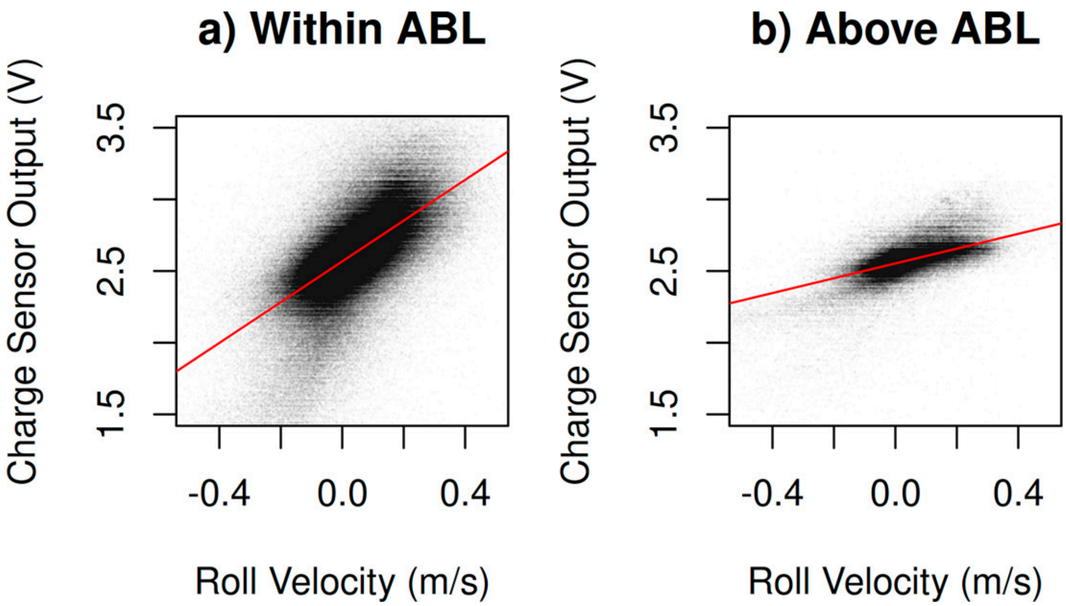

FIG. 12. Comparison of the different responses of the charge sensor to the roll velocity (a) in the boundary layer and (b) above the boundary layer in the free atmosphere. The data shown are composed of all measurement flights in which a clear inversion is identifiable as the upper limit of the ABL (flights 6, 7, 8, 9, 10, and 13). Note that the data shown contain the turns, as there is not enough rolling motion on the straight measurement sections to make a clear correlation discernible. The data are not corrected for roll velocity, and are time-shifted by 0.2 s to account for the time-shift in the charge sensor measurement (Fig. 5).

mounting the charge sensors at a distance from the surface of the wings and encasing them in a conductive housing, the influence of any static charge that may build up during flight on the wings is also minimized. Using an entirely electric aircraft also removes any chance of charging the aircraft body from exhaust emissions. To minimize electrical noise from the aircraft systems, the power supply and logging of the charge sensors were completely decoupled from the rest of the aircraft. Another thing of importance to the quality of the charge measurements is the flight path of the UAS. Section 2c demonstrates the importance of roll velocity influence on the charge sensor measurements. Although this can be removed through developing a calibration method (as discussed in section 2d), it is also good practice to minimize the roll velocity to ensure that the sensor does not saturate. Here we employ a flight path that prioritizes long straight sections with minimal turns (and the turns are not included in the analysis of the final scientific measurements). Although the exact dependency of the movement of the UAS on the charge measurements (be it roll, yaw, or pitch) will depend on the placement of the sensors on the aircraft, it is good practice to try to minimize the effect of such movements to minimize the complexity of correction method required. Proper tuning of the autopilot's flight control is also important, as it can greatly increase the stability of the UAS. As mentioned in section 2c, flying in straight sections minimizes the effect of the roll velocity on the measurements but does not completely delete it. This is particularly apparent when the UAS is flying within the ABL in convective conditions, and the autopilot makes corrections to the flight path to account for turbulent motions. Figure 12 demonstrates the relationship between the roll velocity and charge sensor output voltage below the ABL (Fig. 12a) and above it (Fig. 12b). There is an approximately linear relationship between the two in both cases, but the gradient is steeper in the ABL (1.9 V $\mathrm{m}^{-1}\,\mathrm{s}^{-1}$) than above it (0.5 V $\mathrm{m}^{-1}\,\mathrm{s}^{-1}$). This is likely related to the aircraft's fuselage charging up more within the ABL than above it, which leads to an increased influence of the aircraft's motion on the charge sensors. A similar effect was reported by Hill (1982), who demonstrated that the gradient of the relationship between the bank angle of their UAS and E-field was steeper at 2000 ft (~600 m) than at 6000 ft (~1800 m). Thus, flying above the ABL, rather than below it, is also advantageous to minimize the effects of aircraft movement on charge measurements. The correction method described in section 2d could be further improved by performing separate calibrations in and above the ABL.

Second, the flight past a metallic meteorological tower serves as a validation of the charge sensors and can be compared well with physical models. It enables investigating the behavior of the charge sensors on MASC-3 under controlled and reproducible conditions (section 3a). The results show excellent agreement between the space charge measured by the sensor and the divergence of the E-field in the COMSOL simulation (Fig. 10). This shows that MASC-3 can reliably measure the space charge when the influence of the movement of the aircraft is removed.

Third, the first half of the diurnal cycle of a convective (fair weather) ABL is investigated, thus applying the measurement technique to a meteorological problem under realistic conditions (section 3b). The vertical profiles (Fig. 11) demonstrate the similarities between the space charge profiles and the meteorological profiles, which has been observed in other similar studies from balloons (e.g., Nicoll et al. 2018) and manned aircraft (Sagalyn and Faucher 1954). The magnitude of the space charge (up to 70 pC m^{-3}) is also comparable with balloon measurements of the same charge sensor as reported in Nicoll et al. (2018), which detected space charge of up to 100 pC m^{-3} in the ABL in fair-weather conditions. This provides further evidence that the space charge measurements from the MASC-3 are responding to natural variations in the E-field.

5. Conclusions

This study presents the first analysis of a new series of space charge and meteorology measurements made from a small unmanned aircraft platform. Charge measurements were made from wing-mounted probes using a 4-m-wingspan fixed-wing UAS known as MASC-3. Flight data demonstrate a dependence of the charge sensor output on roll velocity of the UAS, which is corrected for using a series of calibration maneuvers during a calibration flight. A series of flights past a 99 m metal tower demonstrated excellent agreement between the charge sensor response and expected distortion in the E-field caused by the geometry of the mast, as modeled using the COMSOL electrostatic modeling software. Several vertical profile flights (up to 2.5 km) performed at different times during a fair-weather day characterized the evolution of the ABL. This demonstrated a close agreement between the space charge profiles and meteorological variables (particularly turbulence and boundary layer height), as would be expected on a fair-weather day with summertime convection.

The flight data discussed here support the conclusion that it is possible to make sensible measurements of space charge in fair-weather conditions from small unmanned aircraft, which are not significantly affected by the presence and movement of the aircraft. Further, this is possible with only a single small, inexpensive sensor and relatively straightforward data processing techniques. This contrasts with the E-field measurements from crewed aircraft discussed in the literature, which typically require many sensors and complex analysis techniques to derive accurate measurements of fair-weather E-fields. Due to the increasing use of UAS in atmospheric science, this is an important finding, which may drive forward an increase in atmospheric electricity measurements from such platforms, and will help characterize and study the ABL and aerosol processes, including the transport of dust and volcanic ash layers. Additionally, further research into developing small and light E-field sensors is worth pursuing, since this would allow the E-field to be measured directly with small UAS.

Acknowledgments. We thank the following people for their support for the work: the pilot of MASC-3, Henrik Rieth; colleagues in the Environmental Physics Workgroup of the University of Tübingen, Jakob Boventer, Ines Weber, and Kjell zum Berge, who maintained MASC-3, provided the logistics and legal framework for the measurement flights, and provided valuable support during the interpretation of the results; Frank Beyrich and the German Meteorological Service (DWD) for providing the infrastructure at the MOL-RAO and the invaluable support during and after the measurements. The measurements in Falkenberg, which provided the data basis for this paper, were performed as a supplement to a lidar validation flight project funded by the German Meteorological Service (DWD) under the funding code 4819EMF01 (VALUAS). KAN acknowledges a NERC Independent Research Fellowship (NE/L011514/1) and (NE/L011514/2).

Data availability statement. The data that support the findings of this study are available from the corresponding author, Martin Schön, upon reasonable request.

APPENDIX

Calculation of Turbulent Kinetic Energy

To obtain a vertical profile of the ABL, MASC-3 flies a series of measurement sections at a constant rate of climb from the ground to beyond the capping inversion of the ABL (Fig. 4). From these measurement sections, the temperature and humidity measurements are plotted as vertical profiles (Fig. 11a).

As a measure of turbulent fluctuations, the turbulent kinetic energy k is calculated for each measurement section (Fig. 11). Since the measurement sections are not horizontal but slant (from altitudes z_1 to z_2, Fig. 4), k [Eq. (10)] is representative not only for a particular height but for a volume defined by z_1, z_2, and the length of the slant flight section above ground. For the flights presented here, $z_2 - z_1$ is around 10% of the ABL height z_i. By ensuring the duration of each measurement section is longer than the integral time scale $\mathcal{T}$ of the wind components u, v, and w, the measured volume includes the largest vortices present in the ABL (Stull 2015; Bange et al. 2013, 2002). For all measurement sections presented here, $\mathcal{T}$ is lower than 9 s, while the duration of each measurement section is around 50 s:

$$k = 0.5 \times (\overline{u'^2} + \overline{v'^2} + \overline{w'^2}). \tag{A1}$$

REFERENCES

Bange, J., F. Beyrich, and D. A. M. Engelbart, 2002: Airborne measurements of turbulent fluxes during LITFASS-98: Comparison with ground measurements and remote sensing in a case study. *Theor. Appl. Climatol.*, **73**, 35–51, https://doi.org/10.1007/s00704-002-0692-6.

——, and Coauthors, 2013: Measurement of aircraft state, thermodynamic and dynamic variables. *Airborne Measurements for Environmental Research: Methods and Instruments*, 1st ed. M. Wendisch and J.-L. Brenguier, Eds., John Wiley and Sons, 7–75.

Bateman, M. G., M. F. Stewart, S. J. Podgorny, H. J. Christian, D. M. Mach, R. J. Blakeslee, J. C. Bailey, and D. Daskar, 2007: A low-noise, microprocessor-controlled, internally digitizing rotating-vane electric field mill for airborne platforms.

J. Atmos. Oceanic Technol., **24**, 1245–1255, https://doi.org/10.1175/JTECH2039.1.

Clark, J. F., 1957: Airborne measurement of atmospheric potential gradient. *J. Geophys. Res.*, **62**, 617–628, https://doi.org/10.1029/JZ062i004p00617.

——, 1958: The fair-weather atmospheric electrical potential and its gradient. *Recent Advances in Atmospheric Electricity*, 1st ed. L. G. Smith, Ed., Pergamon Press, 61–73.

COMSOL, 2021: COMSOL: Multiphysics software for optimizing designs. Accessed 12 November 2021, https://uk.comsol.com/.

Gish, O. H., 1944: Evaluation and interpretation of the columnar resistance of the atmosphere. *Terr. Magn. Atmos. Electr.*, **49**, 159–168, https://doi.org/10.1029/TE049i003p00159.

——, and G. R. Wait, 1950: Thunderstorms and the Earth's general electrification. *J. Geophys. Res.*, **55**, 473–484, https://doi.org/10.1029/JZ055i004p00473.

Gringel, W., and R. Muhleisen, 1978: Sahara dust concentration on the troposphere over the North Atlantic derived from measurements of air conductivity. *Contrib. Atmos. Phys.*, **51**, 121–128.

Guido, R. C., 2016: A tutorial on signal energy and its applications. *Neurocomputing*, **179**, 264–282, https://doi.org/10.1016/j.neucom.2015.12.012.

Gunn, R., 1947: The electrical charge on precipitation at various altitudes and its relation to thunderstorms. *Phys. Rev.*, **71**, 181–186, https://doi.org/10.1103/PhysRev.71.181.

——, 1948: Electric field intensity inside of natural clouds. *J. Appl. Phys.*, **19**, 481, https://doi.org/10.1063/1.1698159.

Harrison, R. G., K. A. Nicoll, Z. Ulanowski, and T. A. Mather, 2010: Self-charging of the Eyjafjallajökull volcanic ash plume. *Environ. Res. Lett.*, **5**, 024004, https://doi.org/10.1088/1748-9326/5/2/024004.

——, and Coauthors, 2021: Demonstration of a remotely piloted atmospheric measurement and charge release platform for geoengineering. *J. Atmos. Oceanic Technol.*, **38**, 63–75, https://doi.org/10.1175/JTECH-D-20-0092.1.

Hill, M. L., 1972: Introducing the electrostatic autopilot. *AIAA J.*, **10**, 22–31.

——, 1982: Influence of meteorological processes on the verticality of electric fields. Johns Hopkins University Applied Physics Laboratory Tech. Rep. ADA111549, 16 pp., https://doi.org/10.21236/ADA111549.

Holt, C. C., 2004: Forecasting seasonals and trends by exponentially weighted moving averages. *Int. J. Forecast.*, **20**, 5–10, https://doi.org/10.1016/j.ijforecast.2003.09.015.

Hoppel, W., R. V. Anderson, and J. C. Willet, 1986: Atmospheric electricity in the planetary boundary layer. *The Earth's Electrical Environment*, 1st ed. E. P. Krider and R. G. Roble, Eds., National Academies Press, 149–165, https://doi.org/10.17226/898.

Koshak, W. J., J. Bailey, H. J. Christian, and D. M. Mach, 1994: Aircraft electric field measurements: Calibration and ambient field retrieval. *J. Geophys. Res.*, **99**, 22 781–22 792, https://doi.org/10.1029/94JD01682.

Laroche, P., 1986: Airborne measurements of electrical atmospheric field produced by convective clouds. *Rev. Phys. Appl.*, **21**, 809–815, https://doi.org/10.1051/rphysap:019860021012080900.

Mach, D. M., 2015: Technique for reducing the effects of nonlinear terms on electric field measurements of electric field sensor arrays on aircraft platforms. *J. Atmos. Oceanic Technol.*, **32**, 993–1003, https://doi.org/10.1175/JTECH-D-14-00029.1.

——, and W. J. Koshak, 2007: General matrix inversion technique for the calibration of electric field sensor arrays on aircraft platforms. *J. Atmos. Oceanic Technol.*, **24**, 1576–1587, https://doi.org/10.1175/JTECH2080.1.

Markson, R., and C. Price, 1999: Ionospheric potential as a proxy index for global temperature. *Atmos. Res.*, **51**, 309–314, https://doi.org/10.1016/S0169-8095(99)00015-0.

——, J. Sedlácék, and C. W. Fairall, 1981: Turbulent transport of electric charge in the marine atmospheric boundary layer. *J. Geophys. Res.*, **86**, 12 115–12 121, https://doi.org/10.1029/JC086iC12p12115.

Mauz, M., A. Rautenberg, A. Platis, M. Cormier, and J. Bange, 2019: First identification and quantification of detached-tip vortices behind a wind energy converter using fixed-wing unmanned aircraft system. *Wind Energy Sci.*, **4**, 451–463, https://doi.org/10.5194/wes-4-451-2019.

Mazur, V., L. H. Ruhnke, and T. Rudolph, 1987: Effect of E-field mill location on accuracy of electric field measurements with instrumented airplane. *J. Geophys. Res.*, **92**, 12 013–12 019, https://doi.org/10.1029/JD092iD10p12013.

Nicoll, K. A., 2013: A self-calibrating electrometer for atmospheric charge measurements from a balloon platform. *Rev. Sci. Instrum.*, **84**, 096107, https://doi.org/10.1063/1.4821500.

——, and R. G. Harrison, 2009: A lightweight balloon-carried cloud charge sensor. *Rev. Sci. Instrum.*, **80**, 014501, https://doi.org/10.1063/1.3065090.

——, and ——, 2016: Stratiform cloud electrification: Comparison of theory with multiple in-cloud measurements. *Quart. J. Roy. Meteor. Soc.*, **142**, 2679–2691, https://doi.org/10.1002/qj.2858.

——, ——, and Z. Ulanowski, 2011: Observations of Saharan dust layer electrification. *Environ. Res. Lett.*, **6**, 014001, https://doi.org/10.1088/1748-9326/6/1/014001.

——, ——, H. G. Silva, R. Salgado, M. Melgâo, and D. Bortoli, 2018: Electrical sensing of the dynamical structure of the planetary boundary layer. *Atmos. Res.*, **202**, 81–95, https://doi.org/10.1016/j.atmosres.2017.11.009.

Pinto, J. O., and Coauthors, 2021: The status and future of small uncrewed aircraft systems (UAS) in operational meteorology. *Bull. Amer. Meteor. Soc.*, **102**, E2121–E2136, https://doi.org/10.1175/BAMS-D-20-0138.1.

Rautenberg, A., and Coauthors, 2019: The Multi-Purpose Airborne Sensor Carrier MASC-3 for wind and turbulence measurements in the atmospheric boundary layer. *Sensors*, **19**, 2292, https://doi.org/10.3390/s19102292.

Rycroft, M. J., K. A. Nicoll, K. A. Aplin, and R. Giles Harrison, 2012: Recent advances in global electric circuit coupling between the space environment and the troposphere. *J. Atmos. Sol.-Terr. Phys.*, **90–91**, 198–211, https://doi.org/10.1016/j.jastp.2012.03.015.

Sagalyn, R. C., and G. A. Faucher, 1954: Aircraft investigation of the large ion content and conductivity of the atmosphere and their relation to meteorological factors. *J. Atmos. Terr. Phys.*, **5**, 253–272, https://doi.org/10.1016/0021-9169(54)90046-X.

Stull, R., 2015: Turbulence kinetic energy. *Practical Meteorology: An Algebra-Based Survey of Atmospheric Science*, John Wiley and Sons, 708 pp.

Tuma, J., 1899: Beiträge zur Kenntniss der atmosphärischen Elektricität III. Luftelektricitäts-Messungen im Luftballon. *Sitzungsber. Akad. Wiss. Wien, Math.-Naturwiss. Kl.*, **108**, 227–260.

Wildmann, N., M. Mauz, and J. Bange, 2013: Two fast temperature sensors for probing of the atmospheric boundary layer using small remotely piloted aircraft (RPA). *Atmos. Meas. Tech.*, **6**, 2101–2113, https://doi.org/10.5194/amt-6-2101-2013.

——, M. Hofsäß, F. Weimer, A. Joos, and J. Bange, 2014a: MASC—A small remotely piloted aircraft (RPA) for wind energy research. *Adv. Sci. Res.*, **11**, 55–61, https://doi.org/10.5194/asr-11-55-2014.

——, S. Ravi, and J. Bange, 2014b: Towards higher accuracy and better frequency response with standard multi-hole probes in turbulence measurement with remotely piloted aircraft (RPA). *Atmos. Meas. Tech.*, **7**, 1027–1041, https://doi.org/10.5194/amt-7-1027-2014.

Williams, E. R., 2009: The global electrical circuit: A review. *Atmos. Res.*, **91**, 140–152, https://doi.org/10.1016/j.atmosres.2008.05.018.

Wilson, C. T. R., 1921: Investigations on lighting discharges and on the electric field of thunderstorms. *Philos. Trans. Roy. Soc.*, **221**, 73–115, https://doi.org/10.1098/rsta.1921.0003.

Winn, W. P., 1993: Aircraft measurement of electric field: Self-calibration. *J. Geophys. Res.*, **98**, 7351–7365, https://doi.org/10.1029/93JD00165.

Zhang, Y., E. Duff, A. Agundes, B. Yeik, and K. L. Cummins, 2016: Small UAV airborne electric field measurements. *24th Int. Lightning Detection Conf.–6th Int. Lightning Meteorology Conf.*, San Diego, CA, Vaisala.

A.3 OPC-Pod: A New Sensor Payload to Measure Aerosol Particles for Small Uncrewed Aircraft Systems

OPC-Pod: A New Sensor Payload to Measure Aerosol Particles for Small Uncrewed Aircraft Systems

Martin Schön,[a] Vasileios Savvakis,[a] Maria Kezoudi,[b] Andreas Platis,[a] Jens Bange,[a]

[a] *Department of Geosciences, Tübingen University, Germany*

[b] *Climate and Atmosphere Research Center (CARE-C), The Cyprus Institute, Nicosia, Cyprus*

Corresponding author: Martin Schön, martin.schoen@uni-tuebingen.de

Early Online Release: This preliminary version has been accepted for publication in *Journal of Atmospheric and Oceanic Technology*, may be fully cited, and has been assigned DOI 10.1175/JTECH-D-23-0078.1. The final typeset copyedited article will replace the EOR at the above DOI when it is published.

ABSTRACT: Atmospheric aerosols affect human health and influence atmospheric and biological processes. Dust can be transported long distances in the atmosphere, and the mechanisms that influence dust transport are not fully understood. To improve the data base for numerical models that simulate dust transport, measurements are needed that cover both the vertical distribution of the dust and its size distribution. In addition to measurements with crewed aircraft, uncrewed aircraft systems (UAS) provide a particularly suitable platform for this purpose. In this paper we present the OPC-Pod, a payload for the small fixed-wing UAS of the type MASC-3 for aerosol particle measurements. The OPC-Pod is based on the optical particle counter (OPC) OPC-N3 (Alphasense, UK), modified by the addition of a dryer and a passive aspiration system. Based on field tests with a reference instrument in Mannheim, Germany, wind tunnel tests and a comparison measurement with the UAS-mounted aerosol particle measurement system UCASS during a dust event over Cyprus, we show that the OPC-Pod can measure particle number concentrations in the range 0.66 - 31 μm as well as particle size distributions. The agreement of ther OPC-Pod with UCASS is good. Both instruments resolve a vertical profile of the Saharan dust event, with a prominent dust layer between 1500 m and 2800 m above sea level, with particle number concentrations up to 35 cm^{-3} for particles between 0.66 - 31 μm.

Accepted for publication in *Journal of Atmospheric and Oceanic Technology*. DOI 10.1175/JTECH-D-23-0078.1.

1. Introduction

Aerosol particles significantly influence climate and weather processes and affect human health. They can directly influence atmospheric processes by scattering and absorbing sunlight (Chung 2012; Papadimas et al. 2012) and indirectly influence cloud formation and albedo by acting as cloud condensation nuclei (CCN) (Lohmann and Feichter 2005). In addition, ionization variations in the atmosphere can induce electrification of aerosol particles, potentially impacting CCN concentrations and altering cloud presence (Harrison 2000). One type of particulate matter affecting Europe is Saharan dust. This dust has various deposition hotspots throughout the continent, often affecting the Mediterranean (Stuut et al. 2009), and it can significantly affect human health (Karanasiou et al. 2012). The frequency of these dust events follows a seasonal pattern, with the most intense events occurring in the eastern Mediterranean region during spring (Moulin et al. 1998), fall and winter (Athanasopoulou et al. 2016). A trend towards more frequent events has been observed over the years (Varga 2020).

Numerical weather prediction (NWP) models and satellite image analysis have shown the significant influence of Saharan dust on the European climate (Helmert et al. 2007; Bangert et al. 2012; Mauro et al. 2019). The main transport lane of the dust to Europe is the Mediterranean region (Israelevich et al. 2012), through which it reaches Central Europe, although there have been rare cases of observed amounts in Northern Europe and the Arctic region (Ansmann et al. 2003; Barkan and Alpert 2010; Varga 2020). Saharan dust is also transported across the Atlantic, influencing weather systems and directly impacting marine and terrestrial ecosystems by acting as a fertilizer (Swap et al. 1992; Dunion and Velden 2004; Jickells et al. 2005; Yu et al. 2015).

Modern dust forecast systems assimilate aerosol particle data collected by satellites (Niu et al. 2008; Benedetti et al. 2009; Tomaso et al. 2017) and ground-based remote sensing measurements such as the Aerosol Robotic Network (AERONET). Satellite and AERONET observations provide reliable data sets over long time periods and provide information on dust transport over large areas. These passive remote sensing methods are based on the measurement of solar radiation loss due to dust in the air, expressed as aerosol optical depth or AOD (Niu et al. 2008; Gkikas et al. 2012). Dust models such as the Monitoring Atmospheric Composition and Climate (MACC-ECMWF, Inness et al. 2013) show good agreement with AOD measurements over the entire column due to the assimilation of satellite data (Chouza et al. 2016). However, the Copernicus Atmosphere

Monitoring Service (CAMS, successor of the MACC model) does not correctly estimate the vertical transport of aerosol particles in the Atmospheric Boundary Layer (ABL) (O'Sullivan et al. 2020) and underpredicts coarse-mode (> 1 μm) aerosol particles at higher altitudes (Kok et al. 2021). Several studies suggest that numerical models do not simulate all the processes needed to correctly represent dust transport, such as electrical charging of particles (Harrison et al. 2018) and convective processes (Gasteiger et al. 2017; Pilon et al. 2022). Because the interaction between dust and the atmosphere is not always straightforward, it is necessary to gather information on aerosol particle number concentration (PNC), size distribution (O'Sullivan et al. 2020) and physical properties of aerosol particles (Pöschl et al. 2010; Heintzenberg 2012) to understand their impact on climate and weather processes. In situ measurements can fill this gap by providing high-resolution case studies of aerosol size distribution and vertical distribution for comparison with NWP models, and data for fundamental research into the mechanisms behind dust transport (Mamali et al. 2018).

In-situ dust measurements require an airborne platform capable of collecting data at the altitudes of the dust layer. In the case of Saharan dust, this includes the entire troposphere up to about 10 km (Gobbi et al. 2000; Papayannis et al. 2008). Existing balloon-based solutions (e.g. Renard et al. 2016a; Smith et al. 2019; Kezoudi et al. 2021a) can reach such altitudes because their maximum altitude is limited only by buoyancy. In contrast, fixed-wing or rotary-wing aircraft, both crewed and uncrewed, are more limited in their maximum altitude. However, aircraft can provide much higher vertical resolution than untethered balloons, as they are more controllable and higher resolution vertical profiles can be achieved (Pikridas et al. 2019).

To better understand the spatial evolution and mixing processes of a dust layer, measurements of the three-dimensional wind vector, temperature, and humidity are also required. This is the unique capability of the Multiple-Purpose Airborne Sensor Carrier 3 (MASC-3) Uncrewed Aircraft System (UAS) presented here, which can measure these meteorological parameters (Rautenberg et al. 2019) in addition to the PNC measurement presented here. With its maximum altitude of 6 km, MASC-3 can fly high enough to cover a significant portion of the troposphere for capturing dust events or to capture the vertical distribution of aerosol particles in the ABL and above.

While several studies conducted in-situ measurements of Saharan dust using crewed aircraft (McConnell et al. 2010; Johnson and Osborne 2011; Denjean et al. 2016), newly developed lightweight and inexpensive particle sensors allow measurements on small uncrewed aircraft systems (UAS)

(Bates et al. 2013; Altstädter et al. 2015; Brady et al. 2016; de Boer et al. 2016; Platis et al. 2016; Renard et al. 2016b; Schrod et al. 2017; Bezantakos et al. 2018; Kezoudi et al. 2021b) and balloons (Renard et al. 2016a, 2018; Smith et al. 2019; Kezoudi et al. 2021a). Optical particle counters (OPCs) are used in most of these studies because they can be compact and inexpensive. These sensors provide information on particulate matter (PM), PNC, and size distributions, often from accumulation to coarse mode, making them suitable for most in-situ aerosol measurement experiments. Mamali et al. (2018) presented the first Saharan dust measurements using an OPC on an UAS.

This work focuses on the development and validation of the small, lightweight aerosol particle measurement system OPC-Pod for use on the UAS MASC-3 in conjunction with the existing meteorological sensors (Rautenberg et al. 2019) and atmospheric charge sensors (Schön et al. 2022). It aims to extend current research and previous applications of similar sensor payloads. The measurement system is based on the commercially available OPC-N3 from Alphasense (Alphasense 2019), modified for use on fixed-wing UAS. While the focus of this development has been to create a measurement system for Saharan dust, the OPC-Pod can also be used to measure other types of aerosol particles.

The OPC-N3 is integrated into a wing shaped pod (the OPC-Pod). The OPC-Pod also contains a diffusion dryer, a mass flow sensor and a data logger. Since the built-in fan of the OPC-N3 is not sufficient to aspirate the OPC equipped with a diffusion dryer in flight, and since carrying a pump capable of providing sufficient airflow for the OPC-N3 would exceed the strict weight restrictions of a small UAS, the required sample airflow for the OPC-N3 is generated by a passive aspiration system described in Mashni et al. (2023) using the pressure differences at the surface of the OPC-Pod.

The OPC-Pod is mounted on the wing of UAS MASC-3, along with a standard payload for high-resolution temperature, humidity, and wind vector measurement in the nose of the aircraft. This combination of sensors provides wind and temperature data with sufficient resolution to calculate vertical fluxes (Rautenberg et al. 2019) that affect the transport of dust particles. A space charge sensor is used for atmospheric electricity measurements (Schön et al. 2022). This unique combination of sensors allows in-situ measurements of both the vertical distribution of aerosol particles in the atmosphere and the particle size distribution. In addition, the relationship of the aerosol measurements with the simultaneously measured thermodynamic quantities can be investigated.

Finally, hygroscopic growth, which increases apparent particle size in humid air, must be considered. Most aerosol particles found in the atmosphere undergo hygroscopic growth at sub-saturated conditions, especially in the sub-micron range (Swietlicki et al. 2008). It has been shown that Saharan dust also exhibits hygroscopic behavior (Koehler et al. 2009). Therefore, for accurate measurements, the OPC-Pod is equipped with a self-constructed lightweight diffusion drying chamber (Savvakis et al. 2023).

In Section 2a, the construction and operation of the OPC-Pod are described in detail. Section 2c describes validation measurements of the OPC-Pod on the ground, using an unmodified OPC N-3 and a Palas Fidas 200 as reference instruments. Section 2d describes a laboratory comparison of the OPC-Pod with an unmodified OPC N-3 in a wind tunnel. Finally, section 2e describes an in-situ measurement of Saharan dust at the Orounda airfield, Nicosia, Cyprus, during a Saharan dust event on 6 April 2022, where MASC-3 performed a vertical profile up to 3000 m ASL. Because the three experiments build on each other, results and discussion for each of the experiments are presented separately. The field tests are discussed in section 3, the windtunnel test in section 4, and the flight measurements in section 5.

2. Methods

a. MASC-3 and meteorological sensor payload

The OPC-Pod is mounted on the right wing of MASC-3, a fixed-wing UAS with a 4 m wingspan used for atmospheric measurements (Fig. 1). MASC-3 carries a meteorological sensor payload in its nose that measures the three-dimensional wind vector, air temperature, and humidity at a sampling rate of 100 Hz, which is recorded using an on-board data logger. The wind vector and air temperature can be resolved up to 30 Hz using a five-hole probe and fine-wire platinum thermometer (Wildmann et al. 2013, 2014; Rautenberg et al. 2019). The left wing of MASC-3 is equipped with a pod containing two sensors for measuring atmospheric charge (Schön et al. 2022). All sensor systems are synchronized using the GPS timestamp. MASC-3 is equipped with an autopilot and long-range telemetry for command and control, allowing reliable repetition of measurement patterns and control of the aircraft in Beyond Visual Line of Sight (BVLOS)

Fig. 1. MASC-3 directly after takeoff, flying away from the camera, at the Unmanned System Research Laboratory (USRL; Kezoudi et al. 2021b) airfield of the Cyprus Institute, near Orounda, Cyprus. The atmospheric charge measurement pod is mounted on the left wing, while the OPC-Pod is mounted on the right wing. The meteorological sensor payload is on the nose of the aircraft. The low visibility in the background is due to a Saharan dust event. Photo by Christos Keleshis, Cyprus Institute.

conditions. All measurements were performed in straight flight sections with a constant indicated airspeed of 18.5 m s^{-1} and a constant rate of climb or descent of 1.5 m s^{-1}. The maximum flight time of MASC-3 is 1.5 hours and it can reach altitudes up to 6 km ASL.

b. OPC-Pod

The OPC-Pod (Fig. 2) is equipped with a modified OPC of type N3 by Alphasense, outfitted with a diffusion dryer. The sensor was chosen because of its low cost, light weight (100 g) and its large measuring range. The bin boundaries for the instrument are listed in Tab. A1. According to the manufacturer Alphasense, the OPC-N3's maximum coincidence probability is 0.24% for concentrations of 0.5 cm^{-3}, and 0.84% for concentrations of 1000 cm^{-3} (Alphasense 2019). The sensor has been shown to have high accuracy against reference instrumentation, and a low positive bias when operating at ambient conditions (Sousan et al. 2021). It has also been shown that the

Accepted for publication in *Journal of Atmospheric and Oceanic Technology.* DOI 10.1175/JTECH-D-23-0078.1.

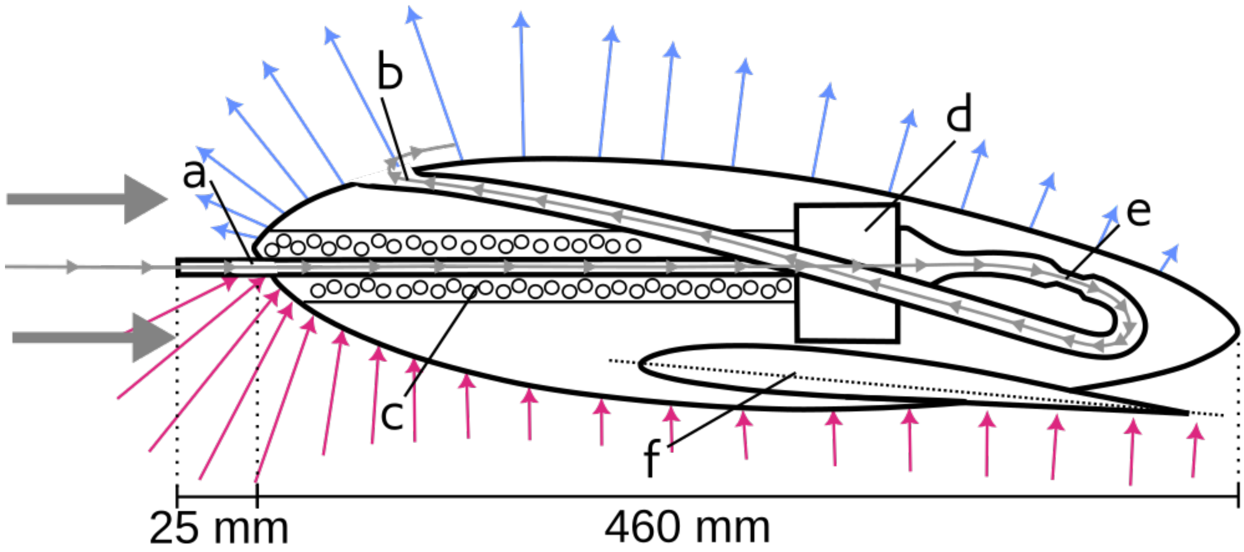

FIG. 2. Cross-section of the OPC-Pod. When exposed to an airflow corresponding to the cruising airspeed of MASC-3 at 18.5 m s^{-1} (gray arrows) and mounted at an angle of attack of 5°, a pressure gradient develops (red arrows: high pressure below the pod, blue arrows: low pressure above the pod). This pressure gradient between the inlet (a) and the exhaust (b) leads to a constant volumetric flow of 9 l min^{-1} (small gray arrows). This aspirates the system, transporting air through the diffusion dryer (c), the OPC N-3 (d), and the mass flow sensor (e). For more details on the passive aspiration system, see Mashni et al. (2023) The entire system is mounted on the wing of MASC-3. In this sketch the wing chord (dashed line) is tilted by 5°, representing the attitude of the pod during flight. (f).

OPC-N3 has a variance coefficient of below 10% when determining particle mean diameter, against a reference instrument (Kaur and Kelly 2023). To reduce the influence of hygroscopic growth, the OPC-Pod is equipped with a custom-made diffusion dryer attached to the inlet of the OPC-N3 (Fig. 2) (Savvakis et al. 2023). This diffusion dryer consists of a perforated inner tube 23 cm long and 6 mm in diameter surrounded by an outer tube with a diameter of 3.5 cm. The drying agent used in the space between the two tubes is silica gel. The inner tube is coated with conductive graphite paint to mitigate the effect of static charge. The inlet is a simple thin-walled inlet with an inner diameter of 6 mm and an outer diameter of 7 mm. The distance from the inlet to the front of the pod is 25 mm (Fig. 2). The OPC-N3 comes with a small fan at the exhaust that provides a total flow rate of 5.5 l min^{-1} and a sample flow rate of 0.28 ml min^{-1}. However, the OPC-N3 is designed to work in ambient conditions. To adapt to the measurement conditions aboard an airborne system, we have modified the OPC-N3 to work with a passive aspiration system in the OPC-Pod, which creates airflow through the pressure differences along the airfoil shape of the OPC-Pod shell. The pod has a symmetrical cross section based on a NACA0024 airfoil (with an increased aft body thickness to accommodate the installed sensors). As with any airfoil, when subjected to airflow, a pressure gradient develops between the area of high dynamic pressure at the front and below the wing and low pressure above the wing (Fig. 2). With the inlet located at the front of the pod and the exhaust at the upper part of the pod, this pressure gradient creates a flow inside the OPC-Pod that increases with the angle of attack. Mashni et al. (2023) provides a detailed description of the passive aspiration system. The inlet, drying channel and OPC are arranged in an iso-axial configuration to minimize particle loss. The autopilot installed in MASC-3 uses a pitot tube to maintain a constant indicated airspeed of 18.5 m s^{-1}. This means that the speed of the MASC-3 relative to the surrounding air is constant, regardless of the wind. Like any fixed-wing aircraft, the wings of the MASC-3 are not completely level during flight, but are constantly at a positive angle to the incoming airflow (the angle of attack). This angle of attack is constant throughout the flight, even when climbing or descending, and generally changes only when the airspeed or mass of the aircraft is changed. For the configuration presented in this manuscript, the angle of attack for the straight flight sections varies between 4.5° and 5.3° (for ascending and descending flight sections), with an average standard deviation σ per section of 0.3°. To ensure that the inlet of the OPC-Pod is iso-axial to the incoming airflow, it is mounted with the components inside the pod tilted at -5° relative to the wing chord of the MASC-3 (Fig. 2). Since the MASC-3 maintains a constant indicated airspeed during flight, the differential pressure along the pod remains constant, resulting in a constant flow inside the pod regardless of any changes in air density. This provides passive aspiration and eliminates the need for a pump or valve. Wind tunnel experiments show that at an airspeed of 18.5 m s^{-1} and an angle of attack of 5°, the resulting volumetric flow measured by a Sensirion SMF3300 flow sensor in the OPC-Pod is 9 l min^{-1}. When operating the OPC-Pod under ambient conditions, for example when comparing the OPC-Pod to a reference instrument on the ground, a pump is attached to the OPC-Pod outlet to create an airflow equivalent to the airflow generated by the passive aspiration system aboard MASC-3.

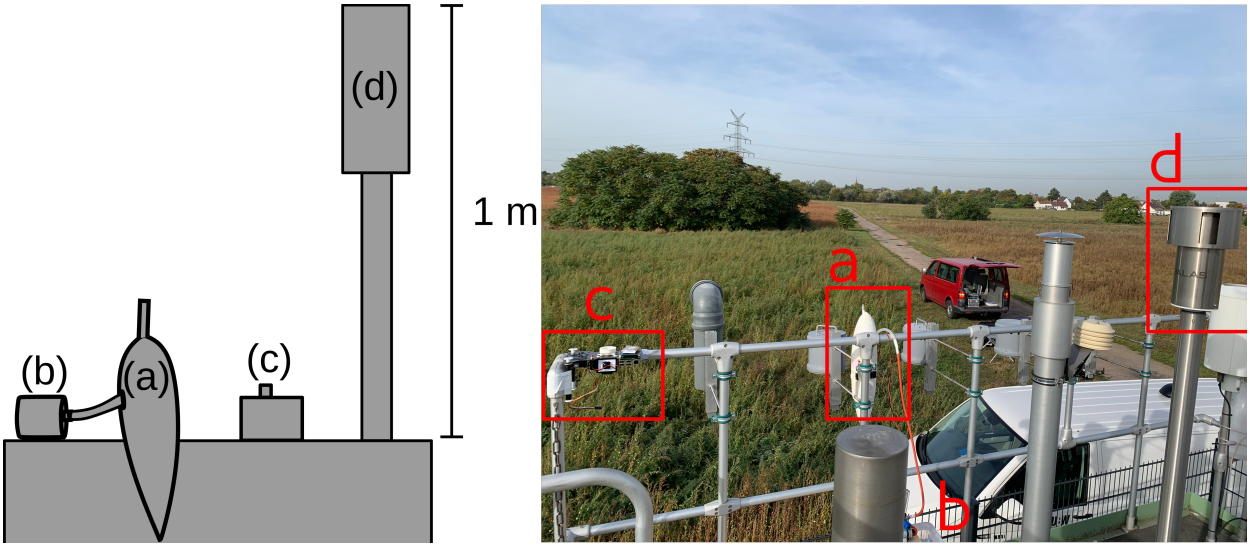

FIG. 3. Diagram and photo of the field validation experiment. The OPC-Pod (a) is aspirated by an electric pump (b) connected to the Pod's exhaust, creating a flow of $9\,\mathrm{l\,min^{-1}}$. The OPC-Pod and an unmodified OPC N-3 (c) are all mounted vertically on top of an air quality measurement station near Mannheim, Germany. The inlet of the station's Palas Fidas 200 aerosol spectrometer is next to the test setup (d).

c. Validation against reference instrument

To validate that the modified OPC-N3 inside the OPC-Pod is still capable of reliably measuring particle concentration and to evaluate the performance of the diffusion dryer, a comparative measurement was performed in the field with the OPC-Pod, a Palas Fidas 200 aerosol spectrometer (Palas GmbH 2023a, EN 15267 certified, equipped with a drying system) and an unmodified OPC-N3 (Fig. 3). The comparison consists of two measurement at an environmental monitoring site of the Baden-Württemberg State Institute for the Environment, Survey, and Nature Conservation near the city of Mannheim (coordinates: 49°32' 38.68" N, 8°27' 55.01" E). The first experiment took place at low air temperatures (0.3-2.8 °C) and above 88% relative humidity (RH), the second measurement at higher temperatures (20 °C) and 60% RH. Mannheim is an industrial region, and fine particle concentration there is generally high. During these tests, the OPC-Pod was operated with a pump (with a flow rate of $9\,\mathrm{l\,min^{-1}}$). The size distributions of PNC are compared to the output of the unmodified OPC-N3 and the reference Palas Fidas 200 of the environmental monitoring site.

d. Wind tunnel validation

In flight, at an airspeed of 18.5 m s^{-1}, the median airspeed at the inlet of the OPC-Pod is 5.6 m s^{-1}, and the maximum Reynolds number at the inlet is 2200. Thus, the OPC-Pod's measurement path is isoaxial, but sub-isokinetic. Since in the experiment in section 2c the OPC-Pod was aspirated using a pump in ambient conditions, an additional validation experiment is performed to estimate particle loss through the system in flight conditions compared to an unmodified, stock OPC-N3. For further reference, a Palas Fidas Frog (Palas GmbH 2023b) aerosol spectrometer is mounted in the wind tunnel, which provides total PNC from 0.45 - 18 μm.

The validation setup consists of the OPC-Pod mounted in a wind tunnel with test dust injected into the wind tunnel inlet. The test dust used is polydisperse dolomite dust with particle sizes ranging from 0 - 20 μm (DMT-Group 2023). Dolomite was chosen as a material similar to soil dust. In addition, dolomite is safer to handle than the commonly used silica dust.

To ensure that the stock OPC-N3 and the Fidas Frog measure the same air mass as the OPC-Pod, but without the high airflow velocity, they are mounted near the inlet of the wind tunnel. The air moving through the wind tunnel recirculates from its exhaust to its inlet, which transports and mixes the injected particles (Fig. 4). The wind tunnel flow is set to the cruising airspeed of MASC-3 so that a volumetric flow of 9 L $\min^{-1}$ is achieved in the OPC-Pod. In addition to evaluating sensor performance, this setup also accounts for the effects of the non-isokinetic inlet and potential aerodynamic effects on the particle measurement, since the wind tunnel can produce an airflow equivalent to the conditions aboard MASC-3 during flight.

Since the relative humidity in the wind tunnel is maintained at about 30%, the influence of hygroscopic growth on the measurements of both systems is minimal and can be ignored.

At the beginning of the test, aerosol particles are injected downstream of the wind tunnel. During the following hour, the particles circulate through the wind tunnel, and the particle concentration decreases due to sedimentation. In order to avoid measuring while the particle concentration is still inhomogeneous, comparisons are made after a period of one time constant (the time required for the dust levels to reduce to e^{-1} of their initial amount, with e being the Eulerian number), which for this experiment is $\approx$ 25 min.

The resulting data from the OPC-Pod is then compared to the result from the stock OPC N-3 in terms of total PNC and count fraction of the respective bin sizes.

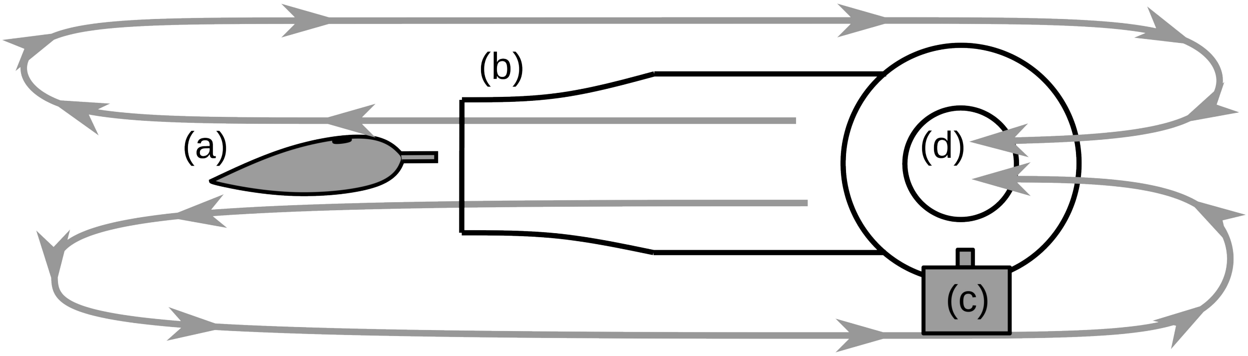

Fig. 4. Diagram of the wind tunnel validation experiment. The OPC-Pod (a) is mounted at the wind tunnel's (b) exhaust, creating an air speed of 18.5 m s^{-1}, resulting in a flow of 9 l min^{-1} inside the OPC-Pod. The stock OPC-N3 (c) is mounted at the inlet of the wind tunnel (d). Dolomite test dust with a particle size between 0-20 μm is injected at the beginning of the experiment and then recirculated through the wind tunnel (gray arrows).

The validation experiment was repeated six times and the resulting count fractions were averaged for each experiment.

e. Flight measurements and comparison with UCASS system

For more conclusive validation, a flight measurement campaign was conducted at the Cyprus Institute's Unmanned Systems Research Laboratory (USRL; Kezoudi et al. 2021b) airfield (coordinates: 35° 5' 41.64" N, 33° 4' 53.76" E, altitude: 327 m ASL, Fig. 5) in Orounda, Nicosia, Cyprus, from 6 April 2022 to 13 April 2022 during a Saharan dust event. The Cyprus Institute provides the necessary infrastructure and legal framework for conducting high-altitude UAS flights (Kezoudi et al. 2021b), which allowed MASC-3 to capture the Saharan air layer during the flight experiments, with flights reaching altitudes up to 6000 m ASL. In parallel to the MASC-3 flights, the Cyprus Institute's fixed-wing electric propulsion Skywalker UAS was flown with the UCASS aerosol particle measurement system (Smith et al. 2019) to provide a comparison for the OPC-Pod measurements. Size bin boundaries for the UCASS are listed in Tab. A2.

The flight pattern of the MASC-3 UAS consisted of vertical profiles (Fig. 6), where the aircraft climbed in sections of 1.5 km length to an altitude of 3000 m - 6000 m ASL. In this paper we present one of these flights from the morning of 6 April 2022 climbing to 3000 m ASL, showing

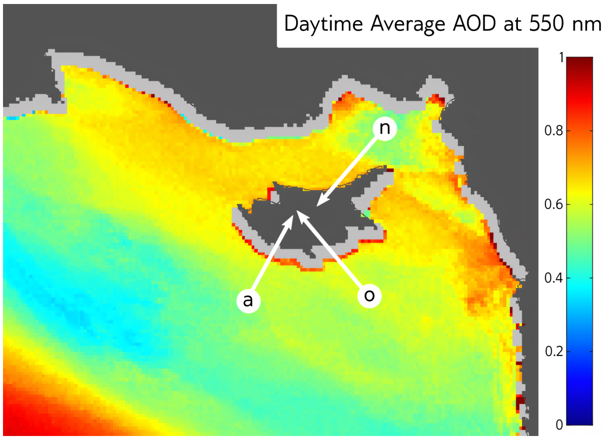

Fig. 5. AOD over ocean at 550 nm over Cyprus on 6 April 2022, 10:00 UTC, derived from the SEVIRI Instrument on the Meteosat Second Generation (MSG) satellite. Marked are the locations of the two AERONET photometers used in Fig. 10, (a) Agia Marina Xiliatou at 521 m ASL, (n) Nicosia, at 181 m ASL, and (o) the Cyprus Institute Orounda airfield at 327 m ASL. AOD Data provided by LSCE/ICARE (AERIS/ICARE Data and Services Center 2024). We thank the AERIS/ICARE Data and Services Center for providing access to the data used in this study.

the size distribution for both the dust layer and the surface layer, as well as vertical profiles from the OPC-Pod of total PNC in the size range 0.66 - 31 μm. For the vertical profile of the UCASS, the closest bin sizes are selected, resulting in a size range of 0.68 - 29.72 μm. The ascent and descent of MASC-3 was performed at a constant vertical velocity of 1.5 $\mathrm{m\ s^{-1}}$ and a constant indicated airspeed of 18.5 $\mathrm{m\ s^{-1}}$. The ascent of MASC-3 began at 11:30 local time (EEST) and reached 3000 m ASL at 12:00 EEST, with the descent ending at 12:30 EEST. The UCASS system was launched at 12:40 EEST and performed a vertical profile to 3500 m ASL shortly after MASC-3 landed.

3. Results and Discussion: Field validation in Mannheim

a. Results

During the first field test comparison at the Mannheim Nord measurement station, conditions were very humid, with relative humidity values ranging from 98% in the morning, to 88% at noon and air temperatures between 0.3 °C in the morning and 2.8 °C at noon, measured at the German

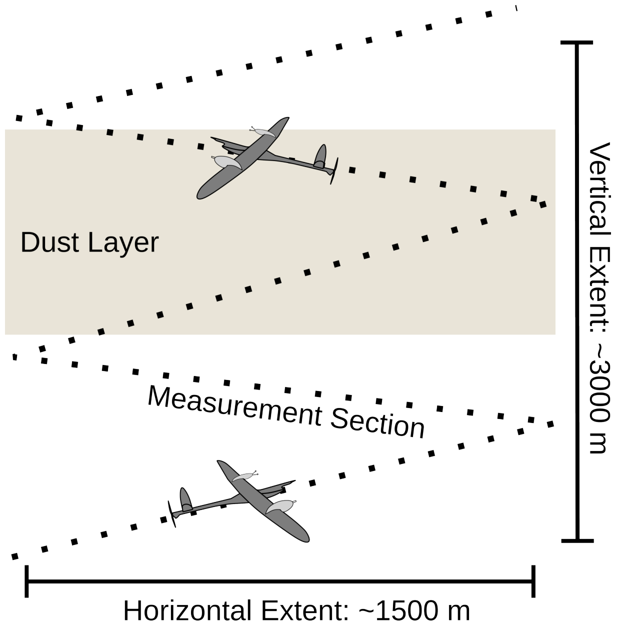

FIG. 6. A diagram of the vertical profile flight pattern of MASC-3. Along sections with a horizontal extent of 1500 m, MASC-3 climbs with a constant vertical velocity of 1.5 m s^{-1} to an altitude above the dust layer. In the case the flight presented here, this altitude was around 3000 m ASL. The descent follows the same pattern as the ascent, with a constant descent rate of 1.5 m s^{-1}.

weather service (DWD) weather station in Mannheim. Fog prevailed during the first half of the day.

The dry size distribution for the first test (Fig. 7 a) from the OPC-Pod and Palas Fidas 200 show good agreement for the smaller particle sizes, but the OPC-Pod underestimates the PNC of coarser particles (3.0 - 10 μm) by up to 80%. The ambient measurement of the OPC-N3, on the other hand, overestimates the PNC of smaller particles (0.46 - 3.0 μm) by up to 1000%. Like the OPC-Pod, the unmodified OPC-N3 underestimates the number concentration above 3.0 μm.

The second field test (Fig. 7 b) was conducted under dry and sunny conditions. The relative humidity values were between 50.0 - 58.6%, and the air temperatures were between 20.4 - 23.3 °C. The size distribution was measured by the same three instruments as before, but this time, both the OPC-Pod and OPC-N3 show similar results (Fig. 7 b). The OPC-Pod and OPC-N3 agree well for most particle sizes, with a maximum deviation of 28% for the size range between 0.66 - 8 μm. However, for the smallest size bin at 0.55 μm, the OPC-Pod shows a higher number concentration

Accepted for publication in *Journal of Atmospheric and Oceanic Technology*. DOI 10.1175/JTECH-D-23-0078.1.

with an increase by 46%. For larger particles above 8 μm, both instruments showed very low number concentrations. Compared to the reference Palas Fidas 200, both instruments generally underestimated the number concentration in the second field test. Similar to the first field test at high humidity, this underestimation is more severe for bin sizes above 3 μm.

b. Discussion

In dry conditions (Fig. 7 b), both the OPC-Pod and the OPC-N3 agree well while they both show a slight underestimation over a range of channels larger than 3.0 μm compared to the Palas Fidas 200, consistent with previous studies showing how the OPC-N3 underestimates PM_{10} while showing good correlation with reference instruments for PM_1 and $PM_{2.5}$ (Molnar et al. 2020). A notable difference between the unmodified OPC-N3 and the OPC-Pod in dry conditions (Fig. 7 b) is the higher bin count of the OPC-Pod in the 0.46-0.66 μm bin. This behavior is further discussed below, since it also appears in the windtunnel experiment (section 4b).

The significant overestimation of PNC by the unmodified OPC-N3 in humid conditions (Fig. 7 a) is expected and confirms the effect of hygroscopic growth on PM measurements, as previous studies have shown a significant overestimation related to high humidity with the OPC-N3 (Savvakis et al. 2023), as well as its predecessor, the OPC-N2 (Crilley et al. 2018).

Considering the low-cost and lightweight nature of the OPC-Pod, the captured size distribution is in good agreement to the reference Palas Fidas 200. The results also show the importance of considering hygroscopic growth in such a system, especially when measuring in humid environments.

4. Results and Discussion: Wind tunnel experiment

a. Results

For the wind tunnel experiment, to show differences in size distribution between the two instruments, the count fraction per size bin is averaged across all six experiments (Fig. 8).

The difference between the OPC-Pod and the unmodified OPC-N3 varies from bin to bin, with the OPC-Pod showing a 30 - 35% overestimation in the coarse mode (particles larger than 4 μm) and about 20% in the very first bin (0.46 - 0.66 μm). For particles between 0.66 - 3 μm, the OPC-Pod underestimates compared to the unmodified OPC-N3. The underestimation of the OPC-Pod

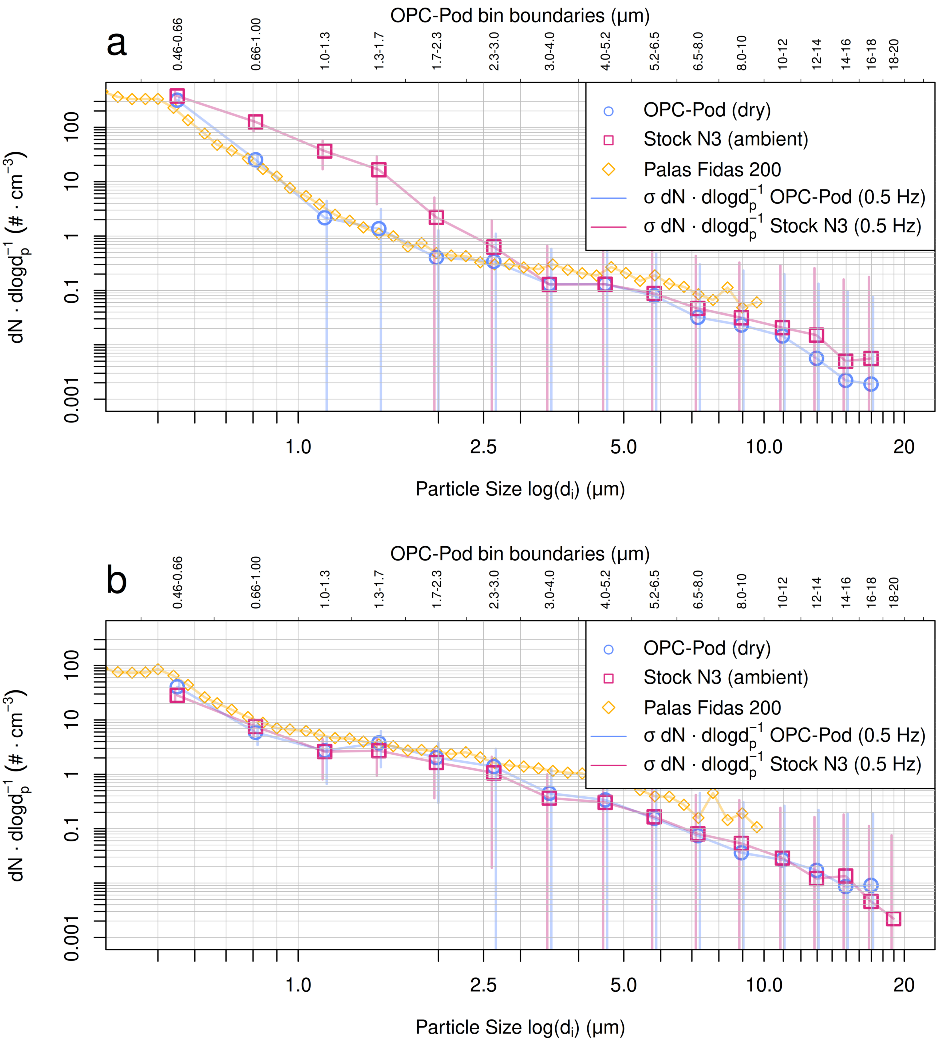

FIG. 7. Aerosol normalized concentration for the OPC-Pod (blue), the unmodified OPC-N3 (red), and the Palas Fidas 200 aerosol spectrometer (orange) for the field tests at the air quality measurement station (Mannheim Nord, 8°27'55.01" N, 49°32'38.68" E). Error bars show the standard deviation of the aerosol normalized concentration σ during the measurement period. Measured on (a) 1200 UTC - 1340 UTC, 14 February 2023 in humid conditions, (b) 0900 UTC - 1000 UTC, 10 October 2023 in dry conditions. The OPC-Pod and the Palas Fidas device had a dryer installed, and the unmodified OPC-N3 measured ambient particle concentration. The top horizontal axis shows the bin boundaries of the OPC-Pod for the depicted mean geometric diameters (see Tab. A1).

reaches about 45% for the bins between 1 and 2.5 μm, but remains at 20% for the remaining size channels. The overestimation compared to the unmodified OPC-N3 in the first bin is similar to the overestimation in this bin during the field tests in Mannheim (Fig. 7 b). Both sensors show a overall similar size distribution, with a local maximum at the 1.3 - 1.7 μm size bin. Both instruments also show an increased variance between multiple experiments towards the larger bin channels.

For the time series of total PNC of the six experiment runs (Fig. 9), we exclude the smallest bin, since the overestimation in this bin is a systematic issue encountered both during the measurements in Mannheim (Fig. 7) and in the windtunnel experiment (Fig. 8). To correspond to the total PNC provided by the Fidas Frog instrument, the total PNC is restricted to 18 μm. Both the OPC-Pod and the unmodified OPC-N3 show lower total PNC compared to the Fidas Frog, and the OPC-Pod shows slightly lower total PNC than the unmodified OPC-N3. The OPC-Pod shows a higher spread for total PNC in all experiments (Fig. 9. While both instruments agree well in the 1-minute maximum PNC values, the OPC-Pod captures lower minimum PNC values, which consequently reduces the 1-minute mean of this sensor.

b. Discussion

The shift in count fraction observed in the size distribution between the OPC-Pod and the unmodified OPC-N3 (Fig. 8) is likely an effect of the sub-isokinetic nature of the sampling method of the OPC-Pod, which results in an underestimation of smaller sized particles and an overestimation of larger sized particles, with up to 43% underestimation for the size bins between 0.66 μm - 2.3 μm, and up to 48% overestimation for the size bins between 2.3 μm - 10 μm. However, the overall shape of the size distribution between the two instruments is similar, with both showing a local maximum at 1.5 μm. This suggests that, when exposed to airflow at the cruise speed of the MASC-3, the OPC-Pod performs similarly to an unmodified OPC-N3 at ambient conditions, except for the described shift in the size distribution due to sub-isokinetic sampling.

The wind tunnel experiments show a consistent trend in total PNC between the OPC-Pod and the unmodified OPC-N3. For the total PNC in the 0.66 - 18 μm range, both instruments agree well. The slightly lower total PNC measured by the OPC-Pod (Fig. 9) is likely a result of the sub-isokinetic sampling described above. However, considering the sub-isokinetic sampling of the OPC-Pod, we would expect an underestimation for all smaller size bins, but for the smallest size

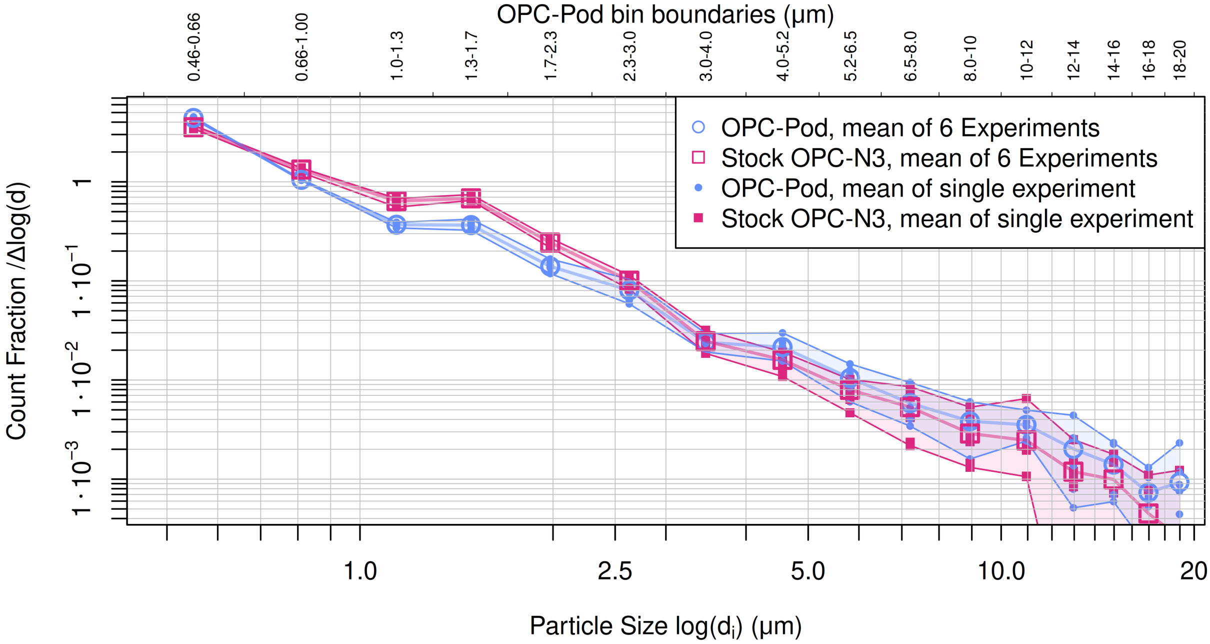

FIG. 8. Count fraction for each size bin from 0.46 - 20 μm of the OPC-Pod (blue circles) and the stock OPC-N3 (red squares). The data are averaged from six wind tunnel experiments. Small icons depict the mean of a single experiment (mean experiment value), a large icon depicts the mean of all six experiments per bin. The colour shaded regions represent the spread between the maximum mean experiment value and the minimum mean experiment value for each instrument. The top horizontal axis shows the bin boundaries of the OPC-Pod for the depicted mean geometric diameters (see Tab. A1).

bin of 0.46 - 0.66 μm, the OPC-Pod actually shows an overestimation compared to the OPC-N3, reflecting the results from the field test in dry conditions in Mannheim (Fig. 7 b). The reason for this overestimation is not clear. In a blank test in filtered air, the OPC-Pod shows zero counts in all bins, so it is unlikely to be due to damaged optics. Since the unmodified OPC-N3 does not show this behavior, it does not seem to be a peculiarity of the Alphasense OPC-N3 in general. To remove the influence of this overestimation from the time series and vertical profiles of total PNC, we show the total PNC starting at 0.66 μm for both the windtunnel experiment and the comparison of the total PNC in the flight experiment. Compared to the total PNC provided by the Fidas Frog, both the OPC-Pod and the unmodified OPC-N3 show lower total PNC, which corresponds to the results from the field test in Mannheim in dry conditions compared to the Palas Fidas 200.

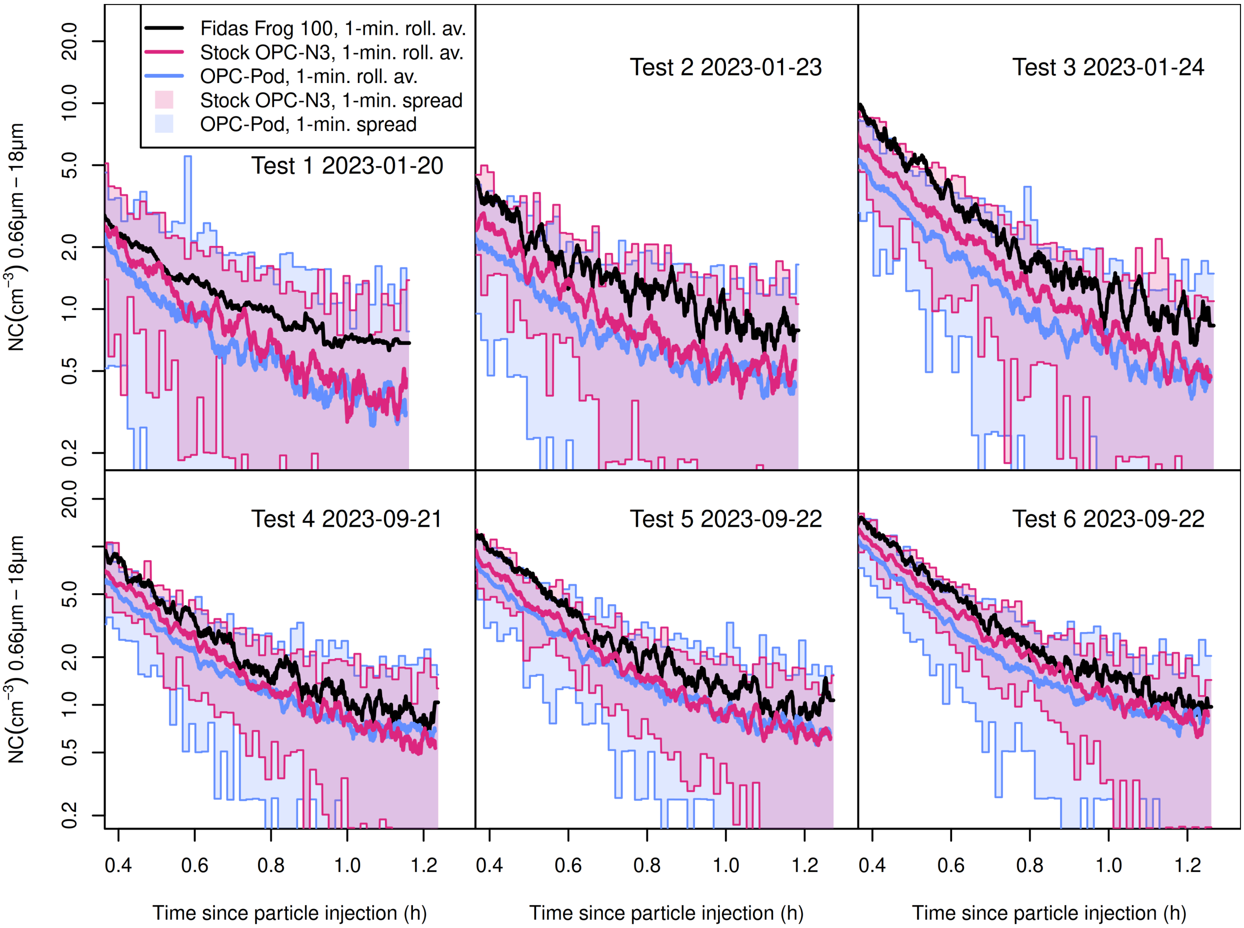

FIG. 9. Wind tunnel time series of PNC 0.46 - 18 μm of the OPC-Pod (blue), an unmodified OPC N-3 (red) and a Fidas Frog (black) during six experiments. The analyzed time window starts when the unmodified OPC N-3 reaches e^{-1} of its maximum particle number concentration and ends 1 hour after this timestamp. Data from each instrument are displayed as a line for the rolling mean of one minute, while the color shaded region represents the spread of the data, ranging from the minimum to the maximum PNC value measured per one minute interval.

5. Results and Discussion: Cyprus flight measurements

a. Results

The measurement flight on 6 April 2022 at Orounda airfield, Cyprus, was conducted during a Saharan dust event.

Fig. 10 shows the daily-averaged columnar Aerosol Optical Depth (AOD) at 550 nm and 675 nm (AERONET version 3 level 2.0 data) as observed by two sunphotometers in Cyprus, one in Nicosia

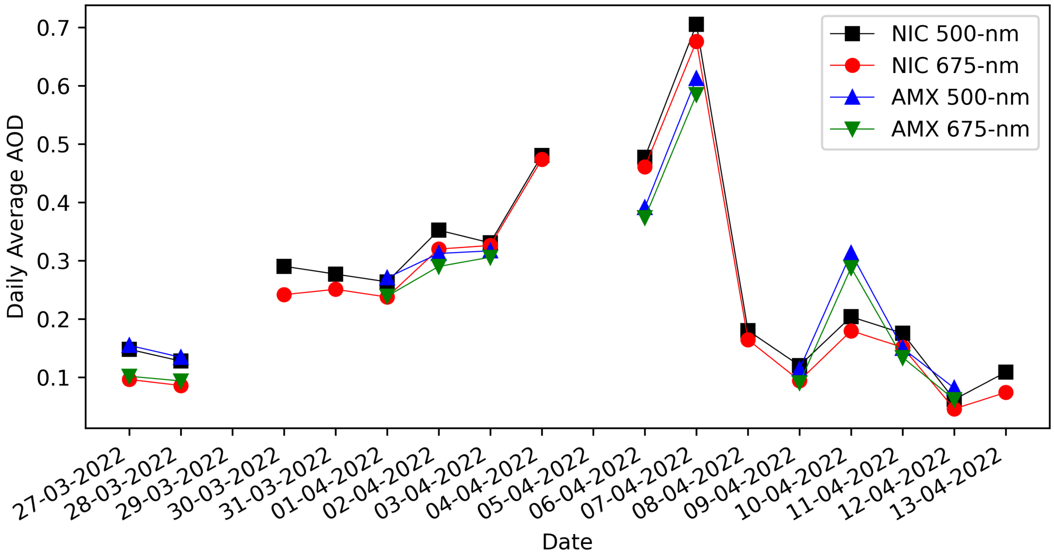

FIG. 10. Daily averaged columnar Aerosol Optical Depth (AOD) as observed by two AERONET sunphotometers: (i) in Nicosia (at the Cyprus Institute) and (ii) at the Agia Marina Xyliatou (AMX) station, located next to Orounda airfield (6 km horizontal distance). The period shown is between 27 March 2022 to 13 April 2022 for the two wavelengths of 550 nm and 675 nm.

(NIC, at the Cyprus Institute site) and one at the Agia Marina Xyliatou (AMX) station which is located adjacent to Orounda airfield (6 km horizontal distance), from 27 March 2022 to 13 April 2022. The location of the stations is also depicted in Fig. 5. High AODs were observed on 6 and 7 April, corresponding to the significant Saharan dust event over the island. This dust event is also visible in the generally elevated AOD over the Mediterranean Sea around Cyprus derived from Meteosat Second Generation (MSG) satellite data (Fig. 5, (Thieuleux et al. 2005)).

On 6 April, ground temperatures were reaching about 25° C, with a relative humidity of about 35%, an atmospheric pressure of 969 hPa, and westerly winds of 2-3 m s^{-1} at the ground and 14 m s^{-1} at 2300 m ASL. Saharan dust in the atmosphere led to low visibility and solar radiation on 6 April.

MASC-3 began its ascent after takeoff from Orounda airfield at 325 m ASL at 11:30 local time (EEST). The ascent ended at 2900 m ASL at 12:00 EEST, which marked the beginning of the descent. After another half hour descent, MASC-3 landed at 12:30 EEST. Following the MASC-3 flight, the UCASS system of the Cyprus Institute was launched at 12:40 EEST and acquired a vertical profile up to 3500 m ASL.

Since a systematic overestimation for the smallest bin size (0.46 - 0.66 μm) of the OPC-Pod was observed during the wind tunnel experiment and the measurement in Mannheim, the profile acquired by the OPC-Pod (Fig. 11 a) shows the vertical distribution of the particle number concentration in a size range between 0.66 - 31 μm (and 0.68 - 29.72 μm for the UCASS). The data shown are averaged over a height range of 20 m. For the size range shown, the ascent profile captured by the OPC-Pod shows an aerosol number concentration of about 15 cm^{-3} from the surface (350 m ASL) to 1280 m ASL. Above 1280 m ASL the number concentration decreases to 9 cm^{-3} at 1500 m ASL. Above this there are two dust concentration maxima visible in the profile, one with 25 cm^{-3} at 2000 m ASL and a vertical extent of about 260 m, and another with a maximum concentration of 29 cm^{-3} at 2300 m ASL and a vertical extent of 570 m. The dust layer caps off at an altitude of 2800 m ASL, with very low aerosol number concentrations of about 2 cm^{-3} above. For the descent of MASC-3, the same patterns are captured again, but the local maxima in the dust layer are shifted downward by about 80 m. In contrast to the ascent, a local maximum in dust concentration is observed near the surface, with up to 21 cm^{-3} between the surface and 540 m ASL.

During its ascent, UCASS captured a similar vertical distribution as MASC-3. It sees a local maximum near the surface at 24 cm^{-3}, up to an altitude of 620 m ASL, which is a higher particle concentration compared to the MASC-3 measurement in this region. The two local maxima in the dust layer above 2500 m ASL are observed as well, but again shifted downward by about 270 m compared to MASC-3's ascent. For the lower local maximum, UCASS recorded a concentration of 22 cm^{-3} at 1740 m ASL, and for the upper maximum it shows a concentration of 35 cm^{-3} at 2400 m ASL. The dust layer is capped slightly lower than in the MASC-3 profile, at 2660 m ASL.

The thermal stratification of the very shallow ABL on 6 April was neutral to convective, with a weak inversion at about 700 m ASL (Fig. 11 b). This inversion developed more during the period between ascent and descent. Comparing the ascent and descent data from MASC-3, the temperature within the ABL dropped about 2 K during the flight. The free atmosphere above was stable, with low humidity throughout the profile at about 30%. In the ABL, relative humidity varied during the 1-hour flight, with 40 - 50 % relative humidity during ascent and 50 - 60 %

relative humidity during descent. A low relative humidity of 12% was measured above the region of increased particle concentration at 2800 m ASL. Mean wind speed increased from 3 m s^{-1} at ground level to 11 m s^{-1} at 950 m ASL, then decreased slightly to 7 m s^{-1} from 950 m ASL to 1220 m ASL, and slowly increased again to a maximum of 14 m s^{-1} at 2300 m ASL at the top of the profile. The wind direction was westerly in the range of 275° to 305° throughout the profile, with a slight dip from 280° to 295° in the vertical profile at 2000 m ASL, coinciding with the lower edge of the high particle number concentration section between 1550 m ASL and 2800 m ASL.

In Fig. 12, we present the number concentration size distribution for two distinct altitude ranges: the lower region extending from the surface to 1200 m ASL, and a section characterized by higher total number concentrations extending from 2200 - 2800 m ASL (or 2200 - 2550 m ASL for the UCASS), referred to as the dust layer in the following description. The OPC-Pod instrument shows notable differences in the size distributions between these altitude sections. In the dust layer, particle concentrations in the size range up to 4 μm are up to 80% higher compared to the lower section. Both height sections show a local maximum in the size distribution for particles falling within the 1.30 - 1.7 μm bin. For particles measuring 4 - 16 μm, the dust layer shows an up to 180% higher concentration compared to the lower section. However, above 16 μm the concentration in the dust layer decreases, while the lower height section registers another local maximum for particles in the 16 μm bin. For particles larger than 16 μm, the OPC-Pod reports up to 200% higher number concentration per bin in the lower altitude section compared to the dust layer above.

Compared to the OPC-Pod, the UCASS size distribution shows several significant differences. Notably, the OPC-Pod shows high concentrations in the 0.46 - 0.66 μm size range, which is consistent with our observations from the validation experiments, where the OPC-Pod tended to overestimate this particular size bin. Another clear difference, for both altitude sections, is the maximum in number concentration for the 2.12 - 2.36 μm bin of the UCASS. Compared to the nearest OPC-Pod bin, UCASS reports a 290% higher number concentration. For coarser particles, when comparing the UCASS measurement in the dust layer to the lower altitude section, the distribution pattern mirrors the trends seen in the OPC-Pod data. Specifically, a higher particle number concentration is seen in the 4 - 16 μm size range in the dust layer. The increase in number concentration for the largest particles in the lower altitude section is also seen in UCASS, but here only the largest size bin shows a higher number concentration in the lower altitude section than in the dust layer.

b. Discussion

The flight measurement on 6 April took place during a Saharan dust event in the eastern Mediterranean, over Orounda, Cyprus, as shown by high AOD values on 6 April in the sunphotometer data (Fig. 10) as well as increased AOD around Cyprus in the MSG/SEVIRI data (Fig. 5).

The vertical profiles of total PNC recorded by UCASS and MASC-3 (Fig. 11 a) are similar in both structure and absolute values. However, the structures in the profile recorded by UCASS appear to be shifted downward compared to MASC-3. This downward shift is already apparent when comparing the MASC-3 ascent and descent profiles, so it is likely that the observed dust layers varied in height during the measurement period. The simultaneous measurement of humidity, temperature (Fig. 11 b), wind speed and wind direction (Fig. 11 c) shows that the section of elevated PNC between about 1500 m ASL up to 2800 m ASL is a distinct layer, separated from below by a temperature inversion and wind shear between 1300 m and 1500 m. The ABL develops a stronger inversion during the MASC-3 flight (visible in the potential temperature profile). In addition, the relative humidity and the PNC in the ABL also increase between the ascent and descent of MASC-3. Following the MASC-3 flight, UCASS measures an even higher PNC in the ABL. This could be due to a general increase in PNC in the ABL, but also to hygroscopic growth as a result of the increased humidity.

The UCASS size distributions follow a similar trend than the OPC-Pod. They show relatively low coarse-mode size fraction in the dust layer, while this size range shows increased PNC closer to the surface, possibly due to local transport processes lifting dust from the surface. However, there are some differences to the OPC-Pods measurement. For the smallest size bin of the UCASS (0.58 - 0.68 μm) the PNC is significantly lower than the PNC of the OPC-Pod in the same size range. This is most likely due to the consistent overestimation of PNC by the OPC-Pod in the smallest size bin described in section 3 and section 4. For particles from 1.52 - 2.82 μm, the UCASS shows a maximum in size distribution that is only reflected by a small bump in the OPC-Pod's size distribution at 1.3 - 1.7 μm. This, compared with the UCASS' decreased PNC for particles

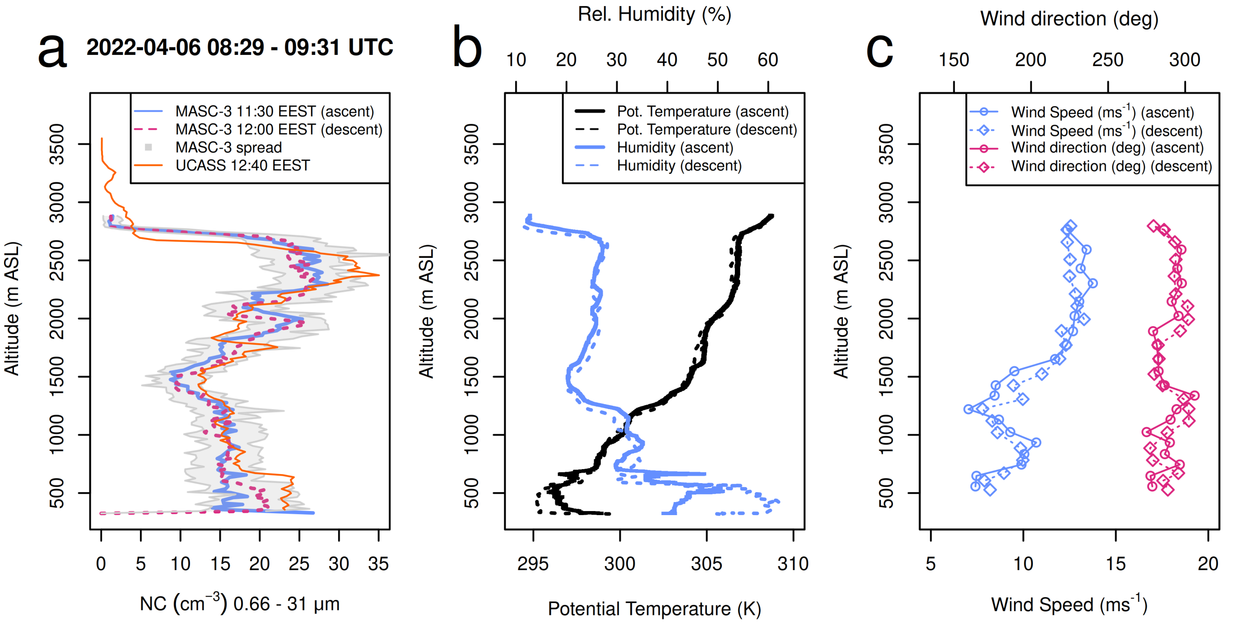

FIG. 11. Vertical profiles of (a) PNC for the size range 0.66 - 31 μm for MASC-3, 0.68 - 29.72 μm for UCASS. PNC is averaged per 20 m of altitude (solid blue and red dashed lines). Additionaly, the OPC-Pod raw PNC data are shown as grey shaded area. Data from the UCASS system (Smith et al. 2019) are shown for comparison. (b) potential temperature and relative humidity measured by the digital humidity and temperature sensor in the nose of the aicraft and (c) horizontal wind and wind direction, averaged per 1.5 km horizontal measurement section. Captured by MASC-3 over Orounda, Cyprus, on 6 April 2022 during a Saharan dust event. For each parameter, data from MASC-3 ascent and descent are plotted separately.

above 10 μm is potentially an effect of the OPC-Pod's sub-isokinetic sampling, underestimating fine particles and overestimating coarse particles.

6. Conclusions

This study presents a new aerosol particle measurement system based on a commercially available low-cost OPC (Alphasense OPC-N3) modified by adding a passive aspiration system using the flow around an aerodynamically shaped pod. A mass flow sensor and a custom-built diffusion dryer and a logging system were added. This sensor package can operate as an add-on payload on the wing of a small fixed-wing UAS of the type MASC-3, alongside the aircraft's standard meteorological sensor payload, capable of measuring high-frequency 3D wind vector, temperature, humidity, and

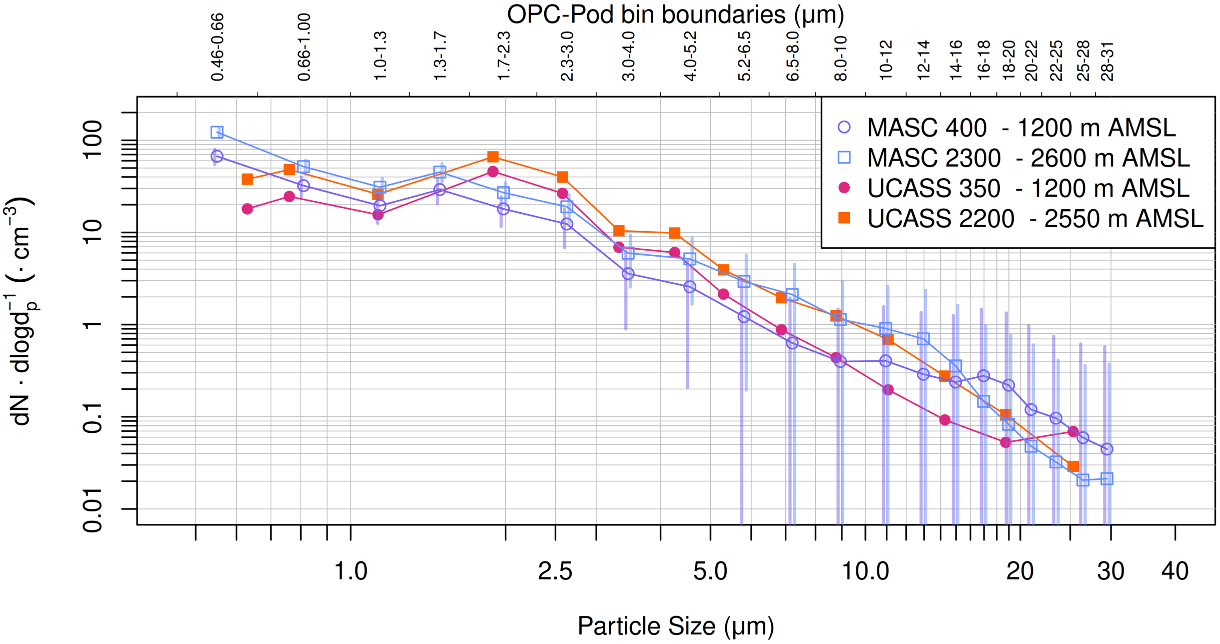

Fig. 12. Aerosol particle normalized concentration captured by MASC-3 and UCASS over Orounda, Cyprus, on 6 April 2022, during a Saharan dust event. Size distributions for each instrument are split into two altitude sections: A lower section, close to the ground up to 1200 m ASL (purple for MASC-3, red for UCASS) and a section for the dust layer (blue for MASC-3, orange for UCASS). The error bars depict the standard deviation σ per altitude section and size bin for MASC-3. The top horizontal axis shows the bin boundaries of the OPC-Pod for the depicted mean geometric diameters (see Tab. A1).

space charge. It was tested against a reference instrument in ambient and high humidity urban conditions, followed by a wind tunnel test simulating flight conditions at 18.5 m s^{-1} using suspended dolomite dust as a surrogate for dust in the atmosphere, and finally in flight during a Saharan dust event over Cyprus. The field test in humid conditions shows that the significant overestimation of PNC by an unmodified OPC-N3 is not present when measuring with the OPC-Pod, due to the installed diffusion dryer. The wind tunnel experiment shows that the passive aspiration system based on pressure differences along the OPC-Pod shell provides sufficient airflow for the sensor inside. The measurement show minor shifts in size distribution compared to an unmodified OPC-N3, overestimating coarse-mode particles and underestimating fine particles, which could be due to potentially sub-isokinetic sampling conditions.

During a flight test in Cyprus, MASC-3 climbed to 3000 m ASL to adequately capture a Saharan dust event. Aerosol particle data from our OPC-Pod and data from the meteorological sensor payload provide a comprehensive picture of the atmospheric column. The data covers a dust layer between 1500 - 2800 m ASL. The total number concentration in the size range 0.66 - 37 μm measured by the OPC-Pod is in good agreement with the UCASS system operated by the Cyprus Institute. While the size distributions of the OPC-Pod and the UCASS system generally agree well, UCASS records higher PNC in the range 1.52 - 2.36 μm, and generally lower PNC for sizes above 10 μm. In conclusion, the OPC-Pod is a capable system comparing well to reference instruments, when limitations due to its low-cost and lightweight nature and the sub-isokinetic sampling are considered.

7. Outlook

Improvements to the OPC-Pod will require addressing sub-isokinetic sampling, either through the development of an isokinetic inlet or a correction function derived from refined calibration experiments. A more detailed investigation of the particular Saharan dust event presented here will be performed in a future publication and will include additional results from MASC-3 flights, multi-rotor UAS vertical profiles, the Cyprus Institute's UCASS system, space charge and turbulence measurements. Future measurement campaigns could take place together with other airborne in-situ measurement platforms to perform simultaneous measurements, for example with UCASS (Smith et al. 2019), LOAC (Renard et al. 2018) or ALADINA (Altstädter et al. 2015). Another possible improvement to the measurement system presented here is to equip the MASC-3 with two OPC-Pods, one diffusion dried as presented here and an identical pod without a dryer, so that information on hygroscopic growth can be obtained by comparing dry and ambient PNC.

Acknowledgments. We thank the following people for their support for the work: colleagues in the Environmental Physics Workgroup of the University of Tübingen, Hasan Mashni, Matteo Bramati, Ines Weber, and Kjell zum Berge, who helped develop the OPC-Pod, maintained MASC-3, provided the logistics, and supported the measurement flights.; the pilot of MASC-3, Henrik Rieth; Kenny Haaker, whose Master Thesis laid the groundwork for the validation of the OPC-Pod.; Martin Schempp, for providing and servicing the airframe of MASC-3; Philippe Goloub and Franco Marenco for their effort in establishing and maintaining the AERONET site Agia Marina Xyliatou; Francois Dulac and an anonymous reviewer for the extensive feedback on this manuscript; Jean Sciare, Christos Keleshis and the whole Unmanned Systems Research Laboratory (USRL) team of the Cyprus Institute, for providing infrastructure, the invaluable support during our experiments, and especially the support during our stay at the beginning of the 2020 COVID pandemic;

The work presented here is part of the Trans-national access (TNA) project IMSAP that is supported by the European Comission under the Horizon 2020 – Research and Innovation Framework Programme, H2020-INFRADEV-2019-2, Grant Agreement number: 871115.

Data availability statement. The data that support the findings of this study are available from the corresponding author, Martin Schön, upon reasonable request.

APPENDIX

Size bins and geometric diameter of OPC-N3 and UCASS

TABLE A1. Alphasense OPC-N3 size bin boundaries and geometric midpoint diameters used in this work (Alphasense 2019)

Lower size boundary (μm)	Upper size boundary (μm)	Geometric midpoint diameter (μm)
0.46	0.66	0.55
0.66	1.00	0.81
1.00	1.30	1.14
1.30	1.70	1.49
1.70	2.30	1.98
2.30	3.00	2.63
3.00	4.00	3.46
4.00	5.20	4.56
5.20	6.50	5.81
6.50	8.00	7.21
8.00	10.00	8.94
10.00	12.00	10.95
12.00	14.00	12.96
14.00	16.00	14.97
16.00	18.00	16.97
18.00	20.00	18.97
20.00	22.00	20.98
22.00	25.00	23.45
25.00	28.00	26.46
28.00	31.00	29.46

Accepted for publication in *Journal of Atmospheric and Oceanic Technology.* DOI 10.1175/JTECH-D-23-0078.1.

TABLE A2. UCASS size bin boundaries and geometric midpoint diameters used in this work

Lower size boundary (μm)	Upper size boundary (μm)	Geometric midpoint diameter (μm)
0.58	0.68	0.63
0.68	0.84	0.76
0.84	1.52	1.13
1.52	2.36	1.89
2.36	2.82	2.58
2.82	3.90	3.32
3.90	4.66	4.26
4.66	6.02	5.30
6.02	7.58	6.87
7.58	9.80	8.77
9.80	12.5	11.07
12.5	16.28	14.27
16.28	21.58	18.74
21.58	29.72	25.33

References

AERIS/ICARE Data and Services Center, 2024: Multi-sensor browse interface. Accessed 13 February 2024, https://www.icare.univ-lille.fr/asd-content/browse/geoview.

Alphasense, 2019: User Manual: OPC-N3 Optical Particle Counter. Accessed 19 May 2022, https://www.alphasense.com/wp-content/uploads/2019/03/OPC-N3.pdf.

Altstädter, B., and Coauthors, 2015: ALADINA–an unmanned research aircraft for observing vertical and horizontal distributions of ultrafine particles within the atmospheric boundary layer. *Atmos. Meas. Tech.*, **8 (4)**, 1627–1639, https://doi.org/10.5194/amt-8-1627-2015.

Ansmann, A., and Coauthors, 2003: Long–range transport of Saharan dust to northern Europe: The 11–16 October 2001 outbreak observed with EARLINET. *J. Geophys. Res.: Atmos.*, **108 (D24)**, https://doi.org/10.1029/2003JD003757.

Athanasopoulou, E., A. Protonotariou, G. Papangelis, M. Tombrou, N. Mihalopoulos, and E. Gerasopoulos, 2016: Long-range transport of Saharan dust and chemical transformations over the Eastern Mediterranean. *Atmos. Environ.*, **140**, 592–604, https://doi.org/10.1016/j.atmosenv.2016.06.041.

Bangert, M., and Coauthors, 2012: Saharan dust event impacts on cloud formation and radiation over Western Europe. *Atmos. Chem. Phys.*, **12 (9)**, 4045–4063, https://doi.org/10.5194/acp-12-4045-2012.

Barkan, J., and P. Alpert, 2010: Synoptic analysis of a rare event of Saharan dust reaching the Arctic region. *Weather*, **65 (8)**, 208–211, https://doi.org/10.1002/wea.503.

Bates, T., P. Quinn, J. Johnson, A. C. F.J., B. S.E., Stalin, C. Meinig, and J. F. Burkhart, 2013: Measurements of atmospheric aerosol vertical distributions above Svalbard, Norway, using unmanned aerial systems (UAS). *Atmos. Meas. Tech.*, **6 (8)**, 2115–2120, https://doi.org/10.5194/amt-6-2115-2013.

Benedetti, A., and Coauthors, 2009: Aerosol analysis and forecast in the European centre for medium-range weather forecasts integrated forecast system: 2. Data assimilation. *J. Geophys. Res.: Atmos.*, **114 (D13)**, https://doi.org/10.1029/2008JD011115.

Bezantakos, S., F. Schmidt-Ott, and G. Biskos, 2018: Performance evaluation of the cost-effective and lightweight Alphasense optical particle counter for use onboard unmanned aerial vehicles. *Aerosol Sci. Technol.*, **52 (4)**, 385–392, https://doi.org/10.1080/02786826.2017.1412394.

Brady, J. M., M. D. Stokes, J. Bonnardel, and T. H. Bertram, 2016: Characterization of a quadrotor unmanned aircraft system for aerosol-particle-concentration measurements. *Environ. Sci. Technol.*, **50 (3)**, 1376–1383, https://doi.org/10.1021/acs.est.5b05320.

Chouza, F., O. Reitebuch, A. Benedetti, and B. Weinzierl, 2016: Saharan dust long-range transport across the Atlantic studied by an airborne Doppler wind lidar and the MACC model. *Atmos. Chem. Phys.*, **16 (18)**, 11 581–11 600, https://doi.org/10.5194/acp-16-11581-2016.

Chung, C. E., 2012: Aerosol direct radiative forcing: a review. *Atmospheric Aerosols: Regional Characteristics - Chemistry and Physics*, H. Abdul-Razzak, Ed., IntechOpen, 379–394, https://doi.org/10.5772/2695.

Crilley, L. R., M. Shaw, R. Pound, L. J. Kramer, R. Price, S. Young, A. C. Lewis, and F. D. Pope, 2018: Evaluation of a low-cost optical particle counter (Alphasense OPC-N2) for ambient air monitoring. *Atmos. Meas. Tech.*, **11 (2)**, 709–720, https://doi.org/10.5194/amt-11-709-2018.

de Boer, G., and Coauthors, 2016: The Pilatus unmanned aircraft system for lower atmospheric research. *Atmos. Meas. Tech.*, **9 (4)**, 1845–1857, https://doi.org/10.5194/amt-9-1845-2016.

Denjean, C., and Coauthors, 2016: Size distribution and optical properties of mineral dust aerosols transported in the western Mediterranean. *Atmos. Chem. Phys.*, **16 (2)**, 1081–1104, https://doi.org/10.5194/acp-16-1081-2016.

DMT-Group, 2023: Datasheet: DMT Dolomite Test Dust up to 20 my. Accessed 29 September 2023, https://testdust.dmt-group.com/en/test-dust/46/dmt-dolomite-test-dust-up-to-20-my.

Dunion, J. P., and C. S. Velden, 2004: The impact of the saharan air layer on atlantic tropical cyclone activity. *Bull. Amer. Meteor. Soc.*, **85 (3)**, 353–366, https://doi.org/10.1175/BAMS-85-3-353.

Gasteiger, J., S. Groß, D. Sauer, M. Haarig, A. Ansmann, and B. Weinzierl, 2017: Particle settling and vertical mixing in the Saharan Air Layer as seen from an integrated model, lidar, and in situ perspective. *Atmos. Chem. Phys.*, **17 (1)**, 297–311, https://doi.org/10.5194/acp-17-297-2017.

Gkikas, A., E. Houssos, N. Hatzianastassiou, C. Papadimas, and A. Bartzokas, 2012: Synoptic conditions favouring the occurrence of aerosol episodes over the broader Mediterranean basin. *Quart. J. Roy. Meteor. Soc.*, **138 (665)**, 932–949, https://doi.org/10.1002/qj.978.

Gobbi, G. P., F. Barnaba, R. Giorgi, and A. Santacasa, 2000: Altitude-resolved properties of a saharan dust event over the mediterranean. *Atmos. Environment*, **34 (29)**, 5119–5127, https://doi.org/10.1016/S1352-2310(00)00194-1.

Harrison, R. G., 2000: Cloud formation and the possible significance of charge for atmospheric condensation and ice nuclei. *Space Sci. Rev.*, **94 (1)**, 381–396, https://doi.org/10.1023/A:1026708415235.

Harrison, R. G., K. A. Nicoll, G. J. Marlton, C. L. Ryder, and A. J. Bennett, 2018: Saharan dust plume charging observed over the UK. *Environ. Res. Lett.*, **13 (5)**, 054 018, https://doi.org/10.1088/1748-9326/aabcd9.

Heintzenberg, J., 2012: The aerosol-cloud-climate conundrum. *Int. J. Glob. Warm.*, **4 (3-4)**, 219–241, https://doi.org/10.1504/IJGW.2012.049438.

Helmert, J., B. Heinold, I. Tegen, O. Hellmuth, and M. Wendisch, 2007: On the direct and semidirect effects of Saharan dust over Europe: A modeling study. *J. Geophys. Res.: Atmos.*, **112 (D13)**, https://doi.org/10.1029/2006JD007444.

Inness, A., and Coauthors, 2013: The MACC reanalysis: an 8 yr data set of atmospheric composition. *Atmos. Chem. Phys.*, **13 (8)**, 4073–4109, https://doi.org/10.5194/acp-13-4073-2013.

Israelevich, P., E. Ganor, P. Alpert, P. Kishcha, and A. Stupp, 2012: Predominant transport paths of Saharan dust over the Mediterranean Sea to Europe. *J. Geophys. Res.: Atmos.*, **117 (D2)**, https://doi.org/10.1029/2011JD016482.

Jickells, T. D., and Coauthors, 2005: Global Iron Connections Between Desert Dust, Ocean Biogeochemistry, and Climate. *Science*, **308 (5718)**, 67–71, https://doi.org/10.1126/science.1105959.

Johnson, B. T., and S. R. Osborne, 2011: Physical and optical properties of mineral dust aerosol measured by aircraft during the GERBILS campaign. *Quart. J. Roy. Meteor. Soc.*, **137 (658)**, 1117–1130, https://doi.org/10.1002/qj.777.

Karanasiou, A., N. Moreno, T. Moreno, M. Viana, F. de Leeuw, and X. Querol, 2012: Health effects from Sahara dust episodes in Europe: literature review and research gaps. *Environ. Int.*, **47**, 107–114, https://doi.org/10.1016/j.envint.2012.06.012.

Kaur, K., and K. E. Kelly, 2023: Laboratory evaluation of the Alphasense OPC-N3, and the Plantower PMS5003 and PMS6003 sensors. *Journal of Aerosol Science*, **171**, 106 181, https://doi.org/10.1016/j.jaerosci.2023.106181.

Kezoudi, M., and Coauthors, 2021a: Measurement report: Balloon-borne in situ profiling of Saharan dust over Cyprus with the UCASS optical particle counter. *Atmos. Chem. Phys.*, **21 (9)**, 6781–6797, https://doi.org/10.5194/acp-21-6781-2021.

Kezoudi, M., and Coauthors, 2021b: The Unmanned Systems Research Laboratory (USRL): A New Facility for UAV-Based Atmospheric Observations. *Atmosphere*, **12 (8)**, https://doi.org/10.3390/atmos12081042.

Koehler, K. A., S. M. Kreidenweis, P. J. DeMott, M. D. Petters, A. J. Prenni, and C. M. Carrico, 2009: Hygroscopicity and cloud droplet activation of mineral dust aerosol. *Geophys. Res. Lett.*, **36 (8)**, https://doi.org/10.1029/2009GL037348.

Kok, J. F., and Coauthors, 2021: Contribution of the world's main dust source regions to the global cycle of desert dust. *Atmos. Chem. Phys.*, **21 (10)**, 8169–8193, https://doi.org/10.5194/acp-21-8169-2021.

Lohmann, U., and J. Feichter, 2005: Global indirect aerosol effects: a review. *Atmos. Chem. Phys.*, **5 (3)**, 715–737, https://doi.org/10.5194/acp-5-715-2005.

Mamali, D., and Coauthors, 2018: Vertical profiles of aerosol mass concentration derived by unmanned airborne in situ and remote sensing instruments during dust events. *Atmos. Meas. Tech.*, **11 (5)**, 2897–2910, https://doi.org/10.5194/amt-11-2897-2018.

Mashni, H., H. Knaus, A. Platis, and J. Bange, 2023: Development of an Airfoil-Based Passive Volumetric Air Sampling and Flow Control System for Fixed-Wing UAS. *Bull. Atmos. Sci. Technol.*, accepted for publication.

Mauro, B. D., and Coauthors, 2019: Saharan dust events in the European Alps: role in snowmelt and geochemical characterization. *The Cryosphere*, **13 (4)**, 1147–1165, https://doi.org/10.5194/tc-13-1147-2019.

McConnell, C. L., P. Formenti, E. J. Highwood, and M. A. J. Harrison, 2010: Using aircraft measurements to determine the refractive index of Saharan dust during the DODO Experiments. *Atmos. Chem. Phys.*, **10 (6)**, 3081–3098, https://doi.org/10.5194/acp-10-3081-2010.

Molnar, A., K. Imre, Z. Ferenczi, G. Kiss, and A. Gelencser, 2020: Aerosol hygroscopicity: Hygroscopic growth proxy based on visibility for low-cost PM monitoring. *Atmos. Res.*, **236**, 104 815, https://doi.org/10.1016/j.atmosres.2019.104815.

Moulin, C., and Coauthors, 1998: Satellite climatology of African dust transport in the Mediterranean atmosphere. *J. Geophys. Res.: Atmos.*, **103 (D11)**, 13 137–13 144, https://doi.org/10.1029/98JD00171.

Niu, T., S. Gong, G. Zhu, H. Liu, X. Hu, C. Zhou, and Y. Wang, 2008: Data assimilation of dust aerosol observations for the CUACE/dust forecasting system. *Atmos. Chem. Phys.*, **8 (13)**, 3473–3482, https://doi.org/10.5194/acp-8-3473-2008.

O'Sullivan, D., and Coauthors, 2020: Models transport Saharan dust too low in the atmosphere: a comparison of the MetUM and CAMS forecasts with observations. *Atmos. Chem. Phys.*, **20 (21)**, 12 955–12 982, https://doi.org/10.5194/acp-20-12955-2020.

Palas GmbH, 2023a: Palas Fidas 200 Technical Features. Accessed 30 October 2023, https://www.palas.de/en/product/fidas200.

Palas GmbH, 2023b: Palas Fidas Frog Technical Features. Accessed 15 November 2023, https://www.palas.de/product/fidasfrog.

Papadimas, C. D., N. Hatzianastassiou, C. Matsoukas, M. Kanakidou, N. Mihalopoulos, and I. Vardavas, 2012: The direct effect of aerosols on solar radiation over the broader Mediterranean basin. *Atmos. Chem. Phys.*, **12 (15)**, 7165–7185, https://doi.org/10.5194/acp-12-7165-2012.

Papayannis, A., and Coauthors, 2008: Systematic lidar observations of Saharan dust over Europe in the frame of EARLINET (2000–2002). *J. Geophys. Res.: Atmos.*, **113 (D10)**, https://doi.org/10.1029/2007JD009028.

Pikridas, M., and Coauthors, 2019: On-flight intercomparison of three miniature aerosol absorption sensors using unmanned aerial systems (UASs). *Atmos. Meas. Tech.*, **12 (12)**, 6425–6447, https://doi.org/10.5194/amt-12-6425-2019.

Pilon, R., and Coauthors, 2022: Saharan dust vertical distribution is controlled by convection and scavenging. why do models miss this? *EGU General Assembly 2022*, Vienna, Austria, https://doi.org/10.5194/egusphere-egu22-2754.

Platis, A., B. Altstädter, B. Wehner, N. Wildmann, A. Lampert, M. Hermann, W. Birmili, and J. Bange, 2016: An Observational Case Study on the Influence of Atmospheric Boundary-Layer Dynamics on New Particle Formation. *Boundary-Layer Meteorology*, **158 (1)**, 67–92, https://doi.org/https://doi.org/10.1007/s10546-015-0084-y10.1007/s10546-015-0084-y.

Pöschl, U., and Coauthors, 2010: Rainforest Aerosols as Biogenic Nuclei of Clouds and Precipitation in the Amazon. *Science*, **329 (5998)**, 1513–1516, https://doi.org/10.1126/science.1191056.

Rautenberg, A., and Coauthors, 2019: The Multi-Purpose Airborne Sensor Carrier MASC-3 for Wind and Turbulence Measurements in the Atmospheric Boundary Layer. *Sensors*, **19 (10)**, 2292, https://doi.org/10.3390/s19102292.

Renard, J.-B., and Coauthors, 2016a: LOAC: a small aerosol optical counter/sizer for ground-based and balloon measurements of the size distribution and nature of atmospheric particles – Part 1: Principle of measurements and instrument evaluation. *Atmos. Meas. Tech.*, **9 (4)**, 1721–1742, https://doi.org/10.5194/amt-9-1721-2016.

Renard, J.-B., and Coauthors, 2016b: LOAC: a small aerosol optical counter/sizer for ground-based and balloon measurements of the size distribution and nature of atmospheric particles – Part 2: First results from balloon and unmanned aerial vehicle flights. *Atmos. Meas. Tech.*, **9 (8)**, 3673–3686, https://doi.org/10.5194/amt-9-3673-2016.

Renard, J. B., and Coauthors, 2018: In situ measurements of desert dust particles above the western Mediterranean Sea with the balloon-borne Light Optical Aerosol Counter/sizer (LOAC) during the ChArMEx campaign of summer 2013. *Atmos. Chem. and Physics*, **18 (5)**, 3677–3699, https://doi.org/10.5194/acp-18-3677-2018.

Savvakis, V., M. Schön, M. Bramati, A. Platis, and J. Bange, 2023: Small-scale diffusion dryer on an optical particle counter for high humidity aerosol measurements with an uncrewed aircraft system. *J. Atmos. Oceanic Technol.*, (under revision).

Schön, M., K. A. Nicoll, Y. G. Büchau, S. Chindea, A. Platis, and J. Bange, 2022: Fair Weather Atmospheric Charge Measurements with a Small UAS. *J. Atmos. Oceanic Technol.*, **39 (11)**, 1799–1813, https://doi.org/10.1175/JTECH-D-22-0025.1.

Schrod, J., and Coauthors, 2017: Ice nucleating particles over the Eastern Mediterranean measured by unmanned aircraft systems. *Atmos. Chem. Phys.*, **17 (7)**, 4817–4835, https://doi.org/10.5194/acp-17-4817-2017.

Smith, H. R., and Coauthors, 2019: The Universal Cloud and Aerosol Sounding System (UCASS): a low-cost miniature optical particle counter for use in dropsonde or balloon-borne sounding systems. *Atmos. Meas. Tech.*, **12 (12)**, 6579–6599, https://doi.org/10.5194/amt-12-6579-2019.

Sousan, S., S. Regmi, and Y. M. Park, 2021: Laboratory evaluation of low-cost optical particle counters for environmental and occupational exposures. *Sensors*, **21 (12)**, 4146, https://doi.org/10.3390/s21124146.

Stuut, J.-B., I. Smalley, and K. O'Hara-Dhand, 2009: Aeolian dust in Europe: African sources and European deposits. *Quat. Int.*, **198 (1-2)**, 234–245, https://doi.org/10.1016/j.quaint.2008.10.007.

Swap, R., M. Garstang, S. Greco, R. Talbot, and P. Kållberg, 1992: Saharan dust in the amazon basin. *Tellus B*, **44 (2)**, 133–149, https://doi.org/10.3402/tellusb.v44i2.15434.

Swietlicki, E., and Coauthors, 2008: Hygroscopic properties of submicrometer atmospheric aerosol particles measured with H-TDMA instruments in various environments–a review. *Tellus B: Chemical and Physical Meteorology*, **60 (3)**, 432–469, https://doi.org/10.1111/j.1600-0889.2008.00350.x.

Thieuleux, F., C. Moulin, F. M. Bréon, F. Maignan, J. Poitou, and D. Tanré, 2005: Remote sensing of aerosols over the oceans using msg/seviri imagery. *Ann. Geophys.*, **23 (12)**, 3561–3568, https://doi.org/10.5194/angeo-23-3561-2005.

Tomaso, E. D., N. A. J. Schutgens, O. Jorba, and C. P. Garc'ıa-Pando, 2017: Assimilation of MODIS Dark Target and Deep Blue observations in the dust aerosol component of

NMMB-MONARCH version 1.0. *Geosci. Model Dev.*, **10 (3)**, 1107–1129, https://doi.org/10.5194/gmd-10-1107-2017.

Varga, G., 2020: Changing nature of Saharan dust deposition in the Carpathian Basin (Central Europe): 40 YEARs of identified North African dust events (1979–2018). *Environ. Int.*, **139**, 105 712, https://doi.org/10.1016/j.envint.2020.105712.

Wildmann, N., M. Mauz, and J. Bange, 2013: Two fast temperature sensors for probing of the Atmospheric Boundary Layer using small Remotely Piloted Aircraft (RPA). *Atmos. Meas. Tech.*, **6 (2)**, https://doi.org/10.5194/amt-6-2101-2013.

Wildmann, N., S. Ravi, and J. Bange, 2014: Towards higher accuracy and better frequency response with standard multi-hole probes in turbulence measurement with remotely piloted aircraft (RPA). *Atmos. Meas. Tech.*, **7 (4)**, 1027–1041, https://doi.org/10.5194/amt-7-1027-2014.

Yu, H., and Coauthors, 2015: The fertilizing role of African dust in the Amazon rainforest: A first multiYEAR assessment based on data from Cloud-Aerosol Lidar and Infrared Pathfinder Satellite Observations. *Geophys. Res. Lett.*, **42 (6)**, 1984–1991, https://doi.org/10.1002/2015GL063040.